Dust grain evolution and interaction in gas-plasma mixtures

Submitted in fulfilment of the requirements

for the Degree of Doctor of Philosophy

Mariam Break Alharbi, M. Sci.

School of Physics and Astronomy

College of Science and Engineering

University of Glasgow

Submitted Aug 2014

Contents

List of Figures

Abstract

The main aim of this thesis is to understand and investigate some essential physical processes leading to dust grain growth and their interactions in plasmas. This is achieved by applying both analytic and numerical models. Three main situations are explored: dust grains growth in presence of electrostatic and electromagnetic fields, dust grains interaction in submicron scales, and collective effects of dust grains above thundercloud.

The evolution and character of plasma dust has wide-ranging implications for astrophysics and laboratory plasmas, including plasma processes and fusion devices. The local electromagnetic fields can influence the conditions for dust growth, leading in some cases to naturally occurring prolate-spheroidal dust shapes. However, presence of magnetic fields can have significant effects on dust growth. Results for dust growth by ion accretion under the combined influence of an applied magnetic field and the evolving electrostatic field arising from the charged grain in 1D and 3D have been presented. The calculations show that most ions starting near the grain surface ultimately collide with it, while those starting further away execute orbital motion around the magnetic field lines and drift toward the grain. Moreover, the energy spectrum for impacting ions shows discrete structure in presence of a parallel oriented magnetic field. Finally, we note that the magnetic field influences the spatial deposition pattern of ions, leading to increasing ions fluxes at the grain ends.

Microdischarge plasmas is an electrical discharges which occurs in geometries in range of sub-millimetre length scales. However, a much extreme situation than microdischarge plasma where small size charged dust grains can cause breakdown for the neutral gas when dust inter space reach to sub-micro scales. The interactions of charged dust grains in plasma where molecules of Oxygen gas are present and the effect on the discharge of the ambient gas is investigated in presence of magnetic field. The particle in cell model was used to simulate electrons motion in addition to using

Monte Carlo method to simulate the electrons collisions with neutrals. The importance of the magnetic field was explored by varying the parameter (p) which gives the relative size of the electric field to the magnetic field. The distribution of electrons kinetic energies was investigated in two cases when ($p = 10^3$) and ($p = 10^2$). At the first case the gained energy increased dramatically, however, the gained energy did not exceed further than the metastables threshold as a result of consuming electrons energy in metastable collisions. When magnetic field is increased ($p = 10^2$), gained energy is fluctuated as a results of contribution in gyromotion orbits and electrons only involved in metastable collisions. However, a number of metastable in this case is lower than ($p = 10^3$) case.

The electron beam can occur just after sprites. The presence of charged dust above thundercloud are thought to have a basic role in the electron beam formation in which the electrons avalanche in sprite event leaving an environment of negative charged dust and positive ions. This environment was simulated in a model like hollow cathode with a column of positive ions inside. The particle in cell method was used to simulate particles motion. Results for electrons evolution in such this environment with and without presence of positive ions were presented. Electrons in environment without positive ions evolve upwards gaining lower final energy. For the case when positive column is presented, electrons evolve upwards in a long path and do not biased to sidewalls. The trajectory of the electron shows an oscillator motion. The period of such motion depends on the electron's original position. Electrons gain higher energy in a shorter time comparing to the case when the ions column is not simulated.

Acknowledgements

Sincere thanks go to my supervisor, Dr. Declan Diver, for his guidance, discussions and advice on my work throughout my PhD. I would also like to thank him for his patience and knowledge whilst allowing me the room to work in my own way.

Special thanks to people in plasma physics group for sharing their knowledge and for useful discussions. Thanks to Craig Stark to the useful discussion.

I would like to thank my parents who have had the best and most positive influence on my life. They were always supporting me and encouraging me with their best wishes. Many thanks to my sisters and brothers for their support and encourage.

I am grateful for the support from my husband, Khalid, who was always the perfect partner over the period of my PhD and through my life. I can not forget to thank my little daughters, Jumanah and Danah, for happiness they add to my life.

I wish to thank Natasha Jeffrey, my office mate, who was always happy to share her extensive knowledge. She always dose not hesitate to give hand when she can.

Finally, I would like to thank all those who supported me in any aspect during the period of the project.

Declaration

I declare that this thesis is my own composition except where indicated in the text and that no portion of the work referred to in the thesis has been submitted in support of an application for another degree or qualification from this or any other institution.

Copyright Statement

1

Introduction

1.1 Plasmas

The term ‘plasma’ is used to describe the matter state in an electrical discharge which contains nearly equal numbers of charged particles (electrons and ions) moving in random directions. This term plasma was first introduced in 1928 by Langmuir [Tonks and Langmuir (1929)] who had observed uncommon electron oscillations while conducting his experiments in ionised gas. These unusual oscillations were oscillations at the plasma frequency. plasma must be larger in extent than its debye length (the characteristic shielding distance in a plasma), and the total number of particles in a debye sphere (ie. the sphere of radius the debye length) should be large (also called the plasma parameter), in order that the electrostatic fluctuations arise mostly from small perturbations of the positions of many particles [**?**]. The presence of charged particles in plasma is responsible for the good conductivity of the plasma as well as for the presence of different wave and instability phenomena.

In an ionised gas (dissociated by an electrical discharge or by thermal means), a mixture of free electrons and ions has been formed, leading to a new medium of charged particles and neutral gas species: a plasma. Plasmas are ubiquitous in universe, either found naturally in the Earth’s atmosphere or within and outwith the solar

system or can be made in devices such as, light tubes, television screens, plasma etching systems for semiconductors, and Tokamaks.

1.2 Dusty plasma

Dusty plasma is a normal electron-ion plasma with solid dust particles with a few nanometer to centimeter sizes [Shukla and Mamun (2010)]. This new system is encountered in many environments such as astrophysics [Goertz (1989); Szopa et al. (2006)] and laboratory plasma including plasma processes [Mikikian et al. (2010)] and fusion devices [Winter (2004)]. These dust particles acquire an electric charge as a result of the absorption of electrons and ions. Because of the small mass of the electrons, their mobility is greater than ions, consequently, grains become negatively charged. Ions are accelerated toward the negatively charged grains in a region called the sheath next to the grain [Shukla and Mamun (2010)].

Dust grain can be injected into a plasma or formed directly in the plasma depending on the environment [Shukla and Mamun (2010)]. For example, in space it can be formed as a result of asteroid collision, while in a Tokamak it may be formed by material ablation during contacting the hot plasma with the fusion vessel structure. Dust is also composed of a range of elements depending on the environment. While it is mainly water ice in Saturns rings, it may be carbon and tungsten components in Tokamaks.

One should distinguish between two terms: dust in a plasma and a dusty plasma depending on the plasma characteristic lengths. The when the dust grain radius (r_d) is much smaller than the plasma Debye radius (λ_D) $r_d \ll \lambda_D < a$, where a is the average distance , corresponds to dust in a plasma, while the case when $r_d \ll a < \lambda_D$ corresponds to a dusty plasma. For the first situation, dust are considered as a collection of isolated screened grains. In the other case, dust grains contribute in the collective behaviour.

The presence of these dust particles add some complexity to the plasma system. It

can affect the interaction between particles and external applied electric and magnetic fields. Furthermore, dust in plasma can produce new kinds of waves, for example, dust acoustic waves (DAW). The interaction between charged grains themselves adds an extra load of complexity, which can be a reason to call this three component dust-ion-electron plasma 'complex plasma'. The dust acoustic wave (DAW) is an essential normal mode of a dusty plasma. In this kind of waves, the restoring force comes from the pressures of the hot electrons and ions, while the dust mass provides the inertia. The frequency of the DAW is smaller than the dust plasma frequency (the electron and ion thermal speeds)[Ghosh et al. (2004)].

1.3 Plasma breakdown

The transformation process of a neutral gas into a conducting self-sustaining discharge is known as plasma breakdown or ignition. Gas discharges range from the very large scale such as lightning and high altitude sprites [van der Velde et al. (2010)] to the very small scale micro-discharges such as plasma display panels [Chen et al. (2006)]. It is important to study discharge processes for fundamental understanding, as well as for its applications [Radmilovi-Radjenovi and Radjenovi (2008)].

1.3.1 Townsend theory

In 1889, Paschen introduced his law for the minimum breakdown voltage after carrying out experiments to study the minimum potential difference that can spark gas between two electrodes in a glass tube [Raizer Yu (1991)]. In his law, the minimum voltage to create breakdown depends on the kind of gas, the distance between the electrodes, d , and the pressure in the tube, p. Furthermore, this minimum voltage is a function of the product between the pressure and the gap distance, pd. It was possible at that time to measure the breakdown voltage experimentally; however, the processes leading to breakdown, were not clearly understood.

Later at the beginning of the twentieth century, Townsend introduced a theory that expressed the breakdown process for gas discharge between parallel plate electrodes, separated by a gap distance d at a pressure p [Meek (1940)]. His theory describes the breakdown processes accurately at a set of conditions where the product pd is at a range of about $0.1 - 100$ Pa.m ($0.075 - 75$ Torr.cm) and the electrode has simple geometries. Townsend's theory provides a description of microscopic processes causing gas breakdown such as the ionization of atoms by electron impact, secondary electron emission at the cathode by ion impact, and charge multiplication in electron avalanches. Townsend's theory is usually used in low-pressure discharge. The following discussion of Townsend theory supposes a uniform electric field $E = \frac{V}{d}$ between parallel metal electrodes, where V is the voltage and d is the distance between electrodes . If a single electron starts at the cathode and forms an electron avalanche towards the anode, then the number of electrons , N_e, as a function of distance x between electrodes is:

$$N_e = e^{\alpha x} \tag{1.1}$$

where α is the ionization coefficient and can be given by the formula:

$$\frac{\alpha}{p} = A \exp\left(\frac{-Bp}{E}\right) \tag{1.2}$$

where constants A and B are gas-specific and are given from experiments, and E is the electric field strength. While the number of ions, N_i, produced by electron impact collision is:

$$N_i = (e^{\alpha d} - 1) \tag{1.3}$$

The electrons during avalanche leave the resulting ions behind in the discharge gap, as a result of the increase in the drift velocity of the electrons being greater than that of the ions. When the electrons reach the anode, the ions have hardly started their drift motion towards the cathode. When ions reach the cathode surface there is a probability, γ, that a secondary electron is emitted from the cathode surface, the number of emitting

secondary electrons for a discharge gap d, is:

$$N_{e,sec} = \gamma(e^{\alpha d} - 1) \tag{1.4}$$

The new secondary electrons will be involved in a new electron avalanche process. If other processes of production and losing charged particles, such as photoionization, field emission and electron attachment are ignored, a criterion for self-sustainment of the electron avalanches can be supposed. The electron avalanche is considered as self-sustaining when the ions coming from a single electron avalanche create a single electron by secondary emission at the cathode surface. This situation can be expressed by:

$$\gamma(e^{\alpha d} - 1) = 1 \tag{1.5}$$

This expression is known as the breakdown criterion and can be rewritten as:

$$e^{\alpha d} = \frac{1}{\gamma} + 1 \tag{1.6}$$

Combining equations 1.2, and 1.6 gives Paschen's Law expression which describes the voltage V_b needed to breakdown a gas and it is a function of pressure and electrode separation distance:

$$V_b = \frac{Bpd}{\ln(Apd)/ln(ln\,(1 + \gamma^{-1}))} \tag{1.7}$$

At high pressure and a large gap distance, discharge evaluates much faster than what can be predicted by Townsend's theory. A new breakdown theory, known as streamer breakdown was introduced . Streamer breakdown theory takes into account space charge effects through electron avalanches, leading to thin, weakly-ionized channels, called streamers.

1.3.2 Streamer breakdown

While the Townsend theory fails to explain the observed, high-speed breakdown features, Loeb [Loeb (1951)], Meek and Raether [Petcharaks (1999)] developed the basis

of a new breakdown theory known as streamer breakdown theory. This new theory considers the space charge effects of a single electron avalanche which were neglected in the Townsend theory. The breakdown process in the streamer theory still results in the developing electrons in the avalanche. However, during avalanche the charge multiplication is very large in which the charges in the avalanche head change the applied electric field. The number Q of space charges contribute to the electric field E_s can be given by:

$$E_s = \frac{Qe}{4\pi\epsilon_0 r^2} \tag{1.8}$$

where e is the elementary charge, ϵ_0 the vacuum permittivity, and r is the radial distance from the centre of the charge region and it can be given by:

$$r = \sqrt{4Dt} \tag{1.9}$$

where D is the diffusion coefficient and t is the time from the avalanche taking place. Reather stated that the anode directed streamer would develop when the carrier number in the avalanche head reached a value of about 10^8. His statement leads to an empirical condition for streamer formation. The streamer formation starts if:

$$e^{\alpha d} = \psi d \tag{1.10}$$

with d being the distance that an electron avalanche travelled, α is the effective ionization coefficient , and $\psi = 1.5 \times 10^4$, where ψ had been calculated based on Friedrich's experiment of synthetic air for α/p calculation.[Petcharaks (1999)]. Equation 1.10 indicates that the applied electric field and the gap distance have to be large enough.

The streamer is described as a thin weakly-ionized channel that develops between the electrodes. The space charge in the streamer head modifies the electric field distribution leading to a high charge multiplication. This helps to develop the streamer very fast. While electron speed is characterized by the electron drift velocity, the produced ions drift very slowly towards the cathode and cause secondary electron emission. Streamer developing velocities are in the order of $10^6 m/s$, and this makes it much faster than in the Townsend breakdown ($10^3 m/s$) [Aleksandrov and Bazelyan (2001)].

1.4 Plasma parameters

1.4.1 The Debye Sphere

The Debye length is an important characteristic length scale in plasma in which at length scales shorter than the Debye length, the quasi-neutrality condition is not valid. For length scales larger than the Debye length, collective processes are dominant. To clarify the Debye length concept, consider a uniform plasma in a thermal equilibrium with temperature T. Since electrons are far more mobile than ions, they therefore respond to the thermal fluctuations much faster than ions. For a 1-D treatment, an electron depletion layer of length L will be created. The electric potential of this layer can be found by solving the Gausss equation:

$$\phi(x) = \frac{n_i q(d^2 - x^2)}{2\epsilon_0} \tag{1.11}$$

where n_i is the ion density, q is the electron charge, d is the maximum width of the no-electron layer, x is the co-ordinate distance, and ϵ_0 is the permittivity of free space.

To find the Debye length which is equivalent to the maximum size d of the layer, equating the maximum potential energy with the thermal energy $1/2k_BT$ to give:

$$\frac{1}{2}k_BT = \frac{ne^2d^2}{2\epsilon_0} \tag{1.12}$$

From equation 1.52 the Debye length is:

$$\lambda_D = d = \left(\frac{\epsilon_0 k_B T}{n_i e^2}\right)^{1/2} \tag{1.13}$$

That means any fluctuations in charge in the plasma will be shielded by a length greater than λ_D, leaving a quasi-neutral plasma on scales $> \lambda_D$. Fig. 1.1 represents the concept of the Debye length.

1.4.2 Plasma Frequency

Consider a plasma averaged over length scales larger than the Debye length which shields the electric field, then a force can be initiated to prevent charge separation.

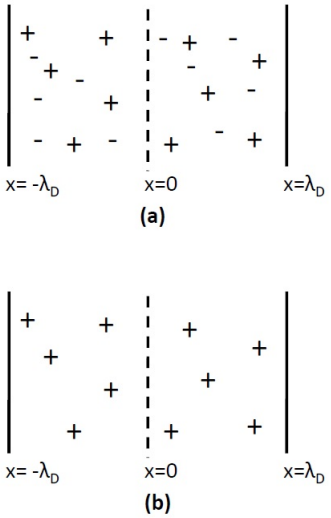

Figure 1.1: Suppose a small region of plasma of length $2\lambda_D$, where λ_D is the Debye length. The figure shows: (a) A 1-D slice of a quasi-neutral plasma. The − represents the electrons, and + represents the protons. The plasma here is locally quasi-neutral. (b)The random thermal fluctuation affect electrons more than the protons, leading to creation of a zone of electron depletion. The characteristic length of the depletion zone is λ_D, the Debye length. Over length scales greater than the Debye length, the plasma is quasi-neutral [Bennet (2012)].

From the continuity equation:

$$\frac{\partial n}{\partial t} + \nabla.(n\boldsymbol{v}) = 0 \tag{1.14}$$

where n is the number density and v is the fluid velocity. Any perturbation occurring leads to charge separation because electrons have a larger mobility than ions. This separation causes an electric field leading to particle acceleration and can be given by:

$$\boldsymbol{E} = -\frac{m_e}{e}\frac{d\boldsymbol{v}}{dt} \tag{1.15}$$

For a perturbation n_1 to a number density n_0 is small, then the equation representing this system can be given by:

$$\frac{\partial^2 n_1}{\partial t^2} + \frac{n_0 e^2}{\epsilon_0 m_e} n_1 = 0 \tag{1.16}$$

This equation represents a simple harmonic motion with a frequency called ‘plasma

frequency':

$$\omega_p = \left(\frac{n_0 e^2}{\epsilon_0 m_e}\right)^{1/2} \tag{1.17}$$

The electric field fluctuations in plasma with a frequency equal to or less than the plasma frequency will be absorbed by the electron motion. For fluctuations with frequency greater than the plasma frequency the electron motion cannot be quick enough to cancel these perturbations.

1.4.3 Electron and Ion Cyclotron Frequency

When a charged particle moves in a plasma only in the presence of a uniform constant magnetic field, its motion is described by the Lorentz equation:

$$m\frac{d\boldsymbol{v}}{dt} = q\boldsymbol{v} \times \boldsymbol{B} \tag{1.18}$$

Consider the magnetic field has a component in z direction only, then equation 1.18 components are:

$$\begin{aligned} \frac{dv_x}{dt} &= \frac{q}{m}Bv_y \\ \frac{dv_y}{dt} &= -\frac{q}{m}Bv_x \\ \frac{dv_z}{dt} &= 0 \end{aligned} \tag{1.19}$$

where v_x, v_y, v_z are the components of the velocity vector. The time derivatives of equations 1.19 are:

$$\begin{aligned} \frac{d^2v_x}{dt^2} &= \left(\frac{qB}{m}\right)^2 v_x \\ \frac{d^2v_y}{dt^2} &= \left(\frac{qB}{m}\right)^2 v_y \end{aligned} \tag{1.20}$$

Equations 1.20 represent a simple harmonic motion at a frequency known as the cyclotron frequency:

$$\omega_c = \frac{\mid q \mid B}{m} \tag{1.21}$$

1.4.4 The Mean-Free Path

Consider a moving electron in a cube with dimensions xyz of atoms which can be seen as a sphere from the moving electron. The number of atoms included in that cube is $nxyz$ where n is the atom density. The cross section of each atom can be represented as $\sigma = \pi r^2$ where r is the radius of the atom. The average distance that can be travelled by the moving electron between collisions is called the mean-free path λ and can be given by:

$$\lambda = \frac{1}{n\sigma} \tag{1.22}$$

1.5 Plasma Sheath

Plasma usually is treated in three different scales with suitable matching parameters at the boundaries, these are: quasi-neutral bulk plasma, a quasi-neutral collisional presheath and a non-neutral sheath. The width of sheath L_s is normally much smaller than the plasma dimensions. To clarify the concept of sheaths, consider a plasma contained in a vacuum chamber of a finite size, since electrons are far more mobile than ions, they reach the wall first resulting in a negatively potential wall. Ions will be attracted by the negative potential at the wall causing the Debye length to confine the potential gradient to a layer, called a sheath, of thicknesses equal to several Debye lengths next to the wall. Sheaths depending on the plasma and wall conditions can be treated as collisionless or collisional. Plasma boundary interactions are significant in many plasma applications, such as semiconductor manufacturing [Tchertchian et al. (2011)], and fusion [Meshkani et al. (2014)]. The concept of presheath arose to match plasma potential at the plasma-sheath boundary . Presheath is a transition area where ions must have a velocity, known as ‘Bohm velocity’, when directed to the sheath.

1.5.1 Collisionless sheath

Consider a collisionless sheath in a plasma with Maxwellian electrons at temperature T_e cold ions ($T_i = 0$), and equal electron and ion densities at the plasma-sheath transition interface. If ions with velocity u_s at a position where $\phi = 0$ at the plasma-sheath interface, where ϕ is the potential, then ions energy is conserved if no collisions are assumed [Lieberman and Lichtenberg (2005)]:

$$\frac{1}{2}Mu^2(x) = \frac{1}{2}Mu_s^2 - e\phi(x) \tag{1.23}$$

Also for the ion flux:

$$n_i(x)u(x) = n_{is}u_s \tag{1.24}$$

with n_{is} being the ion density at sheath edge. From equations 1.23, and 1.24, the ion density is given by:

$$n_i = n_{is}\left(1 - \frac{2e\phi}{Mu_s^2}\right)^{-1/2} \tag{1.25}$$

and from the Boltzmann relation, the electron density is:

$$n_e(x) = n_{es}e^{\phi(x)/T_e} \tag{1.26}$$

Substituting equations 1.25, 1.26 into Poisson's equation;

$$\frac{d^2\phi}{dx^2} = \frac{e}{\epsilon_0}(n_e - n_i) \tag{1.27}$$

At sheath edge $n_{es} = n_{is} = n_s$, equation 1.27 gives:

$$\frac{d^2\phi}{dx^2} = \frac{en_0}{\epsilon_0}\left[\exp\frac{\phi}{T_e} - (1 - \frac{\phi}{\xi_s})^{-1/2}\right] \tag{1.28}$$

where $e\xi_s = \frac{1}{2}Mu_s^2$ is the initial ion's energy. Equation 1.28 gives the potential and electron and ion density at the collisionless sheath. Ions, as mentioned previously, must enter the sheath with Bohm velocity from the presheath layer, then accelerate across the sheath leading to ion density decreasing. If the initial ion energy is low in

comparison to the potential , then the ion energy and the flux conservation (equations 1.23, and 1.24) become:

$$\frac{1}{2}Mu^2(x) = -e\phi(x) \tag{1.29}$$

Also for the ion flux:

$$en_i(x)u(x) = J_0 \tag{1.30}$$

where J_0 is the constant ion current. Solving this for $n(x)$, and using it in Poisson's equation, gives:

$$\frac{d^2\phi}{dx^2} = -\frac{J_0}{\epsilon_0}\left(-\frac{2e\phi}{M}\right)^{-1/2} \tag{1.31}$$

Multiplying by $d\phi/dx$, integrating from 0 to x , taking the negative square root, and integrating again leads to:

$$-\phi^{3/4} = \frac{3}{2}\left(\frac{J_0}{\epsilon_0}\right)^{1/2}\left(-\frac{2e\phi}{M}\right)^{-1/4} x \tag{1.32}$$

Setting $\phi = -V_0$ at $x = s$ gives:

$$J_0 = \frac{4}{9}\epsilon_0\left(\frac{2e}{M}\right)^{1/2}\frac{V_0^{3/2}}{s^2} \tag{1.33}$$

Equation 1.33 is known as: Child−Langmuir's law. It gives the space charge current between two electrodes and depends on the potential difference between them. Using the following relation of current J_0 in Child−Langmuir's law:

$$J_0 = en_s u_B \tag{1.34}$$

gives:

$$L_s = \frac{\sqrt{2}}{3}\lambda_{De}\left(\frac{2V_0}{T_e}\right)^{3/4} \tag{1.35}$$

where λ_{De} is the electron Debye length. This relation gives the sheath thicknesses as a function of sheath potential and plasma parameters. Neglecting the electron number density gives rise to the Child law sheath width to be in the order of $100\lambda_{De}$. However, Child−Langmuir's law can not be used for high pressure discharge and when the sheath potential is not too large compared to electron temperature.

1.5.2 Collisional sheath

If the sheath width is smaller than the mean free path of the ion momentum transfer ($L_s < \lambda_i$), then the Child's law discussed in the previous section is not valid. Therefore, another treatment should be done to deal with the high voltage sheath region and the ion velocity at the sheath edge [Lieberman and Lichtenberg (2005)]. For the sheath region, equation 1.24 , if ionization collisions are not considered, is still valid:

$$n_i u_i = n_s u_s \tag{1.36}$$

where n_s and u_s are the values at the sheath edge. Also, ion velocity when collisions are not neglected is:

$$u_i = \mu_i E \approx \frac{2e\lambda_i}{\pi M \mid u_i \mid} E \tag{1.37}$$

where μ_i is the mobility, and E is the electric field. Solving 1.37 for $u_i > 0$ then substituting in 1.37 gives:

$$n_i = \frac{n_s u_s}{(2e\lambda_i E/\pi M)^{1/2}} \tag{1.38}$$

Substituting this equation in Gauss' law, solving for E, and setting $E(0) \approx 0, \phi(0) = 0$ at the sheath edge, gives the constant currentJ_0:

$$J_0 = \left(\frac{2}{3}\right)\left(\frac{5}{3}\right)^{3/2} \epsilon_0 \left(\frac{2e\lambda_i}{\pi M}\right)^{1/2} \frac{V_0^{3/2}}{L_s^{5/2}} \tag{1.39}$$

This equation is the collisional form of the Child's law. It can be noticed that in this case the current is proportional to the voltage as in the collisionless case but inversely with the sheath width to a different power of the collisionless Child sheath.

1.6 Single particle dynamics

Studying and understanding single particle dynamics are important to get knowledge of plasma processes. In this section an overview of charged particle dynamics in plasma

in presence of an electric field only, magnetic field only, and electric and magnetic fields backgrounds are discussed, in addition to some aspects of magnetized plasma.

1.6.1 Charged particle motion in a uniform electric field

The equation of motion for a particle with mass m, charge q, and velocity $\boldsymbol{V}$ in electric field $\boldsymbol{E}$ and magnetic field $\boldsymbol{B}$ is shown by the Lorentz force $\boldsymbol{F}$ and is given as:

$$\boldsymbol{F} = m\frac{d\boldsymbol{v}}{dt} = q(\boldsymbol{E} + \boldsymbol{v} \times \boldsymbol{B}) \tag{1.40}$$

$$\boldsymbol{v} = \frac{d\boldsymbol{r}}{dt} \tag{1.41}$$

where r is the particle trajectory. In the presence of a constant electric field only, the equation of motion will reduce to:

$$\frac{d\boldsymbol{v}}{dt} = q\boldsymbol{E} \tag{1.42}$$

In this situation the particle moves with a constant acceleration in the direction of the electric field in the case of positive charged particles, and in the opposite direction in the case of negative particles. In a direction perpendicular to the electric field the particle is not accelerated and its motion remains unchanged [Bellan (2006)].

1.6.2 Charged particle motion in a uniform magnetic field

The equation of motion for a particle moving only in a static constant magnetic field is given by:

$$m\frac{d\boldsymbol{v}}{dt} = q(\boldsymbol{v} \times \boldsymbol{B}) \tag{1.43}$$

By taking the scalar product with the velocity vector equation 1.43 becomes:

$$m\boldsymbol{v}.\frac{d\boldsymbol{v}}{dt} = \frac{d}{dt}(\frac{1}{2}mv^2) = q\boldsymbol{v}.(\boldsymbol{v} \times \boldsymbol{B}) = 0 \tag{1.44}$$

From this equation it is clear that the kinetic energy ($w = \frac{1}{2}mv^2$) is a constant. It is convenient to separate the velocity to components parallel $v_{\parallel}$ and perpendicular $v_{\perp}$ to the magnetic field. Because the $\boldsymbol{v} \times \boldsymbol{B}$ force has no component parallel to the magnetic field, therefore the particle moves at a constant velocity along the magnetic field. Since the kinetic energy is constant, v is also constant for the motion, which means that the motion in the plane perpendicular to the magnetic field is a circle and the frequency of this circular motion is known as the cyclotron frequency and it is given by:

$$w_c = \frac{|q|B}{m} \tag{1.45}$$

The centre of the rotational motion is called the guiding centre and the radius of the circle is called the Larmor radius and is given by:

$$r_c = \frac{v_{\perp}}{w_c} \tag{1.46}$$

The Larmor radius is a characteristic minimum scale length for different plasma processes. For a magnetic field pointing towards the observer, positive charged particles rotate in a clockwise direction and in the opposite direction for negatively charged particles[Goldston and Rutherford (1995)].

1.6.3 Motion in uniform electric and magnetic fields

If a particle moves in uniform electric and magnetic fields, the resulting motion consists of a uniform circular motion around the magnetic field plus a uniform translational motion in the $\boldsymbol{E} \times \boldsymbol{B}$ direction with velocity $\boldsymbol{V}_E$ which is called the $\boldsymbol{E} \times \boldsymbol{B}$ drift velocity and is given by:

$$\boldsymbol{V}_E = \frac{\boldsymbol{E} \times \boldsymbol{B}}{B^2} \tag{1.47}$$

For $v_{\parallel} = 0$, the particle trajectory is a cycloid in $\boldsymbol{E}, \boldsymbol{V}_E$ plane. The positively charged particles rotate in the left-hand sense with respect to the magnetic field and negatively charged particles rotate in the right-hand sense as shown in Figure 1.2. The

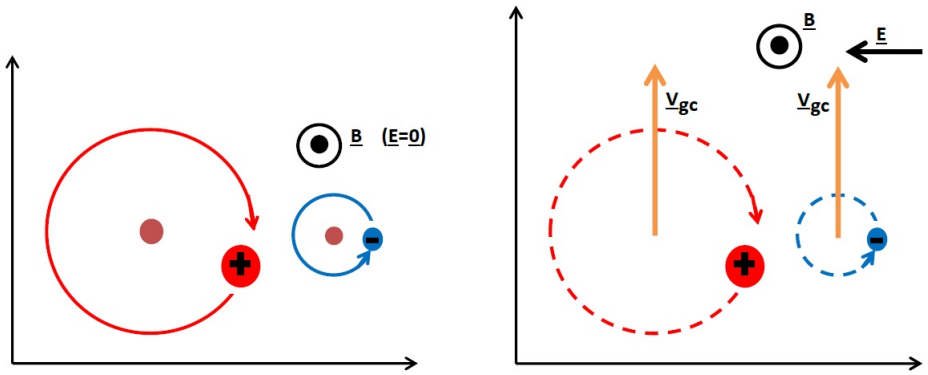

(a) (b)

Figure 1.2: (a) A circular motion of charged particles (proton and electron)in a constant, uniform magnetic field directing out of the page. The particles orbit the guiding centre which is shown in orange. The proton excludes a larger Larmor radius and with the opposite direction to the electron. (b) The drift motion in addition to a circular motion of charged particles in the presence of uniform electromagnetic fields. The guiding centre drifts upwards, in the direction of $E \times B$ with velosity v_{gc} [Bennet (2012)].

guiding centre moving at an $\boldsymbol{E}\times\boldsymbol{B}$ drift velocity. If $v_{\|} \neq 0$, the guiding centre continues to move with this velocity parallel to the magnetic field.

This drift does not depend on the charge or mass of the particle but only on the magnitude and direction of the electric and magnetic fields. This means the guiding centres of both electrons and ions move with the same velocity. Other particle drifts in the magnetized plasma are grad-B drift and curvature drift. The former one forms when the magnetic field is spatially nonuniform and results in the drift of charged particles in opposite directions perpendicular to the magnetic field and its gradient direction. The curvature drift exists in a curved magnetic field and accompanies the grad-B drift. These two drifts are significant in the Tokamak magnetic confinement process because these drifts encourage ions to drift towards Tokamak walls which affect the maintenance of the confinement.

The case when the electric field is spatially non-uniform is different. While drift

velocity is proportional to the kinetic energy and electric field magnitude differs around the grain , the particles gain or lose energy when they move in different regions around the grain. As a result, the cyclotron radius and the drift velocity change.

1.6.4 Energy changes

The Larmor radius increases with the perpendicular velocity. Consider a positively charged particle moving in an electromagnetic field as shown in Figure 1.3(a), when the particle moves in the upper half cycle (from point 1 to 3), the electric field will accelerate it because the particle moves in the direction of the electric field. As a result, the particle will gain energy and its Larmor radius will increase in size, see Figure 1.3(b) .As the particle moves against the electric field in the lower half cycle (point 3 to 1), it slows down and loses energy. The higher velocity on the top portion of the trajectory and the lower velocity on the bottom portion lead to a drift perpendicular to both E and B resulting from the different sizes of the average Larmor radius. However, overall they will gain energy equivalent to moving at the drift speed [Freidberg (2007)].

In the case when the electric field is not constant or not uniform, the particle orbits may be quite complicated and particles can gain or lose energy as they drift into different electrostatic regions due to the work done by the electric field.

1.7 Orbit-Limited Theory

It is common to calculate the charging of dust grains in plasma as well as their shielding by using the orbit-motion-limit (OML) theory for spherical probes [Allen (1992)]. The orbit-motion-limit predicts the electron and ion currents to the probe. The original orbital motion of charged particles around a probe which is attributed to Mott-Smith and Langmuir [Mott-Smith and Langmuir (1926)] assumed particle orbits within the sheath enclosing a spherical or cylindrical probe, whereas plasma outside the sheath is considered to be a neutral.

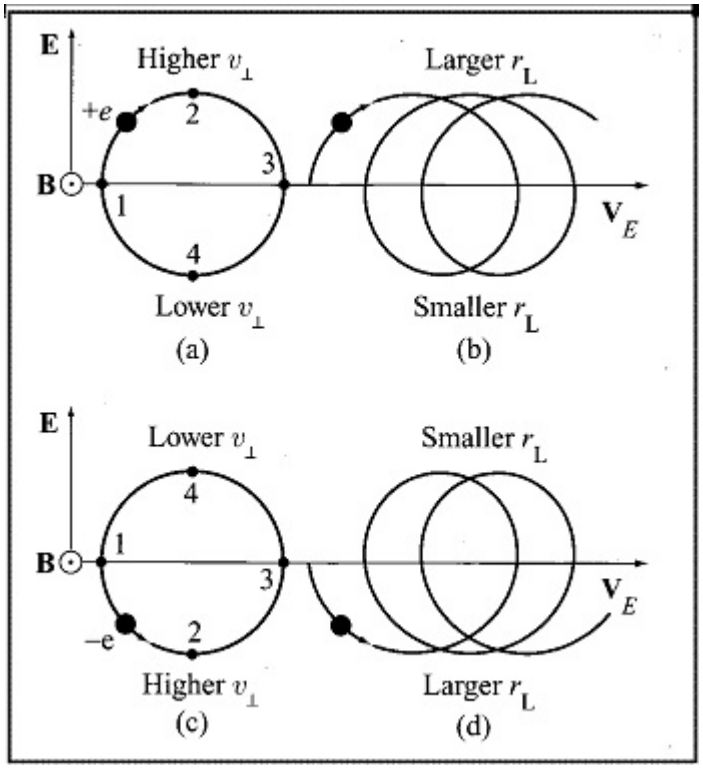

Figure 1.3: (a) Effect of $E_\perp$ on a positive charge and (b) the resulting perpendicular $\boldsymbol{E}\times\boldsymbol{B}$ drift. (c)Effect of$E_\perp$ on a negative charge and (d) the resulting perpendicular $\boldsymbol{E}\times\boldsymbol{B}$ drift [Freidberg (2007)].

The following discussion clarifies the assumptions and equations that OML theory is based on [Allen (1992)]. Consider a cylindrical probe with an attracted potential (consider it at a positive potential). The conservation law of energy gives:

$$\frac{1}{2}mv^2 = \frac{1}{2}mv_p^2 - eV_p \tag{1.48}$$

where v_p is the velocity at the probe surface, and V_p is the probe potential. Conservation of angular momentum gives, for an electron in a close incidence,

$$mvh_p = mr_pv_p \tag{1.49}$$

where $h_p = r_p(1+V_p/V_0)^{1/2}$ is the impact parameter (see Figure 1.4), r_p is the probe radius, and eV_0 is the initial energy of the electron. The previous equation expresses the effective radius of the probe. The electron contribution to the current I to the probe with velocities in a narrow range is given by:

$$dI = 2\pi r_p le(1 + V_p/V_0)^{1/2}(\nu/\pi)dn \tag{1.50}$$

where $(\nu/\pi)dn$ is the electron flux through the unit area for those moving in a direction perpendicular to the probe axis. If we consider a Maxwellian distribution of velocities in two dimensions:

$$dn = n_0\left(\frac{m}{2\pi kT_e}\right)e^{-mv^2/2kT_e}2\pi v dv \tag{1.51}$$

Substituting equation 1.54 in 1.50 and integration gives the total current:

$$I = 2\pi n_0 r_p le\left(\frac{kT_e}{2\pi m}\right)^{1/2}\frac{2}{\sqrt{\pi}}\left(1+\frac{eV_p}{kT_e}\right)^{1/2} \tag{1.52}$$

when $eV_p/kT \geq 2$, then a plot for a relation between I^2 and V_p represents a straight line, with its slope giving n_0 and the intersection with current axis gives T_e. For a spherical probe, the current relation is:

$$I = 4\pi n_0 r_p^2 e\left(\frac{kT}{\pi m}\right)^{1/2}(1 + V_p/V_0) \tag{1.53}$$

For the ion current, the equation becomes :

$$I = 4\pi n_0 r_p^2 e(kT_i/2\pi M)^{1/2}(1 - eV_p/kT_i) \tag{1.54}$$

The theory ignores collisions. However, it is important to include collisions if the theory extends to infinity. Despite this neglect of ion-neutral collisions, OML assumes that the mean free path is much longer than the Debye length [Chen (2009)].

OML theory also neglects the presence of potential barriers. This means ions can reach positive energy points in phase space .The OM theory by Laframboise [Laframboise (1966)] shows that in the limit $r_p \ll \lambda_D$, the results reduce to the simpler OML theory in which there is no absorption radius in that limit. However, Allen et al.[Allen

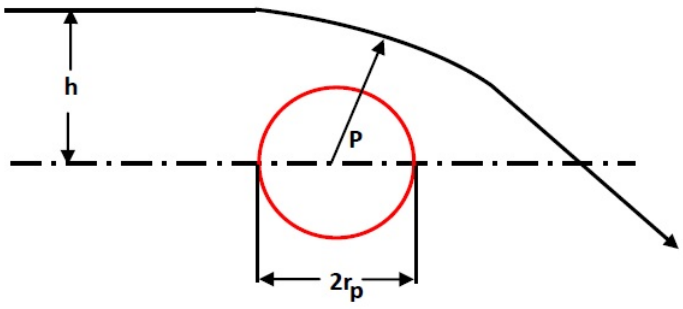

Figure 1.4: Plot illustrates the impact parameter h and the closest approach distance p.

et al. (2000)] have confirmed for any negatively charged dust grain in a Maxwellian plasma, the role of potential barriers in preventing some ions from reaching dust should be considered. It has been shown [Lampe (2001b)] that the OML theory is very accurate when used for small grain size, and in calculating the ion current to the grain and the floating potential. However, potential barriers can have some effects on the potential shielding at limit $r_p \approx \lambda_D$ particulary for large dust size, and low T_i/T_e.

1.8 Gas molecule processes

The presence of charged dust grains in plasma can lead to activation of ambient neutral gas. In this section some aspects of gas molecule processes such as excitation, ionization, radiation and metastable formation that can appear [Lieberman and Lichtenberg (2005)]are discussed.

1.8.1 Electric Radiation and Metastable formation

Atom collisions with charged particles or expose to radiation can lead to atom excitation where the atoms in a ground state transfer to a higher energy bound state. In most bound states atoms emit photons by electric dipole radiation before returning to the

ground state or to a lower energy bound state:

$$e + Ar \rightarrow Ar^* + e \rightarrow Ar + e + \hbar\omega \tag{1.55}$$

where ω is the photon frequency, and $\hbar\omega$ is its energy. This radiation is often in the visible or ultraviolet ranges. It has be shown that the excited states lose energy by electric dipole radiation more often than through collisions. A special excited state where the dipole radiation is not allowed is called metastable, instead the particle can relax by radiating as a quadrupole or through magnetic dipole radiation. However, metastable atoms can be de-excited or ionized by collisions. Metastables states are implicated in He-Ne gas lasers. A e-He collision results in Helium atom He excitation which becomes de-excited by another collision with Ne atoms. Consequently, Ne atoms become excited and then start to radiate leading to laser formation.

1.8.2 Electron Impact Ionization

Since an electron-atom can lead to excitation of the atom or to electric radiation, high energy electrons (higher than ionization energy ε_{ioz}) can produce atom ionization. An incident electron has energy ε and can transfer part of its energy (equal to ionization energy) to a target which loses an electron leading to the ionization of the target. Ionization collisions cross section depend on the incident electron energy. For $\varepsilon < \varepsilon_{ioz}$, the $\sigma_{ioz} = 0$ where σ_{ioz} is the ionization cross section. The ionization cross section [Lieberman and Lichtenberg (2005)] can be given by:

$$\sigma_{ioz} = \pi \left(\frac{e}{4\pi\epsilon_0} \right)^2 \frac{1}{\varepsilon} \left(\frac{1}{\varepsilon_{iz} - \frac{1}{\varepsilon}} \right) \tag{1.56}$$

where:

$$\varepsilon > \varepsilon_{ioz} \tag{1.57}$$

For an electron energy much more than ionization energy, the cross section falls probational to ε^{-1}. Like the ionization cross section, the ionization frequency also falls

with v^{-1} when $\varepsilon \gg \varepsilon_{ioz}$, where v is the electron velocity. The ionization frequency is given by:

$$\nu_{ioz} = n\sigma_{ioz}v \tag{1.58}$$

Since there is usually a distribution of electron energies in any realistic plasma, the tail of such a distribution is significant in ionization process.

1.9 Thesis Outline

The goal of this thesis is to investigate some essential physical processes leading to dust grain growth and their interactions in plasmas. This introductory chapter introduces a short discussion of the basic physical background related to the subject in hand. The following chapters will discuss in greater details the physical mathematical and computational treatment of the research carried out for this thesis.

The first subsequent chapter will discuss the mathematical and computational techniques used in dust grain simulations. Chapter 2 will introduce the particle model including the Monte-Carlo collision . Field solver in addition to the Lagrange multiplier techniques that will be investigated in chapter 3. Poisson's equation will be solved using the Finite Difference method to calculate the electric potential of charged dust grains in 3 dimensions as well as the electric potential resulting from the charged particles. Furthermore, 1-D examples of dust growth will be presented in chapter 3. The model introduced in Chapter 2 as well as the numerical techniques discussed in Chapter 3 will be utilized in Chapter 4 and simulation results will be discussed. Chapter 5 will investigate the possible gas discharge processes that can occur in the environment of charged dust grains in plasma that can be measured in submicron scales. Chapter 6 will address a specific case for various dust interactions and their role in the formation of electron beams above a thundercloud. The simulation results will also be discussed. Chapter 7 is the conclusion, and will examine the possible extension of the work presented in this thesis.

2

Particle model

2.1 Introduction

This chapter introduces the particle model which will be applied in the simulation of charged particles' (electrons and ions) dynamics in the coming chapters. The particle model and its different aspects, such as collision processes, data interpolation and other components are described here in detail. In addition to particle model, other techniques, namely the Poisson solver and the Lagrange multiplier will be incorporated in simulations and are the subject of chapter 3.

2.2 Interpolation

Interpolation is a method which is quite commonly used for the particle model. This process allows the estimation of a function $f(x, y)$ at untabulated points (x, y). In the particle model, scaler quantities, for example the electric potential, are defined at grid points. However, the computing of particle positions and velocities is required in a continuous way in the computational domain. On the other hand, whilst particles can move to positions that don't coincide with grid points, their charge must be assigned to the nearest set of grid points in order to allow the calculation of the electric potential.

The simplest interpolation method which applies the nearest grids points is the

linear interpolation [Press (1992)] (or bilinear and trilinear interpolation in two and three dimensions respectively). In such a method, the data at grids points are used to find the value in the internal desired points or a value weighted to the nearest mesh points.

In order to clarify the concept of the linear method the following example is considered: in two dimensions if $ya(j,k)$ is an array of functional values, $x1a$ is a given array of length m, and $x2a$ is an array of length l . These three arrays are combined by the following relation:

$$ya(j,k) = y(x1a(j), x2a(k)) \tag{2.1}$$

To estimate the value of function y at internal point $(x1, x2)$ by bilinear interpolation, the four mesh points which surround the desired point, as shown in Figure 2.1 , are related to point $(x1, x2)$ by relations:

$$x1a(j) \leq x1 \leq x1a(j+1) \tag{2.2}$$

$$x2a(k) \leq x2 \leq x2a(k+1) \tag{2.3}$$

The following relations are then considered:

$$y_1 = ya(j,k) \tag{2.4}$$

$$y_2 = ya(j+1,k) \tag{2.5}$$

$$y_3 = ya(j+1,k+1) \tag{2.6}$$

$$y_4 = ya(j,k+1) \tag{2.7}$$

The value of ya at point $(x1, x2)$ is given by:

$$y(x_1, x_2) = (1-t)(1-u)y_1 + t(1-u)y_2 + tuy_3 + (1-t)uy_4 \tag{2.8}$$

where:

$$t = (x_1 - x1a(j))/(x1a(j+1) - x1a(j)) \tag{2.9}$$

$$u = (x_2 - x2a(k))/(x2a(k+1) - x2a(k)) \tag{2.10}$$

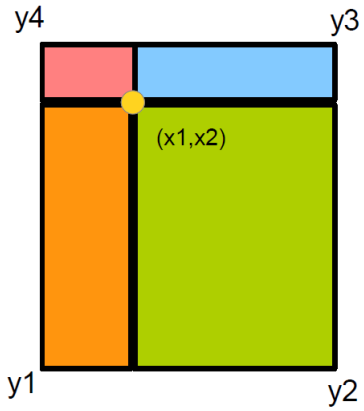

Figure 2.1: Interpolation diagram.

Similarly, when interpolation to mesh points is done, the internal value weighting is applied to the surrounding grids hence the greatest weight is attributed to the nearest grid point weighting the particle to the grid points, the largest weight is attributed to the nearest grid point then; it follows that:

$$y_1 = \left(y(x_1, x_2) - t(1-u)y_2 + tuy_3 - (1-t)uy_4 \right) / (1-t)(1-u) \quad (2.11)$$

$$y_2 = \left(y(x_1, x_2) - (1-t)(1-u)y_1 + tuy_3 - (1-t)uy_4 \right) / t(1-u) \quad (2.12)$$

$$y_3 = \left(y(x_1, x_2) - (1-t)(1-u)y_1 - t(1-u)y_2 - (1-t)uy_4 \right) / tu \quad (2.13)$$

$$y_4 = \left(y(x_1, x_2) - (1-t)(1-u)y_1 - t(1-u)y_2 + tuy_3 \right) / u(1-t) \quad (2.14)$$

Taking a simple case when $t = 0$ and $u = 0$, the value of the function lies on a mesh point. The method can similarly be applied to three-dimensions.

2.3 Integration of particle motion

The coupled set of equations of motion that describe the individual particles motion are as follows;

$$\mathbf{F} = m\frac{d\mathbf{v}}{dt} = q(\mathbf{E} + \mathbf{v} \times \mathbf{B}) \quad (2.15)$$

$$\mathbf{v} = \frac{d\mathbf{r}}{dt} \tag{2.16}$$

equations 2.15, and 2.16 are ODE's (Ordinary Differential Equations).

One effictive method for solving initial value problems for ODE's is the Runge-Kutta method [Press (1992)]. It is derived from a convenient Taylor method that expanded to some n order terms, in which $4^{th}RK$ is equated to the first five terms of Taylor expansion, and the error term is of order of 5. In RK method the function $f(x,t)$ is evaluated at selected points on each step size. This method is stable and converges to a good level. To illustrate the idea of the Runge-Kutta algorithm, let's consider an ODE:

$$\frac{dy}{dx} = f(x,y) \tag{2.17}$$

when subject to an initial value $f(x) = x_0$ at $x = 0$. The $4^{th}RK$, evaluate $f(x)$ four times per step h: Once at the initial point, twice at trial midpoints and once at a trial end point. The final value of the function is computed from these four derivatives. The fourth Runge-Kutta formula therefore has the form:

$$y_{n+1} = y_n + \frac{k_1}{6} + \frac{k_2}{3} + \frac{k_3}{3} + \frac{k_4}{6} + O(h^5) \tag{2.18}$$

in which:

$$k_1 = hf(x_n, y_n) \tag{2.19}$$

$$k_2 = hf(x_n + \frac{h}{2}, y_n + \frac{k_1}{2}) \tag{2.20}$$

$$k_3 = hf(x_n + \frac{h}{2}, y_n + \frac{k_2}{2}) \tag{2.21}$$

$$k_4 = hf(x_n + h, y_n + k_3) \tag{2.22}$$

$O(h^5)$ is the error term of fifth order which indicates that each time step has an error with an order five, as lower order errors are canceled out by each other.

2.4 Particle in cell simulation

Many plasma simulations are intended to calculate the dynamics and possible collisions of each particle. However, the large number of these particles in many plasma environments makes this process difficult or even impossible. Therefore, the super-particles technique has been introduced to represent the huge number of particles in one super particle. In our simulations in this thesis only real particles are considered, otherwise other PIC techniques are the same. The super-particle behaves in the same way the real particle does by interacting with self fields and obeying Lorentz force equations. Such simulation is known as the Particle-in-Cell [Petrovi et al. (2007)].

PIC simulation details can be found in many prior works, such as [Dowds et al. (2003b), and MacLachlan (2009)]. The simulation begins by injecting the super-particles into the computational domain and then their self fields are computed from the particles' positions and velocities via equations of motion under the influence of the outer fields. The interpolation process is used to weight the particles' charges to the mesh points then solve Poisson equation. The electric fields are then calculated and weighted to the particle positions through the simulation space. The new particles' velocities and positions are then updated. Collisions between particles or neutrals are simulated using a Monte-Carlo algorithm.

2.5 Monte Carlo method

The ideal particle model must include a treatment of particle collisions. This requires us to add a new term to the equations of motion to include collisions. Equation 2.15 can be written as:

$$\mathbf{F} = m\frac{d\mathbf{v}}{dt} = q(\mathbf{E} + \mathbf{v} \times \mathbf{B}) + \mathbf{K} \tag{2.23}$$

where K is the collision term. Two important parameters in collision treatment are the collision cross-section and the rate coefficient. A collision cross-section describes a target particle interaction area which causes a reaction if intersected by the colliding

particle. The cross-section is often dependent on energy. If particles with a distribution of energies involved in collisions, then their rate coefficient combines the information from the cross-section and the energy distribution. The rate coefficient is often used in a fluid model; however, as the work here is dealing with individual particles, then its treatment of collisions should use individual cross-sections. A common method to deal with collision processes is a Monte Carlo collision (MCC) [Birdsall (1993)] scheme which treats the collision processes using statistical methods. The type of the collision should be determined after the collision occurring decision. The cross sections of each interaction in addition to the particle energy are crucial parameters to decide that a collision has occurred.

When an electron gains enough energy to cause a specific collision, such a collision is considered to take place.

The probability, P, of the incident particle having a collision at a time step is expressed as:

$$P = n_t v \Delta t \sum_{i=1}^{M} \sigma_i \epsilon \tag{2.24}$$

where n_t is the number density of the targets, v is the speed, Δt is the computational time step size, σ_i is the i^{th} cross-section of a collision at particle energy ϵ, the sum in equation 2.24 represents the total cross sections of all collisions types, and M is the total number of collision types. The simulation is easy to extend to include any number of collision types with heavier loads on the computer. If a target species includes more than one type, the probability expression can easily be modified to consist of different target species types. The collision probability at each time step is determined by comparison of the probability with a random number. Another random number is compared with the probability of each collision kind to determine the type of the incident collision . The probability of a collision can be given for each collision type as:

$$P_i = n_t v \Delta t \sigma_i(\epsilon) \tag{2.25}$$

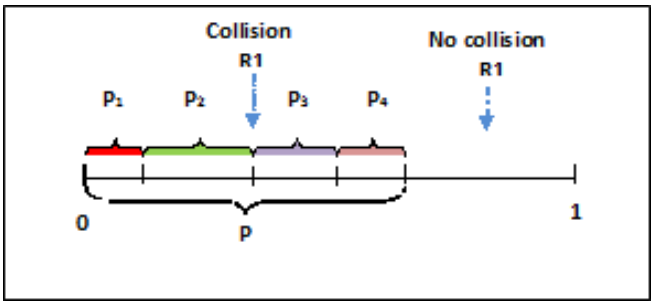

Figure 2.2: Diagram showing a straightforward Monte-Carlo collision selection method. The line shows the choice between a collision and no collision. A collision occurs if the random number R_1 is less than the total collision probability.

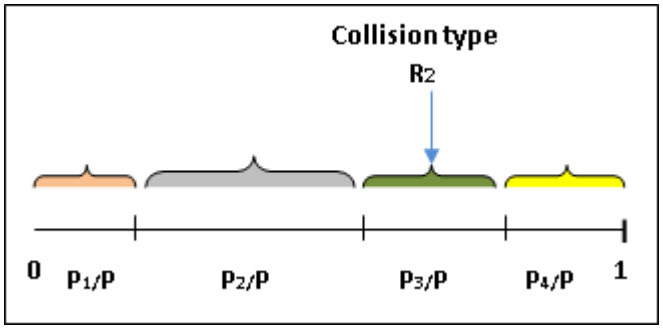

Figure 2.3: Diagram showing a straightforward Monte-Carlo collision selection method. After deciding between a collision or no collision by comparison a first random number with the total probability, the type of collision is chosen: a second random number is compared to the relative sizes of each collision probability.

where P_i is the probability of the i^{th} collision kind. If a generated random number ($R1$) selected from a uniform distribution of numbers of between 0 to 1 is less than the total probability of simulated collisions then the incident particle must undergo a collision. In order to decide the collision type, another random number ($R2$) is compared with the relative probabilities (P_i/P). Diagrams 2.2, and 2.3 clarify the Monte-Carlo ideas described above.

Molecular gases can be involved in many inelastic reactions, such as attachment, dissociation, charge exchange, or ionisation . These reactions can change the chemical composition of the plasma. In addition, there are different kinds of elastic collisions,

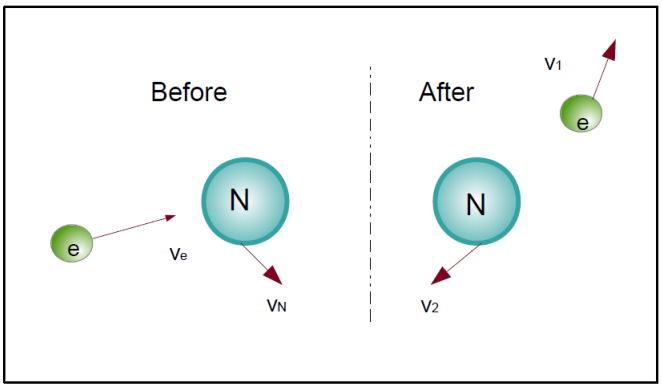

Figure 2.4: Figure showing pre- and post-collison dynamics for an elastic collision between an electron and a neutral.

for example, vibrational, rotational, and electronic excitations. These excitations affect the energy distributions of the particles. A general description of how Monte-Carlo method treats some of these interactions now follows,

2.5.1 Elastic collisions

In an elastic collision, momentum and the total kinetic energy are redistributed between the particles involved [Braithwaite (2000)] , e.g.

$$e^-_{fast} + A_{slow} \rightarrow e^-_{lessfast} + A_{lessslow} \tag{2.26}$$

As a result of an electron losing energy, it follows a scattered direction. The scattering angle θ in the range of $[-\pi : \theta]$ can be expressed by a simple relation [Dowds et al. (2003b)] as;

$$\theta = 8\pi(R - \frac{1}{2})^3 \tag{2.27}$$

where R is a random number between 1 and 0. There is no energy threshold for elastic collisions. Figure 2.4, above, shows the properties of an elastic collision.

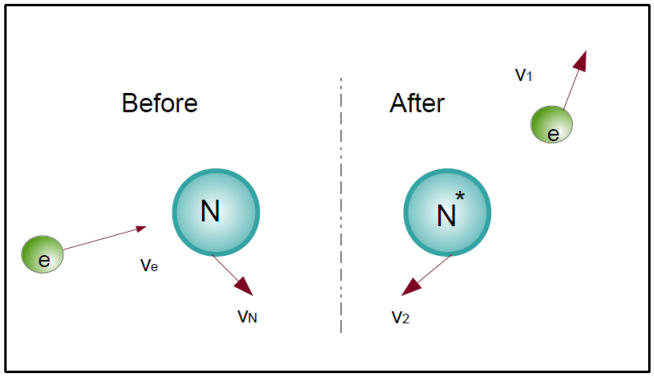

Figure 2.5: Figure showing pre- and post-collision dynamics for an inelastic collision between an electron and a neutral.

2.5.2 Inelastic collisions

Here, momentum is redistributed between the colliding particles; however, part of the kinetic energy is transferred from one particle to the others, resulting in a state of excitation or ionization. Figs. 2.5, and 2.6 show the properties of inelastic and ionization collisions respectively.

$$e^-_{fast} + A \rightarrow e^-_{slower} + A^* \tag{2.28}$$

or,

$$e^-_{fast} + A \rightarrow 2e^- + A^+ \tag{2.29}$$

A particular excited state of an atom or molecule that has a longer lifespan than the usual excited states is known as metastable state. Therefore, a metastable can survive to undergo a second collision that may transfer it to an ionized state. The ionization process results in two electrons; the incident, plus another, leaving a positive ion.

The ionising electron's initial speed and the neutral speed in lab frame are v_e and v_n respectively, and the postcollision speeds of the ion and two electrons in the same frame are v_n, v_1 and v_2 respectively. The neutral speed is assumed to be unchanged pre- and postcollision. In the rest frame of neutral [Lieberman and Lichtenberg (2005), and

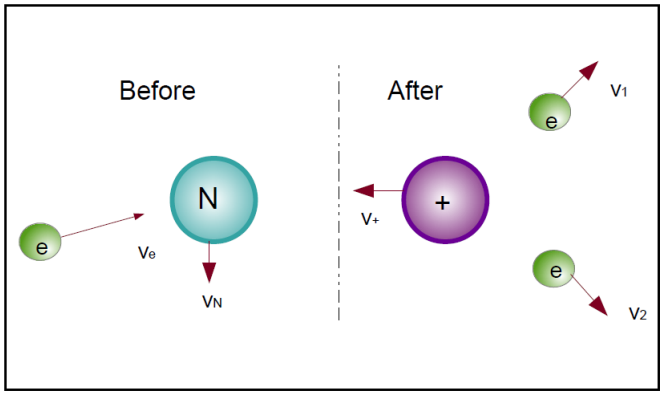

Figure 2.6: Figure showing pre- and post-collision dynamics for an ionization collision between an electron and a neutral.

MacLachlan (2009)] the velocities of the ionizing electron and the neutral are:

$$u_e = v_e - v_n \tag{2.30}$$

$$u_n = 0 \tag{2.31}$$

move into the centre of momentum frame gives:

$$u_e = u_n - u_{cm} \tag{2.32}$$

$$u_n = -u_{cm} \tag{2.33}$$

$$u_{cm} = \frac{m_e u_e}{m_e + m_n} \tag{2.34}$$

The energy during the collision is given by:

$$\varepsilon_e + \varepsilon_n = \varepsilon_1 + \varepsilon_2 + \varepsilon_+ + \varepsilon_{iz} \tag{2.35}$$

The post collision energy,$'\varepsilon'_{post}$, is:

$$\varepsilon_{post} = \varepsilon_e + \varepsilon_n - \varepsilon_{iz} \tag{2.36}$$

where ε_e is the incident electron energy, ε_n is the neutral energy, ε_+ is the ion energy, ε_{iz} is the ionisation energy, and ε_1 and ε_2 are the energies of the post-collision electrons. The post collision momentum is given by the relation:

$$m_e u_1 + m_e u_2 + m_+ u_+ = 0 \tag{2.37}$$

The energy that an ion can acquire through the collision is a random fraction of:

$$max(\varepsilon_+) = \frac{m_e}{m_e + m_+}\varepsilon_{post} \tag{2.38}$$

The rest of the energy must be shared randomly between the electrons. Another random number is used to calculate the trajectory (ϕ_1, θ_1) of the first electron:

$$u_1 = \sqrt{\frac{2\varepsilon_1}{m_2}}(\sin\phi_1 \cos\theta_1, \sin\phi_1 \sin\theta_1) \tag{2.39}$$

where $\theta_1 \in [0 : \pi]$ and $\phi_1 \in [0 : 2\pi]$ $\phi_1$usually has an isotropic distribution:$\phi_1 = R2\pi$, whereas θ_1 has a non-isotropic distribution $\theta_1 = \cos(1 - 2R)$

The second electron's velocity can be calculated via the conservation of momentum:

$$u_2 = -\frac{m_e u_1 + m_+ u_+}{m_e} \tag{2.40}$$

Finally, the velocities of electron and ion must be transformed back into the lab frame by adding in the initial neutral velocities and the centre of momentum. The work in this thesis considers the ion to be stationary, and so only the electrons share the postcollision energy.

2.6 Algorithm

The particle model strategy described above can be ordered into the following steps:

- Initial conditions, such as the initial particle positions and velocities, the time step size, number of steps and all nondimensional parameters, are determined. The size of the time step is chosen to give a good resolution without a big load on computer. This can be achieved by the trail and error.

- To calculate the trajectories and velocities of particles, the following procedures are then followed:

  - Computing the charge density of the charged particles through grids using the following equation:

$$\rho = e(n_+ - n_-) \tag{2.41}$$

where e is the electron charge, n_- is the electron density, and n_+ is the positive ion density. The method of interpolation explained above is used to assign particle charge to the surrounding grid points.

- Calculating the electric potential via a Poisson's equation:

$$\nabla^2\phi = \frac{\rho}{\varepsilon_0} \tag{2.42}$$

where ε_0 is the permittivity of free space, ϕ_0 is the electric potential, and ρ is the charge density. Further details regarding this step are found in chapter 3.

- Calculating the electric fields from the gradient of the electric potential.
- Applying the fourth-order Runge-Kutta method on the equations of motion to get the updated positions and velocities of particles.

- Determining the energy of every particle to study the possibility of collisions occurring and their effects on particle velocity.
- Updating the position and velocity of every particle postcollision.
- Storing all data in a file.
- Repeating the previous steps.

2.7 Particle model test: a simple 1D Dust grain growth treatment

This section aims to apply and test some of the aspects of the particle model explained earlier. Collisions will not be included here as they will be investigated in chapter 5.

Neither the self fields of the ions nor of the electrons will be considered here. Instead, the electric field will be given by analytical expressions depending on the particles' positions. This section addresses the basic model of dust growth by ion accretion and takes 1D dust to be a simple starting example.

Much prior researches have been done on the physical mechanisms that lead to dust formation [Patzer et al. (1995),Nuth et al. (2002)] and on spheroidal dust grains' impact on the transmission of electromagnetic radiation.

Stark et al.[Stark et al. (2006)] investigated the growth of elliptical dust grains via plasma deposition and showed that this growth depends on the initial kinetic energy of the ions and the magnitude of the electric field in the grain sheath. Ions with a potential energy in the sheath which is much greater than their initial kinetic energy cause elongated growth for grains above a certain eccentricity.

The growth of elliptical dust grains in many astrophysical and laboratory environments may require magnetic fields to be involved the calculations. In addition to the electrostatic fields arising from the dust grains themselves, perpendicular and parallel orientated magnetic fields will also be respectively considered . The results presented in this chapter will later be compared with the results of the $3D$ simulations which were carried out in chapter 4.

2.8 Charging of dust grains in plasma

The charging of dust grains in plasma occur through several methods; for example, dust in astrophysical environments is usually charged electrostatically by the absorption of charged particles. In addition to the photo ionization involving incidents of energetic photons leading to the positive charge of the grains.

Dust particles acquire charges when they are immersed in plasma. Ions and electron currents flow to dust particles; however, dust grains charge negatively because of the high mobility of the electrons. The negative-potential dust surfaces will be surrounded by positive particles (ions) because the grains attract ions and repel elec-

trons. These positive ions partially screen the negatively charged grains in a phenomena called 'Debye screening'. From the OML theory, the ion and electrons currents which are collected by a spherical probe with radius a are [Lieberman and Lichtenberg (1994)]:

$$I_e = -I_{e0} \exp(\phi_d / T_e) \tag{2.43}$$

$$I_i = I_{i0}(1 - \phi_d / T_e) \tag{2.44}$$

where ϕ_d is the probe (or the dust) potential, and T_e is the electron temperature. If one assumed isotropic Maxwellian distribution of both electrons and ions in the Debye sphere, then:

$$I_{e0} = \frac{1}{4} e n_e \bar{v}_e . 4\pi a^2 \tag{2.45}$$

$$I_{i0} = \frac{1}{4} e n_i \bar{v}_i . 4\pi a^2 \tag{2.46}$$

where a is the probe radius, $\bar{v}_e = (8eT_e/\pi m)^{1/2}$ and $\bar{v}_i = (8eT_i/\pi M)^{1/2}$. In case of equilibrium, in which no secondary and field emission of electrons are occurred from the dust surface, the ϕ_d is given by the total currents of ions and electrons. Using equations 2.43 and 2.45, and taking the logarithm gives:

$$\phi_d = -T_e \left[ln\left(\frac{M}{m} \frac{T_e}{T_i} \frac{n_e^2}{n_i^2} \right) - ln\left(1 - \frac{\phi_d}{T_i} \right) \right] \tag{2.47}$$

An analytic expression for ϕ_d is given by:

$$\phi_d \approx -0.73 T_e ln\left(\frac{M}{m} \frac{T_e}{T_i} \frac{n_e^2}{n_i^2} \right) \tag{2.48}$$

The charge on the dust surface can be found when the potential is known from the relation:

$$Q_d = C_d \phi_d \tag{2.49}$$

where the particle capacitance is given by:

$$C_d = 4\pi\epsilon_0 a e^{a/\lambda_D} \tag{2.50}$$

when $a \ll \lambda_D$:

$$C_d = 4\pi\epsilon_0 a \tag{2.51}$$

In low temperature laboratory plasma , the dominant charging process is the absorption of free charge. This study focus on charging of dust grains by absorbtion of charged particles. Studying and understanding single particle dynamics is important in building a fuller knowledge of plasma processes. The interaction of dust grains with magnetized plasma influences the levels of nucleation and agglomeration. We will consider the spatially nonuniform electric field of a charged wire and a constant magnetic field.

2.9 Model of 1D treatment of dust growth

In our model we consider a steady state magnetised plane parallel plasma sheath in contact with the grain. Also, the magnetic field is chosen to be in z and x directions (perpendicular and parallel to the grain, respectively). The sheath edge separates the quasineutral plasma and the sheath region. It is assumed that the sheath consists of cold ions and isothermal electrons to be in thermal equilibrium state. At the sheath edge, the electric potential is taken to be zero. The sheath confines the electrons in the plasma and accelerates the ions out of the plasma. The ions are accelerated into the plasma-sheath boundary with critical velocity. The minimum value of the ion-entering velocity is determined by Bohm criterion [Hershkowitz (2005)]. For a colisionless sheath, this minimum value is regarded as the ion sound speed. Therefore, for ions entering the sheath region ,the minimum velocity divided by the ion sound speed (which is known as Mach number) must be greater than unity, hence,

$$M \geq 1 \tag{2.52}$$

However, in our model the ions are launched within the sheath with launch velocity v_{launch} at $t = 0$, and at a perpendicular distance = $\sqrt{\hat{x}^2 + \hat{y}^2 + \hat{z}^2}$ from the grain, where $(\hat{x}, \hat{y}, \hat{z})$ is the initial position of the ion, and the grain is parallel to the x axis. In such

Table 2.1: Parameters used in numerical simulations.

Simulation property	Value
Number of launched ions	10^4
p	1
$d\hat{t}$	0.1
number of time steps	1500
ϕ	$-10V$
L	10
x	$-L/2$ to $3L/2$
y	$L/5$

a model, the grain size is assumed to be much smaller than the sheath length. If we assume astrophysical dust, the size of dust in the model is in the range of micrometers while the sheath is in the range of metres. The number of lunched ions toward the grain surface is 10^4 ions to be consistent with the astrophysical regime, especially the Coulomb crystal dust (see table 2.2. The ions distributed along the x-axis (initial $\hat{x} = -L/2$ to $\hat{x} = 3L/2$, and initial $\hat{y} = L/5$). To ensure that the ions hit the grain, the perpendicular launch distance is chosen to be smaller than the ions Larmor radius ($\hat{y} < R_L$). The parameter p is set to one in the simulation. Table **??** represents the parameters used in this simulation.

2.9.1 Electric field around a charged wire

To start with a simple model of dust growth, a thin long grain of finite length is considered. The electric field of such a model can easily be obtained using direct formulas. That simplicity allows us to gain a clear insight into the dynamics of dust growth in the presence of an electrostatic and magnetostatic fields. Furthermore, it is a good test of some of the technics of the particle model described before. Other aspects of our particle model will be taken into consideration in the later chapters of this thesis. In

simulating a long thin grain as a simple wire in terms of the electric field that is generated by it when the wire is charged, the goal is to consider the trajectories of the ions falling under the influence of such a field in combination with a global, uniform magnetic field. Presently, we consider an infinitely thin, uniformly charged wire of a finite length L ($L = 10$ in our simulation) with a charge per unit length λ. First we consider the x component of the field at $P(a, b, c)$. The element of charge is $dq = \lambda dx$ for the elemental length dx located at position x, as shown in figure 2.7. The electric field vector arising from a charge q located at distance r is given by $E = \frac{q}{2\pi r^2}\hat{r}$ [Tipler and Mosca (2007)]. Hence the electric element in the x direction arising from the charge element in the diagram must be

$$dE_x = \frac{\lambda dx}{4\pi\varepsilon_0 r^2}\sin\theta = \frac{\lambda}{4\pi\varepsilon_0}\frac{xdx}{(x^2+b^2)^{\frac{3}{2}}} \tag{2.53}$$

Integrating from $x = -a$ to $L - a$ yields the x-component of electric field

$$E_x(a,b) = \frac{\lambda}{4\pi\varepsilon_0}[\frac{1}{\sqrt{a^2+b^2}} - \frac{1}{\sqrt{(L-a)^2+b^2}}] \tag{2.54}$$

The same operation can be carried out for the electric field in the y-direction

$$E_y(a,b) = \frac{\lambda}{4\pi\varepsilon_0 b}[\frac{L-a}{\sqrt{(L-a)^2+b^2}} + \frac{a}{\sqrt{a^2+b^2}}] \tag{2.55}$$

The x-component, y-component, and the resultant ($E = \sqrt{E_x^2 + E_y^2}$) of the electric field of the wire can be seen in Figs. 2.8, 2.9, and 2.10. The x-component of the electric field becomes extremum at points $(0, 0)$ and $(10, 0)$ as shown in 2.8, while the y-component of the electric field becomes extremum above and bottom the charged wire as shown in figure 2.9. Figure 2.10 shows that the electric field of the wire reaches its maximum around the wire and then decreases gradually while moving away from the wire. Overall, it can be observed that the electric field of the charged wire is spatially non-uniform in magnitude and also that it changes its direction at the wire ends.

In case of a presence of a parallel magnetic field to the grain's long axis, the $x-, y-, z-$ components of grain electric field are needed:

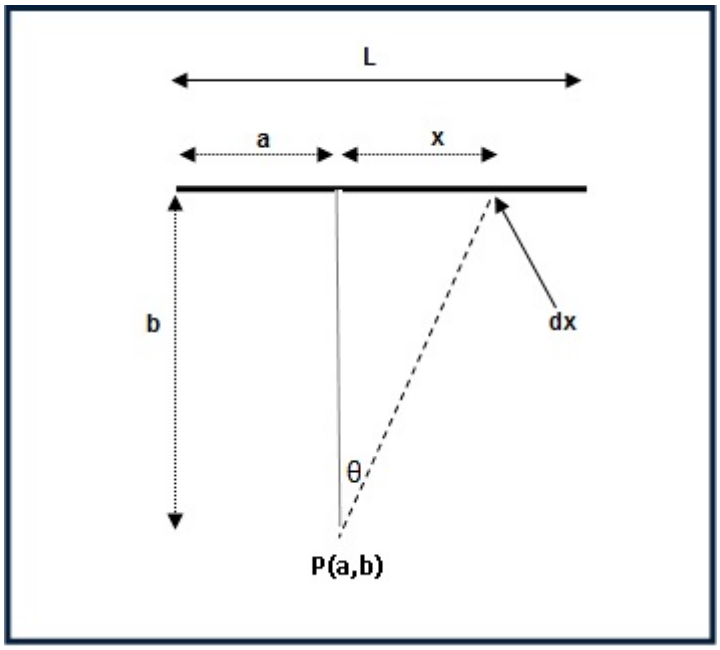

Figure 2.7: An infinitely thin, non-uniformly charged wire of finite length L in xy dimensions.

$$E_x(a,b,c) = \frac{\lambda}{4\pi\varepsilon_0}\left[\frac{1}{\sqrt{a^2+r^2}} - \frac{1}{\sqrt{(L-a)^2+r^2}}\right] \tag{2.56}$$

$$E_y(a,b,c) = \frac{\lambda}{4\pi\varepsilon_0 b}\left[\frac{L-a}{\sqrt{(L-a)^2+r^2}} + \frac{a}{\sqrt{a^2+r^2}}\right] \tag{2.57}$$

$$E_z(a,b,c) = \frac{\lambda}{4\pi\varepsilon_0}\left[\frac{1}{\sqrt{a^2+r^2}} - \frac{1}{\sqrt{(L-a)^2+r^2}}\right] \tag{2.58}$$

where,

$$r = \sqrt{b^2+c^2} \tag{2.59}$$

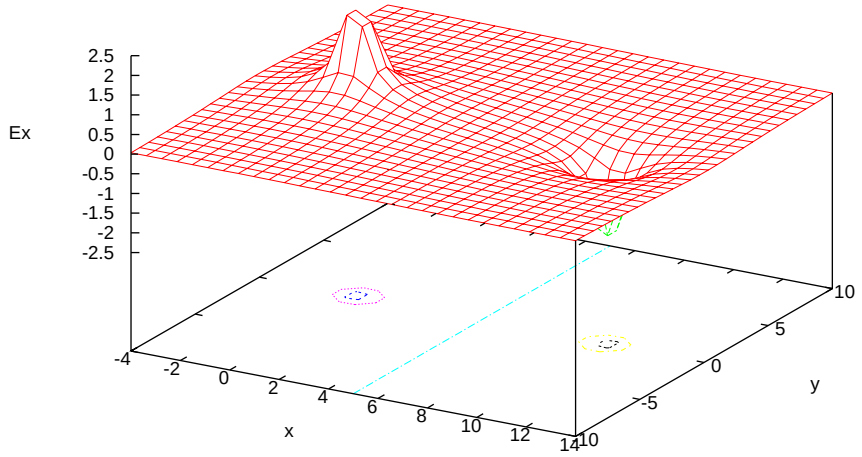

Figure 2.8: The x-component of the electric field for a charged wire. The x-component of the electric field becomes extremum at points $(0, 0)$ and $(10, 0)$.

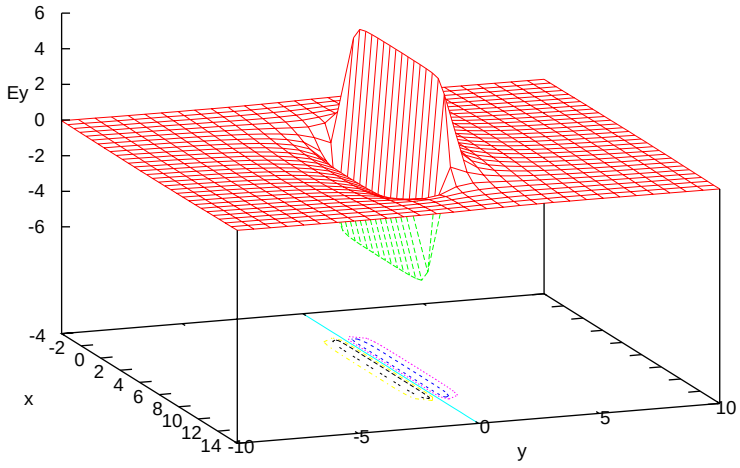

Figure 2.9: The y-component of the electric field for a charged wire. The y-component of electric field becomes extremum above and below the charged wire.

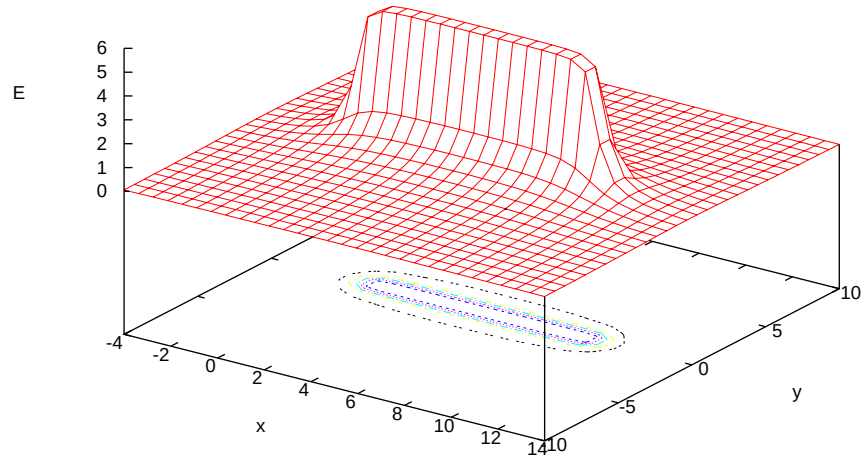

Figure 2.10: The electric field for a charged wire. The electric field of the wire becomes extremum around the wire and then decreases gradually while moving away from the wire.

2.9.2 Model equations

The equations of motion of a charged particle in presence of electric and magnetic fields are re-iterated again here:

$$F = m\frac{d\mathbf{v}}{dt} = q(\mathbf{E} + \mathbf{v} \times \mathbf{B}) \tag{2.60}$$

$$\mathbf{v} = \frac{d\mathbf{r}}{dt} \tag{2.61}$$

To simplify these equations, we select some appropriate non-dimensional variables, $u = v/v_0$, $e = E/E_0$, $b = B/B_0$, and $\hat{t} = t/t_0$, where v_0 is a characteristic speed, t_0 is a characteristic time, and E_0 is a characteristic field.

Model equations are derived in two cases: in the presence of perpendicular orientated magnetic fields with respect to the long axis of the charged wire, and in the presence of parallel magnetic fields.

Perpendicular magnetic fields

Non-dimensional equations in two dimensions xy (when magnetic field lines are directed perpendicularly to the wire) take the following forms:

$$\begin{aligned} \frac{du_x}{d\hat{t}} &= pe_x + su_y b \\ \frac{d\hat{x}}{d\hat{t}} &= u_x \\ \frac{du_y}{d\hat{t}} &= pe_y - su_x b \\ \frac{d\hat{y}}{d\hat{t}} &= u_y \end{aligned} \tag{2.62}$$

where $p = t_0 q E_o/(v_0 m)$ and $s = qB_0 t_0/m$ are non-dimensional parameters, $\hat{x}$ and $\hat{y}$ are the non-dimensional positions of the particle. We will consider B as uniform in space. To simplify the equations, we can choose $t_0 = 1/w_c$, where w_c is the cyclotron frequency, $s = 1$, and $p = qE_0/(mw_c v_0)$. By altering p the ratio of the electric field to the magnetic field can be changed. It is noticeable that it is impossible to set B=0 formally in these equations (2.63) since these equations will vanish, instead different normalisation of the equations of motion are required. Equations 2.63 can be written as:

$$\begin{aligned} \frac{du_x}{d\hat{t}} &= pe_x + u_y b \\ \frac{d\hat{x}}{d\hat{t}} &= u_x \\ \frac{du_y}{d\hat{t}} &= pe_y - u_x b \\ \frac{d\hat{y}}{d\hat{t}} &= u_y \end{aligned} \tag{2.63}$$

Parallel magnetic fields

Applying the same approach as previously, and using non-dimensional variables in equations of motion, when applying parallel magnetic fields, non-dimensional equations extend to three dimensions and take the following forms:

$$\begin{aligned}
\frac{du_x}{d\hat{t}} &= pe_x \\
\frac{d\hat{x}}{d\hat{t}} &= u_x \\
\frac{du_y}{d\hat{t}} &= pe_y - su_z b \\
\frac{d\hat{y}}{d\hat{t}} &= u_y \\
\frac{du_z}{d\hat{t}} &= pe_z + su_y b \\
\frac{d\hat{z}}{d\hat{t}} &= u_z
\end{aligned} \tag{2.64}$$

The equations listed in 2.64 can be rewritten as:

$$\begin{aligned}
\frac{du_x}{d\hat{t}} &= pe_x \\
\frac{d\hat{x}}{d\hat{t}} &= u_x \\
\frac{du_y}{d\hat{t}} &= pe_y - u_z b \\
\frac{d\hat{y}}{d\hat{t}} &= u_y \\
\frac{du_z}{d\hat{t}} &= pe_z + u_y b \\
\frac{d\hat{z}}{d\hat{t}} &= u_z
\end{aligned} \tag{2.65}$$

2.10 Runge Kutta and model equations

We will now apply the $4^{th}RK$ solver to non-dimensional equations of motion, given the following relations:

$$\hat{\mathbf{r}}^{n+1} = \hat{\mathbf{r}}^n + \frac{\mathbf{k}_{\hat{\mathbf{r}}_1}}{6} + \frac{\mathbf{k}_{\hat{\mathbf{r}}_2}}{3} + \frac{\mathbf{k}_{\hat{\mathbf{r}}_3}}{3} + \frac{\mathbf{k}_{\hat{\mathbf{r}}_4}}{6} \tag{2.66}$$

$$\mathbf{u}^{n+1} = \mathbf{u}^n + \frac{\mathbf{k}_{\mathbf{u}_1}}{6} + \frac{\mathbf{k}_{\mathbf{u}_2}}{3} + \frac{\mathbf{k}_{\mathbf{u}_3}}{3} + \frac{\mathbf{k}_{\mathbf{u}_4}}{6} \tag{2.67}$$

where $d\hat{t} = T/N$ is the temporal step size, T is the integration time and N is the number of time steps.

2.11 The Algorithm

In order to solve the system of equations shown in 2.63, and 2.65, a Fortran 95 code was written. The following steps clarify the idea of the code containing $4^{th}RK$:

1-The initial conditions are set:

These conditions include the positions and velocities of charged particles, the step size and the value of parameter p. Ions are launched through a grain sheath with initial velocities and positions which are chosen to lead to a distance from the grain equivalent to ions' Larmor radius to make sure that ions can reach the grain's position. This can be archived by choosing a distance from the grain within its sheath and selecting appropriate velocities where the Larmor radius is proportional to the particle velocity. In addition, the step size is fixed to give the correct resolution, so the ions can feel the grain's electric field without extra time consumption. For parameter p, two cases are considered: in the first case, $p = 1$ when the electric field is comparable to the magnetic field, and in the second case $p < 1$ when the magnetic field is dominant.

2- Electric fields components are calculated:

Because the simulated grain like wire is a simple model profile, the electric field components in x, y and z directions can therefore be calculated using analytical expressions 2.54, and 2.55 and 2.56, 2.57, and 2.59. Ions field contribution to the sheath field is not included.

3- Applying the $4^{th}RK$ to solve equations of motion at each time step in order to compute the updated positions and velocity.

4- The sheath is considered as collisionless, therefore, collisions are not included at this stage of the work, but are examined in later chapters.

5-The process is continued till charged particles collide with the grain.

6-The next particle is then selected and its trajectory and its velocity evolution followed by repeating steps $2 - 5$.

7-Results including ion positions and velocities are written to a file. Fig. 2.11 shows a flow chart summaries these steps.

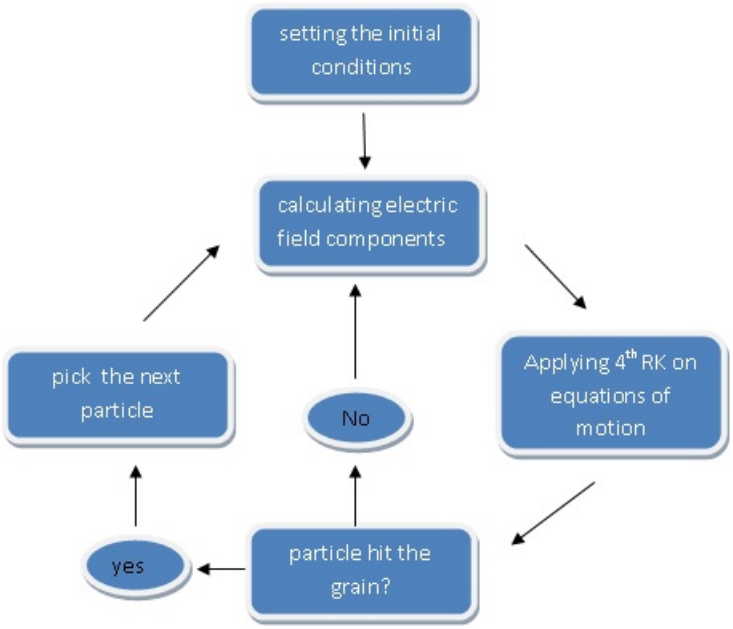

Figure 2.11: Figure showing a flow chart of steps used for calculating particles flow towards the charged grain .

2.12 Results and Discussion

This section calculates and sets out the results of the growth of $1D$ dust in the presence of the magnetic field and the electrostatic field arising from the grain itself. Two cases will be considered; firstly, dust growth in the influence of a magnetic field which is oriented perpendicularly to the long axis of the dust. In the second case, the magnetic field is directed to the grain along the long axis direction. In both situations, the ions' trajectories and energies will be calculated. In addition, the dynamic of dust growth and the effect of the trapped particles will be discussed.

2.12.1 Perpendicular magnetic field

Here, a magnetic field oriented perpendicularly to the long axis of the grain is considered. Figure 2.12 shows a diagram of this configuration. The magnetic field direction is set to a z-direction to be perpendicular to the x-axis where the long axis of grain is directed. The trajectories of the ions toward the grain are calculated and the effect of

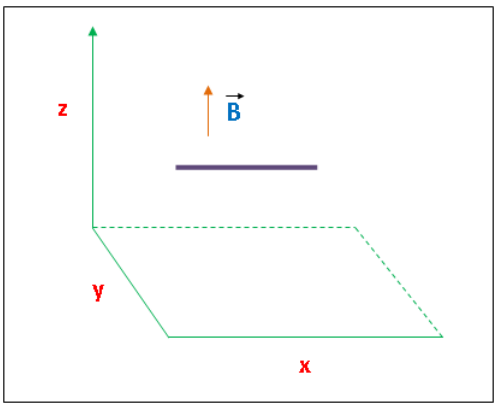

Figure 2.12: Figure showing the direction of the perpendicular magnetic field with respect to the long grain axis.

the magnetic field on dust growth is demonstrated.

Initial conditions

The trajectories of 20 ions distributed along the x-axis (initial $\hat{x} = -L/2$ to $\hat{x} = -3L/2$, and initial $\hat{y} = L/5$) are calculated. To ensure that the ions hit the grain, the perpendicular launch distance is chosen to be smaller than the ions Larmor radius ($\hat{y} < R_L$). The ions Larmor radius is the radius of the circle in the plane perpendicular to the magnetic field direction. The ions are launched with an initial velocity u (u=$u_{x0} + u_{y0}$) where $u_{x0} = 0.2u_0$ and $u_{y0} = 0.01u_0$, and are tracked when they hit the wire surface. The positions $(0, 0)$ and $(L, 0)$ are the ends of the wire. It is important to note that $p = 1$ (p represents the ratio of the electric field to the magnetic field).

Trajectories of Ions

Fig. 2.13 shows the trajectories of the 20 ions distributed along the x-axis. It is clear from the graph that the ions present very different trajectories while under the influence of the constant magnetic field which is in z direction (towards the reader, perpendicular to the plane of the paper) and due to variations in the magnitude and the direction of the electric field in the different regions around the wire. Ions which start close to

the wire(from $\hat{x} = L/5$ to $\hat{x} = 9$) move unimpeded toward the wire until they hit its surface, whereas ions which start their motion from $\hat{x} = -L/2$ to $\hat{x} = L/10$, and $\hat{y} = L/5$, move away from the wire and in a helical motion with large Larmor radius. As the ions start their motion further from the left wire edge, their Larmor radius starts to gradually decrease as they start from further positions from the grain's edge which has a strong electric field. Ions that start their motion from an initial position of $\hat{x} = L$ to $\hat{x} = 3L/2$ move towards the x-axis and present a helical motion with smaller Larmor radius which starts to increase slightly since particles move from further positions from the wire right edge. The motion behavior is similar but in an opposite direction when the particles begin their motion with initial positions $\hat{x} = -L/2$ to $\hat{x} = 3L/2$, and $\hat{y} = -L/5$ as shown in Fig. 2.14.

One important observation from Fig. 2.13 is that the trajectories of these ions deviate from a straight line while they move towards the wire as a result of an $E \times B$ drift which is in -x direction for ions moving toward the top surface of the wire and in x direction for ions moving toward the bottom surface of the wire.

Energy of Ions

Energy was calculated for some of the ions (those which had initial positions $\hat{x} = -L/5$, 0, $L/5$, $4L/10$, $6L/10$,$8L/10$,L,$6L/5$ and $\hat{y} = L/5$) and the results are visualised in Fig. 2.15. The energy curves of the selected ions are identical to those of the nonselected ones, therefore the energy properties of only some of the ions are presented and discussed here. The figure shows that the ions which hit the wire surface gained the highest energy then their energy are set to zero when hitting the wire. In details, ions starting from position $\hat{x} = L/5, 8L/10, \hat{y} = L/5$ gained the highest energy before giving it to the wire while hitting the wire surface(yellow and blue lines), followed by ions starting from $\hat{x} = 4L/10, 6L/10$ and $\hat{y} = L/5$ (pink and light blue lines). Ions that travelled in alignment with the wire ends $\hat{x} = 0, L, \hat{y} = 0$ (green and black lines) still gain high energy as a result of moving near the wire ends which are regions of very high electric field magnitude and their high energies help them to escape from the wire's

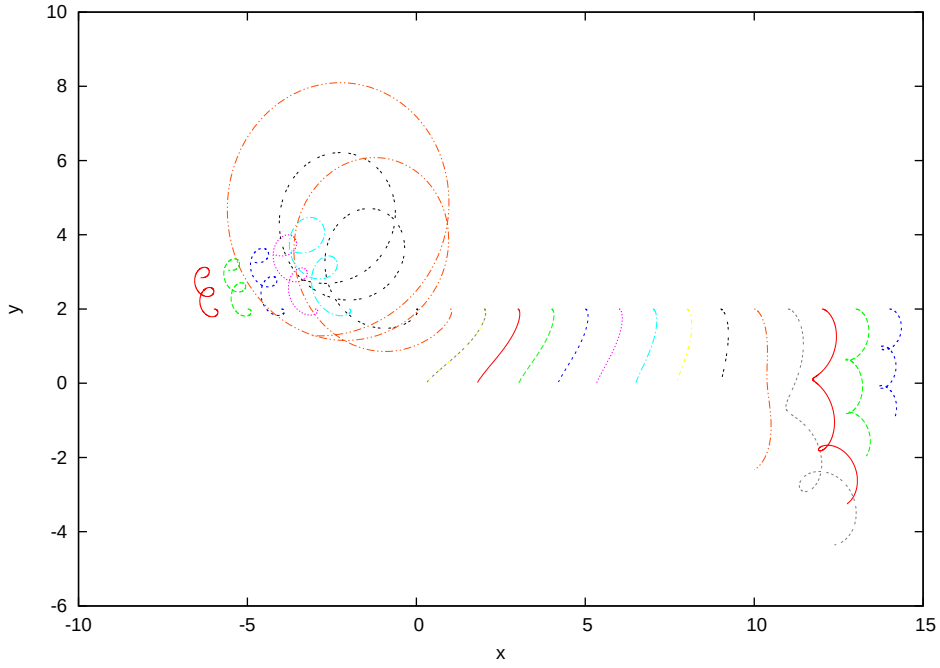

Figure 2.13: Trajectories of 20 ions toward a charged wire. Their initial positions are x=-6 to x=14 ,y=2 and p=1. Note that the wire is located at positions $(0, 0)$ to $(10, 0)$ and the magnetic field is directed towards the reader, perpendicular to the plane of the paper. Ions which start near the wire(from $x = 2$ to $x = 9$) move unimpeded toward the wire until they hit its surface, whereas ions start their motion from $x = -6$ to $x = 1$,$y = 2$, then move away from the wire and show a helical motion with large Larmor radius before they start to decrease gradually as the ions start their motion further from the left wire edge. Ions that start their motion from initial $x = 10$ to $x = 14$ move toward the x-axis and present a helical motion with a smaller Larmor radius which start to increase slightly when particles move from further positions along the wire right edge.

electric field and to avoid hitting the wire. Ions that start from positions further from the wire edges $\hat{x} = -L/5, 6L/5, \hat{y} = l/5$ will gain the lowest amount of energy (red and red dashed lines). In the case of a strong magnetic field (where $p < 1$, as in Fig. 2.23), it is clear that particles which start further away from the wire than a Larmor radius will be impeded from reaching the wire itself; hence in a uniform magnetic field, only those particles with more energy will reach the wire and collide with it. This carries

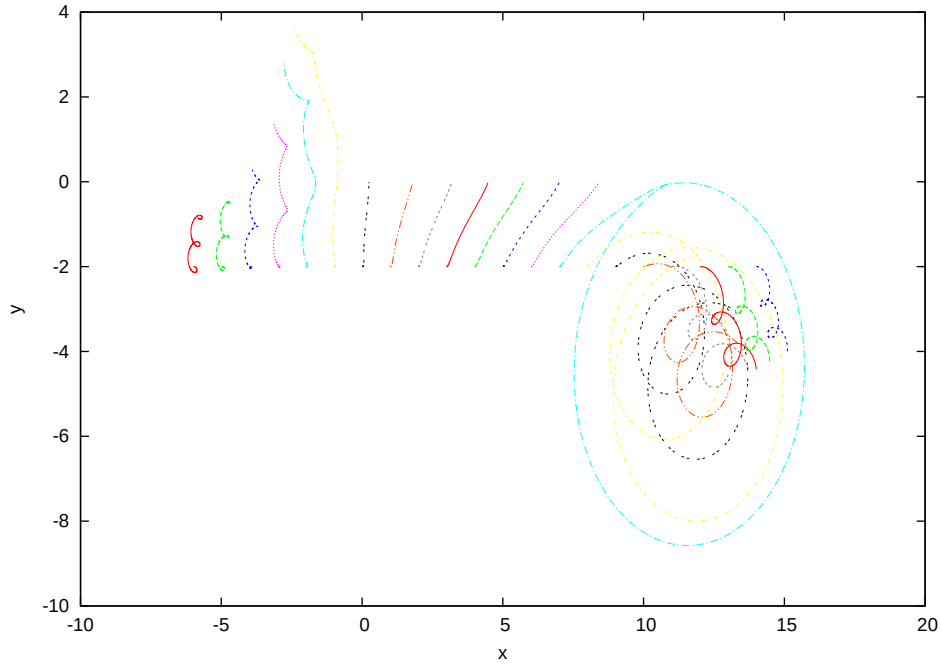

Figure 2.14: Trajectories of 20 ions toward a charged wire. Their initial positions are; x=-6 to x=14 ,y=-2 and p=1. The wire is located at positions $(0, 0)$ to $(10, 0)$ and the magnetic field is directed towards the reader, perpendicular to the plane of the paper. The plot displays similar behaviour but the opposite direction than that seen in Fig. 2.13, because the particles here are launched from below the grain.

the implication that there is a population of trapped particles, orbiting close to the wire but not hitting it, that will effectively shield the electrostatic field from other charged particles, thereby reducing the effective sheath distance.

Trapped particles

In the case a of strong magnetic field, as in Fig. 2.23, it is clear that particles which start further away from the wire than a Larmor radius will be impeded from reaching the wire itself. Hence in a uniform magnetic field, only those particles with more energy will reach the wire and collide with it.

The energetic particles have high velocity components, and as a result their Larmor radius becomes larger as the Larmor radius is proportional to the velocity.

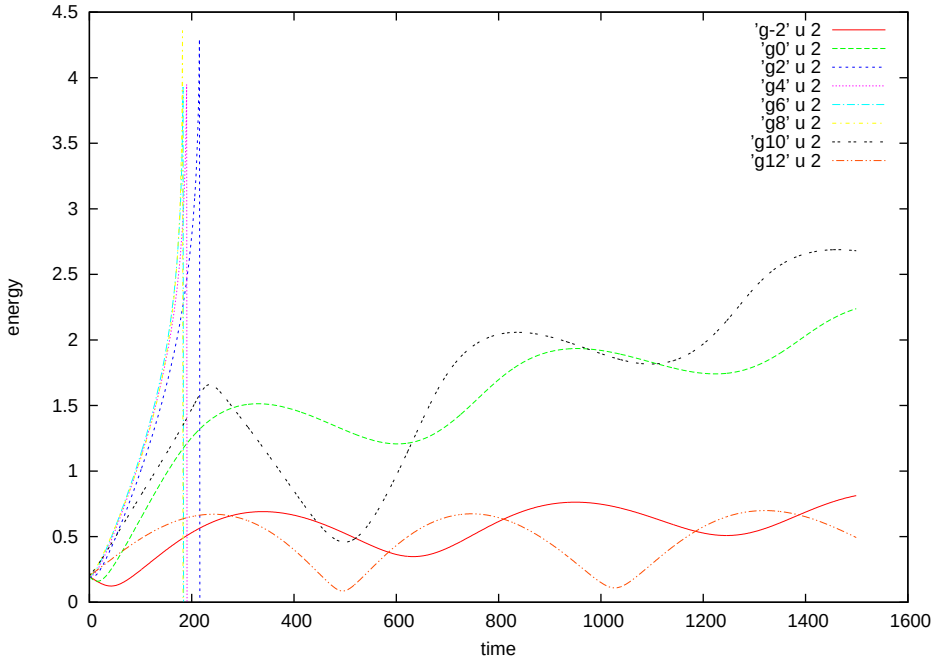

Figure 2.15: Gained energies for eight ions moving towards a charged wire. Their initial positions are; $x = -2, 0, 2, 4, 6, 8, 10, 12$,$y = 2$. Ions that hit the wire surface gain the highest energy then their energies drop to zero when they hit the wire (blue, yellow, pink, and light blue). Ions that travel align with the wire ends ($x = 0, 10, y = 0$)(green and black lines) still gain high energy (but lower than those which were hit) as a result of moving near the wire ends.

$$r_c = \frac{v_\perp}{w_c} \tag{2.68}$$

This means that in this case the energetic particles can reach a larger distance from their initial positions than other particles and may reach the grain's position. Other particles, which is orbiting close to the wire but not hitting it, will effectively shield the electrostatic field from other charged particles, reducing the effective sheath distance.

There are two classes of particles that do not impact the grain, but have persistent nearby trajectories which will shield the grain's electrostatic field from other charged particles: (i) distant particles, which execute Larmor orbits that prevent impact. Fig. 2.17 shows that the final energy gained by impacting ions increases with distance from the grain up to a certain point ($y = 3$) where the ion is forced into a Larmor orbit before

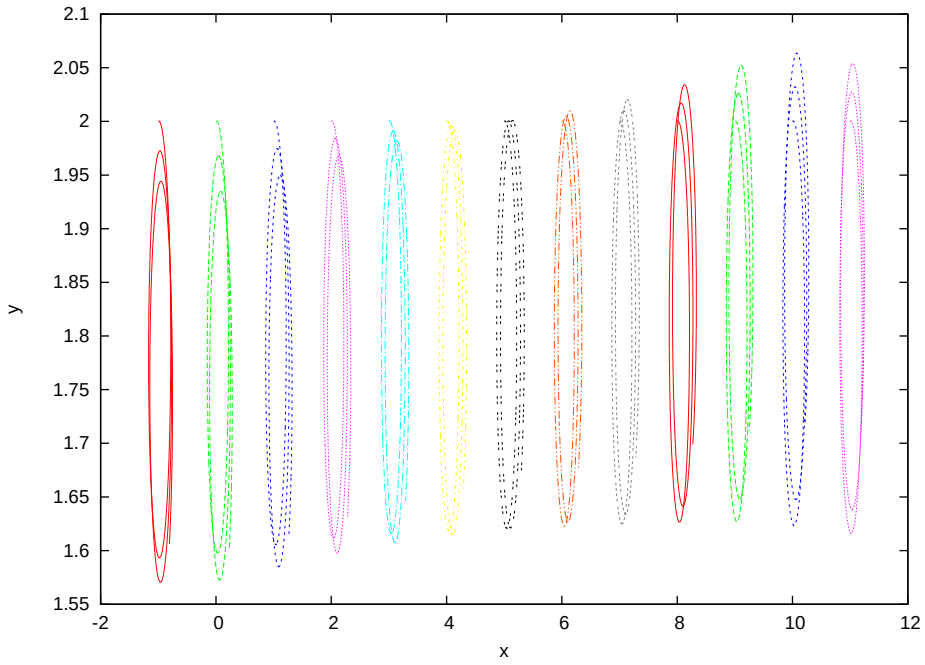

Figure 2.16: Ions in circular motion in the influence of a strong magnetic field. The ion's initial positions are; $x = -1$ to $x = 11, y = 2$. Note that the magnetic field is directed towards the reader, perpendicular to the plane of the paper and $p = 0.001$. Particles execute Larmor orbits that do not intersect the wire position, and so they are unable to collide with the wire.

reaching the grain. (ii) energetic particles, which orbit the grain,as shown in Fig. 2.18.

This effect of electrostatic field reduction is a consequence of repletion between coming ions and trapped ones. That results in a reduction in the distances ions can reach.

Ions Loading

Histograms are used to show the location and number of particles arriving at the grain site. For the electric field dominating the magnetic field, particle distribution tends to be more concentrated at the grain surface. For a dominant magnetic field, a skew in particle distribution is noticeable as shown in Fig. 2.19.

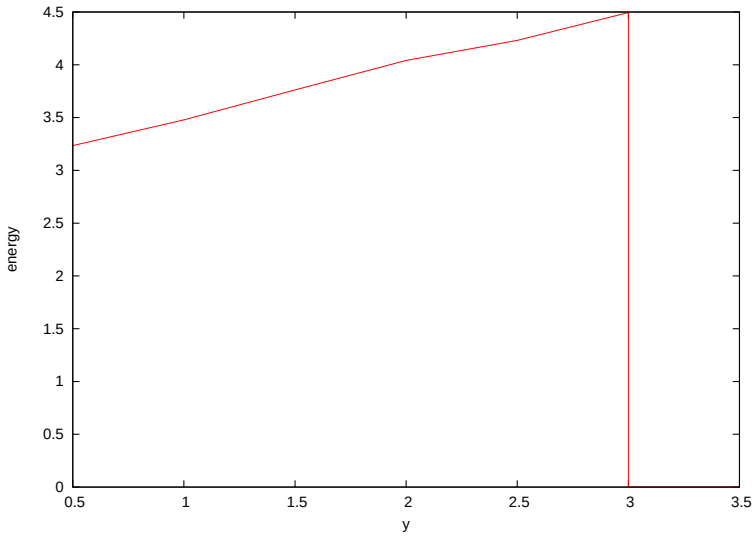

Figure 2.17: Plot of ion energy on impact as a function of their starting distance from the grain. The final energy gained by impacting ions increases with the distance from the grain up to the point (y=3) where the ion is forced into a Larmor orbit before reaching the grain. The increase of impact energy with initial distance is entirely due to the ion falling a greater distance under the electric field.

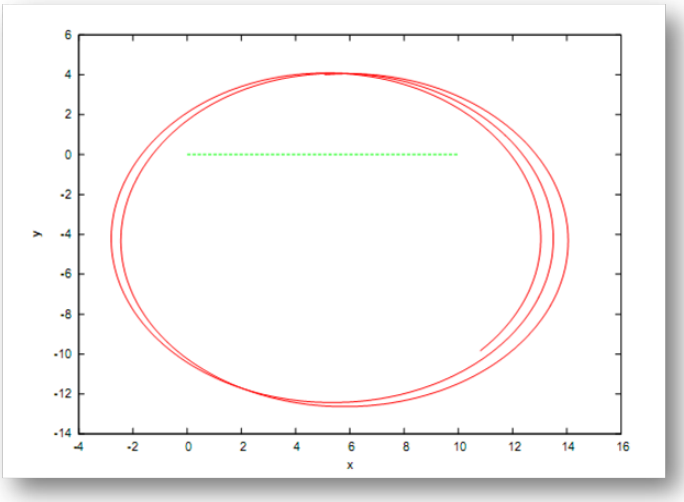

Figure 2.18: Examples of orbiting particles, initial velocities: $ux = 8$, $uy = 1$, initial starting position:$(5, 4)$.

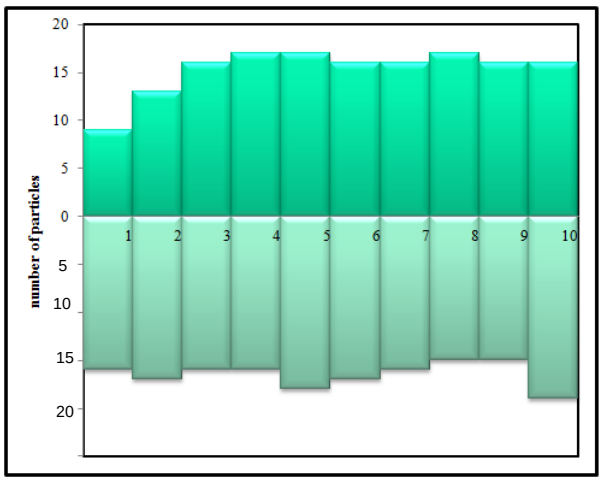

Figure 2.19: Histogram showing the location and number of particles arriving at the grain site. Note the skew in particle distribution. The magnetic field directed perpendicular to the grain long axis.

2.12.2 Parallel magnetic field

In this case the magnetic field is oriented to x-direction which is the same direction of the long axis of the grain. Diagram 2.20 shows this situation. This requires the simulation to be in three dimensions to allow the magnetic field's alignment with the grain axes. Again, positive ions' trajectories toward the grain and ion accretion on the grain surface will be calculated .

Initial conditions

The trajectories of 20 ions distributed along the x-axis (initial $x = -L/2$ to $x = -3L/2$, initial $y = L/5$ and $z = L/20$) were studied. The ions were launched with an initial velocity (u_{x0}, u_{y0}, u_{z0}) and tracked until they hit the wire surface. The wire is located at position $(0, 0, 0)$ to $(L, 0, 0)$. It is important to mention that $p = 1$ (p represents the ratio of the electric field to the magnetic field).

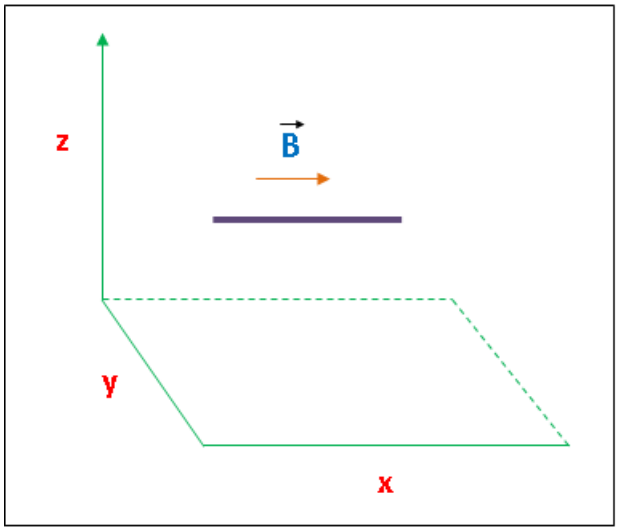

Figure 2.20: Figure showing the direction of the parallel magnetic field with respect to the long grain axis.

Trajectories of Ions

Fig.2.21 shows the trajectories of the 21 ions distributed evenly along the x-axis from perpendicular non dimensional distance=1.1 from the grain. The initial positions are $\hat{x} = -L/2$ to $3L/2, \hat{y} = L/10$, and $\hat{z} = L/20$. The ions are launched with perpendicular velocity= 1.2. In these conditions, the particles are found to tend to hit the grain. It is clear from Fig.2.21 that the ions follow very different trajectories under the combined influence of a constant magnetic field which is in x direction (parallel to the grain) and a non-uniform electrostatic field arising from the charged grain. In broad terms, there are two sets of trajectory solutions. Ions which start from positions near the grain, but not at the corners (x in the range $[0, L]$) move in curved paths towards the grain until they hit its surface, whereas those ions which start their motion near the corner(x in range $[L, 3L/2]$ and$[-L/2, 0]$) are driven towards the other grain's corner(+ or $-x$ for ions starting from the left and right grain's corner respectively) but are gradually driven away from the grain (to $+y$,$-z$ direction) by the combination of local field configurations, and follow a helical motion with an increasing Larmor radius (due to the acceleration produced by the corner electric field). These corner particles cause

some population around the grain, as shown in Fig.2.22.

As before, in this case the magnetic field is directed in x direction, then the x-component is an acceleration along B.

The velocity components of equations array 2.64 are:

$$\frac{du_x}{d\hat{t}} = e_x \tag{2.69}$$
$$\frac{du_y}{d\hat{t}} = e_y - u_z b \tag{2.70}$$
$$\frac{du_z}{d\hat{t}} = e_z + u_y b \tag{2.71}$$

Parameter p is set to $p = 1$ one. The solution of the first equation is:

$$u_x(t) = e_x t + u_{x0} \tag{2.72}$$

where u_{x0} is the initial velocity component in x direction, and the solution represents an acceleration along B. This is a simple calculation and it is not the solution for the actual problem, as the electric field in our problem is non constant but varies with position. Rearranging these equations and taking the time derivative of the second and third equations in 2.69 (where a dot above a quantity represents the derivative d/dt):

$$\ddot{u_y} = -b(e_z + u_y b) = -b^2(u_y + \frac{e_z}{b}) \tag{2.73}$$
$$\ddot{u_z} = b(e_y - u_z b) = -b^2(u_z - \frac{e_y}{b}) \tag{2.74}$$

The electron cyclotron frequency b and drift velocity u_D is equal to $u_D = \frac{e}{b}$. Solutions of these equations are expressed as:

$$u_y(\hat{t}) = A\cos(b\hat{t}) + B\sin(b\hat{t}) - u_D \tag{2.75}$$

$$u_z(\hat{t}) = C\cos(b\hat{t}) + D\sin(b\hat{t}) + u_D \tag{2.76}$$

To find coefficients A, B, C and D, the initial conditions are applied in previous equations.

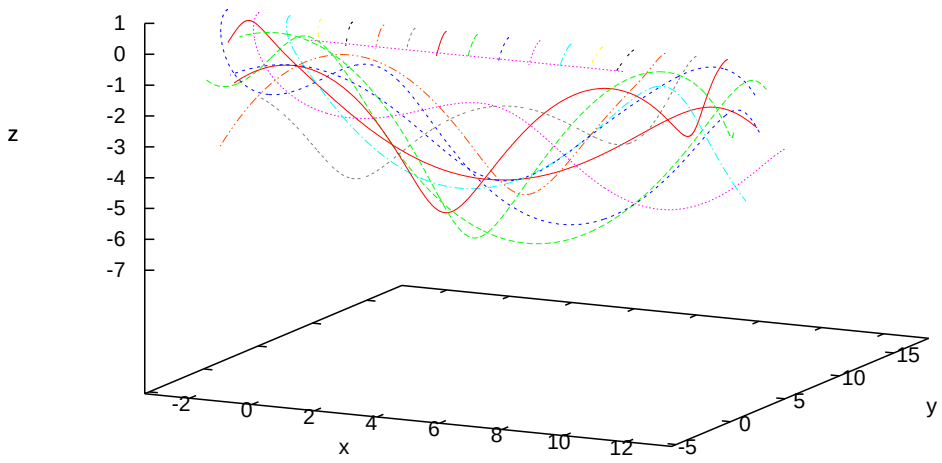

Figure 2.21: Trajectories of 21 ions moving towards the charged grain from initial positions: $x = -L/2$ to $L + 5$, $y = L/10$, and $z = L/20$. The magnetic field is parallel to the grain. Ions starting from positions closest to the grain corners undergo Larmor orbits which ensure that they don't intersect the grain surface; all other ions impact the grain.

So, the ion is accelerated by the electric field, and orbits the magnetic field lines in a circular motion. In contrast, the guiding centre drifts in a direction perpendicular to both the electric and magnetic fields. Therefore, the orbit of the particle in space is that of a slanted helix with a changing pitch.

Ions' energies

Energies were calculated for selected ions (having initial positions of $\hat{x} = -L/2, -3L/10, -L/10, 0, L/5, L/2, 6L/5, 7L/5$) and are presented in Fig.2.23. The other of ions not presented here (have initial $\hat{x} = -2L/5, -L/5, L/10, 3L/10, 7L/5, 11L/10, 13L/10$) have identical energies to the selected ones. Fig.2.23 shows some colliding ions en-

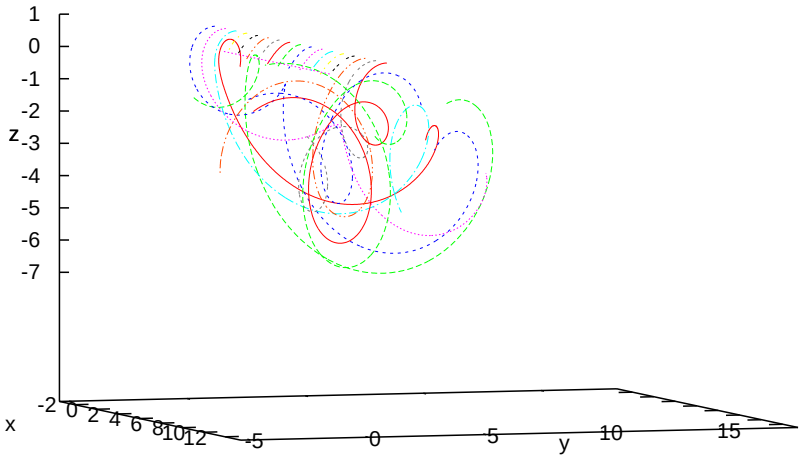

Figure 2.22: As Fig.2.21 but showing the corner particles' population around the grain.

ergies. Those ions that impact the grain(initial $\hat{x} = 0,\ L/5,\ L/2$) have their energies zeroed. Those with starting positions near the grain's centre, gain the highest energies before the collision.

Trapped particles

The Debye sheath of the negatively charged grain is considered to be an attractive well for positive ions. These ions can be trapped in bounded orbits to the grain until they freed if they undergo a collision. Including trapped ions in our calculations is important because these ions can shield the charged particle from external electric fields.

In this case there are two classes of grain shielding:

1. Particles which orbit symmetrically about the grain, enclosing it in a smear of charge; (see Fig.2.24(a)). These particles have a perpendicular velocity = 1.2, an initial position $(5, 4, 2.1)$, and a perpendicular distance=4.2. Such particles

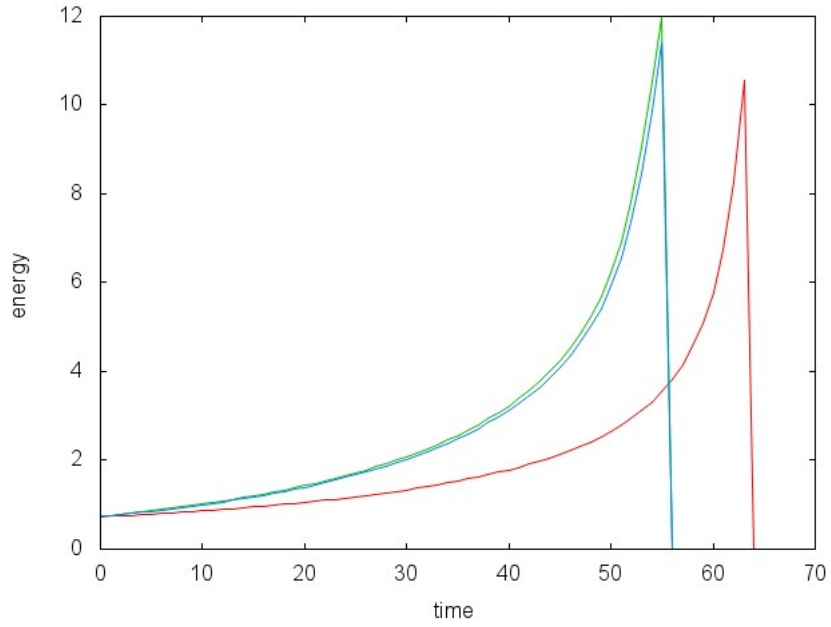

Figure 2.23: Energies acquired by ions moving towards the charged grain from initial positions $x = 0, 2, 5$ (red,blue,and green lines respectively). Ions impacting the grain have their energies zeroed; those impacting closest to the grain centre gain the highest energy.

can reduce the effective charge on the grain for all arriving particles.

2. Particles which perform strongly localised orbits which do not necessarily entirely enclose the grain (Fig.2.24(b)). They have an initial position $(5, 1, 5)$, a perpendicular distance=5 ,and a perpendicular velocity=6.8. These particles produce a localised perturbation to the field around the grain, and may deflect particles arriving from particular directions.

Case (1) also has a special sub-case: particles that orbit close to the grain corners for a short time before moving away; these orbits still have an element of symmetry, but they do not persist for as long as the other symmetric orbiting particles which have not started near the strong fields at the grain corners.

An effect of trapped ions is the reduction of the surface potential of a dust particle, or the presence of a large number of trapped ions in the Debye shielding cloud which may affect the interaction of dust particles with electromagnetic forces or may

influence dust interaction with each other. In our case, this reduction of the grain's potential can be taken into consideration by reducing the amount of overall charge on the grain. Orbit-motion-limit (OML) theory [Laframboise (1966),Lampe (2001a)] for spherical probes is often used to calculate the charge and to study the shielding of dust grains in plasma. OML neglects the effect of bounded ions and ions-neutral collisions [**?**], although collisions of ions can increase the ion current collected and change the potential profile of the shielding sheath of the grain. Sternovsky et al. [Sternovsky et al. (2004)] noted that the minimum surface potential value is at positions close to where the maximum numbers of trapped ions has occured.

Ions Loading

About 10^4 particles were launched toward the grain to study the colliding particles distribution at the grain surface. A histogram shows the location and number of particles arriving at the grain site, (see Fig.2.25). Note the gradual increase, from the grain centre to the ends, in terms of the number of impacting particles. Therefore, the dust grain that aligned parallel to the magnetic field is subject to elongation growth.

2.13 Overview of the role of magnetic fields on dust growth

Adding magnetic fields to dusty plasmas allows some interesting effects. The presence of magnetic fields may cause unbalanced charge distributions on the surfaces of dust grains. However, further simulation research in 3D is required to investigate this possible effect and this will be done in chapter 4. Furthermore, magnetic fields cause more restricted motion for charged particles moving perpendicularly to magnetic fields direction in comparison to particles moving parallel to a magnetic field's direction. The addition of a magnetic field can encourage elongated dust growth. A magnetic field parallel to a long grain's axis causes restrictions on ions' motion toward the grains

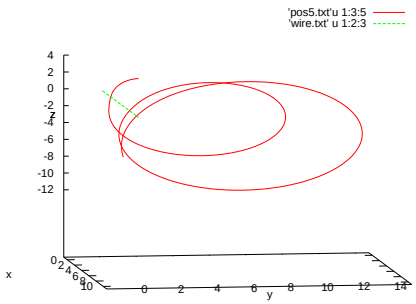

(a)

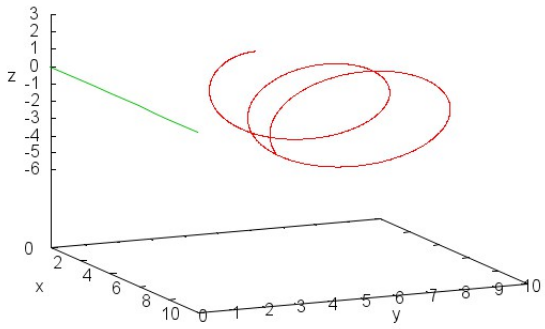

(b)

Figure 2.24: (a) Examples of Particles that start further away from the grain and do not intersect the grain position and hence shield the grain's electrostatic field. Their initial positions are $(5, 4, 2.1)$.(b) Examples of orbiting particle,its initial start position$(5, 1, 0.55)$
and its perpendicular velosity=6.8

surface. However, the ions' movement is impeded in direction perpendicular to the magnetic field, meaning more loading on the grain's ends. Applying a perpendicular magnetic field (to the long axes of dust grain direction) reveals a skewed dust growth, and further tests of this behaviour are required in a more realistic configuration.

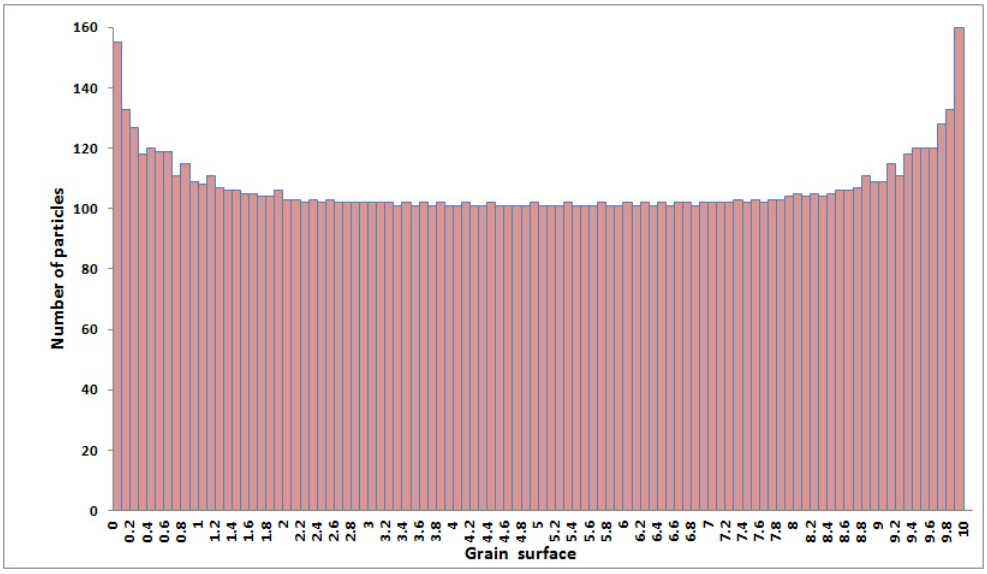

Figure 2.25: Histogram showing the location and number of particles arriving at the grain site. Note the congestion of colliding particles at grain ends. The magnetic field directed along the grain constrains the particles' motion ina perpendicular direction to the magnetic field, whereas particles move freely in the direction of the magnetic field (towards the grain's ends)in addition to the higher electrostatic field at these locations.

2.14 Astrophysical and laboratory context

Understanding the process involving dust charging and growth leads to an improved understanding of these processes in several different astrophysical and laboratory plasma environments. Table 2.2 shows the typical parameters of various dust-plasma environments. There n_e, n_n and n_d are the number densities of electrons, neutrals and dust, respectively; a and Z_d are the grain radius and charge state. T is the electron temperature in eV; while d, λ_D and Γ_d are the average inter-grain distance, the Debye shielding distance and the grain Coulomb coupling parameter, respectively. It is obvious that these parameters have quite different ranges in cosmic and laboratory regimes. However, the associated physical processes are still similar. Unlike terrestrial plasma, most cosmic environments are low temperature plasma, meaning that the ionization fraction is also low and more species are neutrals. The number of ions simulated here may lie

on an astrophysical range, which are much less than terrestrial range. However, it is still relevant as a general model which can easily be modified to the desired parameters. The chosen acquired electrostatic field by dust $\phi_0 = -10\ V$ is consistent with astrophysical dust measurements. The selected value of parameter $p = 1$ (describes the relative sizes of electrostatic field and applied magnetic fields). However, astrophysical and laboratory magnetic fields differ by factors of tens in orders of magnitudes and thereby requiring higher and lower values for parameter p to cover the low- and highly- magnetic environments. The next chapter will cover these extra assumptions, since this chapter has presented an initial and simple model of elongated dust growth.

Environment	$n_e(cm^{-3})$	$T(eV)$	$n_d(cm^{-3})$	$a(\mu m)$	$n_n(cm^{-3})$	$\lvert Z_d \rvert$	d/λ_D
Interstellar molecular clouds	10^{-3}	0.001	10^{-7}	0.2	10^4	~ 1	0.3
Supernovae shells	10^3	0.2	10	0.01	–	20	$\sim 5 \times 10^{-2}$
Flames	$> 10^{11}$	0.2	$< 10^{11}$	0.01	5×10^{18}	2	0.5
Lab-plasma (Dust-Ball)	10^8	2 – 4	10^3	5	5×10^{14}	10^3	0.4 – 0.6
Process plasma (Chip manufacture)	3×10^9	2	$10^3 - 10^8$	≤ 1	10^{15}	$< 3 \times 10^3$	0.1 – 3
Coulomb dust crystal	10^9	2	$10^4 - 10^5$	5	10^{16}	10^4	0.3 – 1

Table 2.2: Typical properties of dust in different plasma environments [Mendis (2002)].

2.15 Conclusion

The simulations presented in this chapter show the influence of magnetic fields oriented perpendicularly and parallel to the long-axis of the grain, respectively, on the ion loading on a charged grain surface. Ions approaching the corners of a finite, rod-shaped grain missed grain collisions, while ions that started close to the grain's central regions did experience collisions. Moreover, there is a population of trapped particles, orbiting close to the wire but not hitting it, that effectively shields the electrostatic field from other charged particles, reducing the effective sheath distance. The final energy gained by the impacting ions increases according to the separation distance from the grain, as the ions fall through an increasing electric potential. The grain shielding

created by trapping ions requires more investigation and more calculations are provided in chapter 4. Finally, we have observed that the magnetic field influences the spatial deposition pattern of the ions, leading to increasing ions fluxes at the grain's ends. However, a more reliable treatment of dust growth should be carried, dealing with models in three dimensions and calculating an accurate electric potential on the simulation domain. Chapter 3 demonstrates the method of finite difference to establish particle motion through a grain sheath, setting an accurate ellipsoidal dust surface. Chapter 4 introduces the results of dust growth depending on chapter 3's technics.

3

The finite difference method and the Lagrange multiplier

3.1 Introduction

The ideal simulation of dust grains growth needs to be done in three dimensions and requires the dust grains to have a three dimensional shape. In a plasma, charged particles flow toward grains within a dust sheath requiring an effective way to calculate electric potential field. A finite difference solver in three dimensions is discussed and applied here to calculate the dust potential and the electric field's components. As the potential calculations need to set potential dust surface accurately, a good technique based on a Lagrange multiplier is introduced and used to interpolate the dust shape.

3.1.1 The electric potential of ellipsoidal grains

Finding the electric potential of ellipsoidal grains in two and three dimensions requires the solving of a Laplace equation in two and three dimensions. However, in this chapter only a three dimensions approach will be discussed as the two dimensional process follows the same technique. The Poisson equation in three dimensions is given by:

$$\left(\frac{\partial^2}{\partial x^2}+\frac{\partial^2}{\partial y^2}+\frac{\partial^2}{\partial z^2}\right)\phi = 0 \tag{3.1}$$

with boundary conditions:

$$\phi(x,y,z) = \begin{cases} \phi_s, & b^2c^2x^2 + a^2c^2y^2 + a^2b^2z^2 - (abc)^2 \leq 0 \\ 0, & x^2+y^2+z^2 \to \infty \end{cases}$$

where a,b, and c are the grain axes at x,y, and z coordinates respectively. These conditions imply that the potential on the grain surface is ϕ_s and this potential reduces to zero at the sheath edge. Laplace equation can be solved analytically. However, to avoid complexities and to arrive at an accurate solution, numerical methods are preferable. These numerical methods fall in two categories; direct and iterative. It is well known that direct methods yield an exact solution of the differential equation by solving a system of linear equations via a known number of prescribed operations. Alternatively, iterative numerical solutions can be used to solve Laplace equation. These methods depend on the estimation of an initial solution, allowing it to slowly relax in to the exact solution. Several attempts have to be made to obtain the true solution. So, one can use a relaxation method to allow the numerical solution converge to the exact solution. That can be done by solving the diffusion equation:

$$\frac{\partial\phi}{\partial t} - D\left(\frac{\partial^2}{\partial x^2}+\frac{\partial^2}{\partial y^2}+\frac{\partial^2}{\partial z^2}\right)\phi = 0 \tag{3.2}$$

in which D is the diffusion constant.

In order to simplify the problem and make it applicable to computational solving, non-dimensional relations were used as follows:

$$\Phi = \frac{\phi}{\phi_0} \tag{3.3}$$

$$\tau = \frac{t}{t_0} \tag{3.4}$$

$$r = (x,y,z) \tag{3.5}$$

$$\hat{r} = (\hat{x}, \hat{y}, \hat{z}) \tag{3.6}$$

That gives

$$\frac{\partial \Phi}{\partial \tau} - \sigma(\frac{\partial^2}{\partial \hat{x}^2} + \frac{\partial^2}{\partial \hat{y}^2} + \frac{\partial^2}{\partial z^2})\Phi = 0 \tag{3.7}$$

where $\sigma = Dt_0/L$ is a dimensionless parameter, t_0 is a characteristic time of diffusion and L is the grain sheath's characteristic length. The selection of D and t_0 values has no prior requirements, as their values only have numerical significance. A finite difference method is used to solve equation 3.7 as it is simplest to implement. Furthermore, it is easy to converge, and stable.

3.2 The finite difference method

The basic concepts of the finite difference method [Lapidus and Pinder (2011),Press (1992)] can be clarified as follows:

Replace the domain of the solution of PDE (partial differential equation) with a finite number of mesh points. Then, the derivative of the equation is replaced at each mesh point by a finite difference approximation .

First the $\hat{x}$,$\hat{y}$,$\hat{z}$, and τ domain are divided into a set of nodes such that:

$$\Phi(\hat{x}) = \Phi(mh) \tag{3.8}$$

$$\Phi(\hat{y}) = \Phi(lh) \tag{3.9}$$

$$\Phi(\hat{z}) = \Phi(nh) \tag{3.10}$$

$$\Phi(\tau) = \Phi(ok) \tag{3.11}$$

$$\Phi(\hat{x}, \hat{y}, \hat{z}, \tau) = \Phi(mh, lh, nh, ok) = \Phi^{o}_{m,l,n} \tag{3.12}$$

in which:

$$m \in [0, mmax] \tag{3.13}$$

$$l \in [0, lmax] \tag{3.14}$$

$$n \in [0, nmax] \tag{3.15}$$

$$o \in [0, omax] \tag{3.16}$$

The grid spacing in $\hat{x}$,$\hat{y}$,$\hat{z}$ directions is h and in τ direction is k. m, l, and n refer to the location of function Φ in the $\hat{x}$,$\hat{y}$, and $\hat{z}$ coordinates, respectively. The Taylor expression of Φ at point $(\hat{x}, \hat{y}, \hat{z})$ yields:

$$\Phi^{o+1}_{m,l,n} = [\Phi^{o}_{m,l,n} + k\delta\tau\Phi^{o}_{m,l,n}] \tag{3.17}$$

where higher order terms were neglected. Using $\delta\tau\Phi^{o}_{m,l,n} = \delta(\partial^2_{\hat{x}} + \partial^2_{\hat{y}} + \partial^2_{\hat{z}})\Phi^{o}_{m,l,n}$; gives:

$$\Phi^{o+1}_{m,l,n} = [\Phi^{o}_{m,l,n} + k\delta(\partial^2_{\hat{x}} + \partial^2_{\hat{y}} + \partial^2_{\hat{z}})\Phi^{o}_{m,l,n}] \tag{3.18}$$

By replacing each second derivatives with finite difference approximation

$$U_{s,t,l} = \frac{1}{6}[(U_{s+1,t,l} + U_{s-1,t,l}) + (U_{s,t+1,l} + U_{s,t-1,l}) + (U_{s,t,l+1} + U_{s,t,l-1})] \tag{3.19}$$

yields;

$$\Phi^{o+1}_{m,l,n} = (1 - 6w\sigma)\Phi^{o}_{m,l,n} + w\sigma(\Phi^{o}_{m+1,l,n} + \Phi^{o}_{m-1,l,n} + \Phi^{o}_{m,l+1,n} + \Phi^{o}_{m,l-1,n} + \Phi^{o}_{m,l,n+1} + \Phi^{o}_{m,l,n-1}) \tag{3.20}$$

where $w = k/h^2$ is the mesh ratio.

3.2.1 Stability

Finite difference approximation 3.20 is stable and converges if [Lapidus and Pinder (2011)]:

$$0 < w\sigma \leq \frac{1}{6} \tag{3.21}$$

The boundary conditions are:

$$\phi(x,y,z) = \begin{cases} -1, & b^2c^2(m-m_0)^2 + a^2c^2(l-l_0)^2 + a^2b^2(n-n_0)^2 - (abc)^2 \leq 0 \\ 0, & (m-m_0)^2 + (l-l_0)^2 + (n-n_0)^2 - r_s^2 \geq 0 \end{cases}$$

where $m_0 = mmax/2,\ l_0 = lmax/2,\ n_0 = nmax/2$ r_s is an integer denoting the radius of the plasma sheath and a, b, and c are integers that denote the semi-major and minor axes of the ellipsoid on the discrete cartesian grid $(mh; lh; nh)$. The parameter $omax$ is chosen to be suitably large to permit a numerical solution in order to converge to the right solution. The finite difference method is convergent to the true solution if the overall error approaches zero as k and h approach zero.

3.2.2 Boundary and initial conditions

An accurate interpolation technique was used to incorporate the grain shapes and to set boundary conditions of the grain surface following steps used by Stark [Stark (2008)]:

- Potential distribution

  The technique used here depends on the fact that the potential in a vacuum reduces by $1/d$ from the charge source , where d is the perpendicular distance from the source. With this in mind, the potential on a point $(\hat{x}, \hat{y}, \hat{z})$ outside the grain can be written as:

$$\Phi(\hat{x}, \hat{y}, \hat{z}) = \frac{\gamma\Phi_0}{\gamma + d(\hat{x}, \hat{y}, \hat{z})} \tag{3.22}$$

where γ is a normalization factor and $d(\hat{x}, \hat{y}, \hat{z})$ is the perpendicular distance from the nearest mesh point outside the ellipsoid to a point (x_s, y_s, z_s) on the grain surface and Φ_0 is the potential on the grain surface.

- Finding the nearest grid points outside the ellipsoid;

  The points of intersection between the ellipsoid and the family of lines $\hat{y} = lh$ for $l \in (l_0 - b, l_0 + b)$ and family of lines $\hat{z} = nh$ for $n \in (n_0 - c, n_0 + c)$ are determined . This will give familly of points outside the ellipsoid (x_s, y_s, z_s). For each of these mesh points (lh) and (nh), determine which m satisfy the relation $m < x_s < m - 1$. This gives the nearest mesh points $(x_p, y_p, z_p) \equiv (mh, lh, nh)$ in $\hat{x}$ direction. To make sure mesh points are accurate, determine family of lines $\hat{x} = mh$ for $m \in (m_0 - a, m_0 + a)$ and family of lines $\hat{z} = nh$ for $n \in (n_0 - c, n_0 + c)$, yielding (x_s, y_s, z_s). For each of these mesh points (mh) and (nh), determine which l satisfy the relation $l < y_s < l - 1$ this gives the nearest mesh points in $\hat{y}$ direction, then do same steps for family of lines $\hat{x} = mh$ for $m \in (m_0 - a, m_0 + a)$ and family of lines $\hat{y} = lh$ for $l \in (l_0 - b, l_0 + b)$, giving (x_s, y_s, z_s). For each of these mesh points (mh) and (lh), determine which n satisfy the relation $n < z_s < n - 1$ this gives the nearest mesh points $(x_p, y_p, z_p) \equiv (mh, lh, nh)$ in $\hat{z}$ direction.

- Finding the perpendicular distance $d(\hat{x}, \hat{y}, \hat{z})$:

  The perpendicular distance $d(\hat{x}, \hat{y}, \hat{z})$ from a point on the ellipsoid surface to the nearest grid point (x_p, y_p, z_p) can be calculated using the Lagrange multiplier method [Press (1992)] which is used to maximize and minimize a general function, $f(x, y, z)$, subject to the constraint $g(x, y, z)$.

$$\nabla L(\hat{x}, \hat{y}, \hat{z}, \lambda) = \nabla[f(\hat{x}, \hat{y}, \hat{z}) + \lambda g(\hat{x}, \hat{y}, \hat{z})] \tag{3.23}$$

  where,

$$f(\hat{x}, \hat{y}, \hat{z}) = [(x_p - \hat{x})^2 + (y_p - \hat{y})^2 + (z_p - \hat{z})^2]^{\frac{1}{2}} \tag{3.24}$$

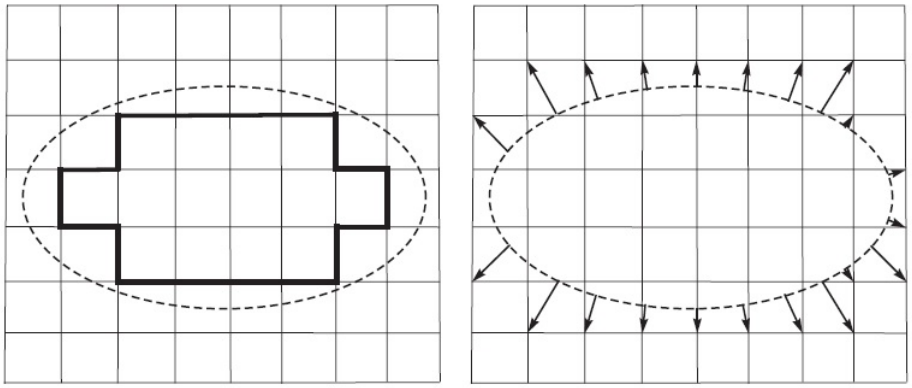

Figure 3.1: Plot showing the execution of the boundary conditions. The left diagram illustrates the step-wise approximation while the plot on the right illustrates the potential interpolator implementation where the electric potential is specified at the nearest grid points outside the ellipse boundary. The arrows show the immediate neighbour grid points where the potential is set by the interpolator method. [Stark (2008)].

$$g(\hat{x},\hat{y},\hat{z}) = \frac{\hat{x}^2}{a^2} + \frac{\hat{y}^2}{b^2} + \frac{\hat{z}^2}{c^2} - 1 \tag{3.25}$$

by considering the ellipsoid centered at $(0,0,0)$ then:

$$\hat{x} \rightarrow \hat{x} - \hat{x}_0 \tag{3.26}$$

$$\hat{y} \rightarrow \hat{y} - \hat{y}_0 \tag{3.27}$$

$$\hat{z} \rightarrow \hat{z} - \hat{z}_0 \tag{3.28}$$

$$x_p \rightarrow x_p - \hat{x}_0 \tag{3.29}$$

$$y_p \rightarrow y_p - \hat{y}_0 \tag{3.30}$$

$$z_p \rightarrow z_p - \hat{z}_0 \tag{3.31}$$

Applying these relations in Eq. 3.23 leads to the following equations:

$$\frac{\partial L}{\partial \hat{x}} = -[(x_p - \hat{x})^2 + (y_p - \hat{y})^2 + (z_p - \hat{z})^2]^{\frac{-1}{2}}((x_p - \hat{x}) + \frac{2\lambda}{a^2}\hat{x} = 0 \tag{3.32}$$

$$\frac{\partial L}{\partial \hat{y}} = -[(x_p - \hat{x})^2 + (y_p - \hat{y})^2 + (z_p - \hat{z})^2]^{\frac{-1}{2}}((y_p - \hat{y}) + \frac{2\lambda}{b^2}\hat{y} = 0 \tag{3.33}$$

$$\frac{\partial L}{\partial \hat{z}} = -[(x_p - \hat{x})^2 + (y_p - \hat{y})^2 + (z_p - \hat{z})^2]^{\frac{-1}{2}}((z_p - \hat{z}) + \frac{2\lambda}{c^2}\hat{z} = 0 \tag{3.34}$$

$$\frac{\partial L}{\partial \lambda} = \frac{\hat{x}^2}{a^2} + \frac{\hat{y}^2}{b^2} + \frac{\hat{z}^2}{c^2} - 1 \tag{3.35}$$

expressing Eqs. 3.32 , 3.33, and 3.34 in terms of λ gives:

$$\lambda = \frac{a^2}{2\hat{x}}[(x_p - \hat{x})^2 + (y_p - \hat{y})^2 + (z_p - \hat{z})^2]^{\frac{-1}{2}}(x_p - \hat{x}) \tag{3.36}$$

$$\lambda = \frac{b^2}{2\hat{y}}[(x_p - \hat{x})^2 + (y_p - \hat{y})^2 + (z_p - \hat{z})^2]^{\frac{-1}{2}}(y_p - \hat{y}) \tag{3.37}$$

$$\lambda = \frac{c^2}{2\hat{z}}[(x_p - \hat{x})^2 + (y_p - \hat{y})^2 + (z_p - \hat{z})^2]^{\frac{-1}{2}}(z_p - \hat{z}) \tag{3.38}$$

combining Eqs. 3.36 , and 3.37 to eliminate λ gives:

$$\frac{a^2(x_p - \hat{x})}{\hat{x}} = \frac{b^2(y_p - \hat{y})}{\hat{y}} \tag{3.39}$$

combining Eqs. 3.36 , and 3.38 gives:

$$\frac{a^2(x_p - \hat{x})}{\hat{x}} = \frac{c^2(z_p - \hat{z})}{\hat{z}} \tag{3.40}$$

and combining Eqs. 3.37 , and 3.38 to eliminate λ gives:

$$\frac{b^2(y_p - \hat{y})}{\hat{y}} = \frac{c^2(z_p - \hat{z})}{\hat{z}} \tag{3.41}$$

Rearranging these equations and subsisting them into equation 3.35 yields a 6^{th} order polynomial in x:

$$\sum_{i=0}^{6} A_i x^i \tag{3.42}$$

in which:

$$A_0 = -a^{10} x_p^4 \tag{3.43}$$

$$A_1 = -2a^8 b^2 x_p^3 - 2a^8 c^2 x_p^3 + 4a^{10} x_p^3 \tag{3.44}$$

$$\begin{aligned} A_2 = {} & a^6 b^2 x_p^2 y_p^2 + a^6 b^2 x_p^2 y_p^2 + a^8 x_p^4 - a^6 c^4 x_p^2 - 4a^6 c^2 b^2 x_p^2 \\ & + 6a^8 c^2 x_p^2 - b^2 a^6 x_p^2 + 6a^8 b^2 x_p^2 - 6a^{10} x_p^2 \end{aligned} \tag{3.45}$$

$$\begin{aligned} A_3 = {} & 2a^4 c^2 b^2 y_p^2 x_p - 2a^6 z_p^2 c^2 x_p + 2a^4 b^2 c^2 x_p y_p^2 - 2a^4 b^2 c^4 x_p + 2a^6 b^2 x_p^3 \\ & + 2c^2 a^6 x_p^3 - 4a^8 x_p^3 - 2a^4 b^2 c^4 x_p + 2c^4 a^6 x_p + 8a^6 b^2 c^2 x_p + 2c^2 a^6 x_p \\ & - 6a^8 b^2 x_p - 6a^8 c^2 x_p + 4a^{10} x_p \end{aligned} \tag{3.46}$$

$$\begin{aligned} A_4 = {} & b^2 a^2 c^4 y_p^2 - 2a^4 b^2 c^2 y_p^2 + a^6 b^2 y_p^2 + a^2 b^4 c^2 z_p^2 + a^4 b^4 x_p^2 - 2a^4 b^2 c^2 z_p^2 + 4a^4 b^2 c^2 x_p^2 \\ & - 6a^6 b^2 x_p^2 + a^4 c^4 x_p^2 - 6a^6 c^2 x_p^2 + 6a^8 x_p^2 - a^2 b^4 c^4 + 2a^4 b^4 c^2 - a^6 b^4 + 2a^4 b^2 c^4 - 4a^6 b^2 c^2 \\ & + 2a^8 b^2 - a^6 c^4 + 2a^8 c^2 - a^{10} \end{aligned} \tag{3.47}$$

$$\begin{aligned} A_5 = {} & -2a^4 b^4 x_p + 2a^4 b^2 c^2 x_p + 2a^2 b^2 c^4 y_p - 8a^4 b^2 c^2 y_p \\ & + 6a^6 b^2 y_p - 2a^4 c^2 x_p + 6a^6 c^2 x_p - 4a^8 x_p \end{aligned} \tag{3.48}$$

$$A_6 = a^4c^4 - 2a^2c^4b^2 + a^4b^4 + a^4c^4 - 2b^4c^2a^2 + 4a^4b^2c^2 - 2a^6b^2 - 2a^6c^2 + a^8 \quad (3.49)$$

- Finding polynomial roots:

  To get the $\hat{x}$ coordinate of the point on the ellipsoidal grain surface which gives the perpendicular distance to the mesh point (x_p, y_p, z_p) outside the ellipsoid, the real roots of the polynomial must be calculated. The Newton-Raphson method [Press (1992)] is one tool which can be used to find polynomial roots. This method requires an initial guess (x_0) of the root (r) of the function $(f(x))$. The goal of any numerical process is to make a good estimate of the root. The Newton-Raphson method does so by finding the intersection ,(x), point of the tangent line at the initial guess point $(x_0, f(x_0))$. The tangent equation at (x_0) is;

  $$f(x) = f(x_0) + \acute{f}(x_0)(x - x_0) \quad (3.50)$$

  for integer value of n:

  $$x_n \rightarrow r$$
  $$as$$
  $$n \rightarrow \infty$$

  if the tangent line intersects $x-axis$ at $(x_1, f(x_1))$, this x value gives the next root estimate, hence:

  $$x_1 = x_0 - \frac{f(x_0)}{\acute{f}(x_0)} \quad (3.51)$$

  The Newton-Raphson is an iterative method, therefore, the process is repeated until a good convergence of the root is reached.

The latter formula is the Newton-Raphson (N-R) formula for finding roots of function by starting initial guess of the root, iterating the proceed to obtain a good estimating of the root. For the problem at hand the initial guess for $\hat{x}$ was chosen to be x_s, a point on the ellipsoid perimeter.

Applying N-R formula to polynomial 3.42 gives $\hat{x}$-coordinate of its root .

- Calculating the $\hat{y}$-coordinate of the polynomial root:

  The corresponding $\hat{y}$-coordinate of the root calculated in the previous step when $\hat{x}$ and $\hat{z}$ coordinates are known can be given by the relation:

$$\frac{\hat{x}^2}{a^2} + \frac{\hat{y}^2}{b^2} + \frac{\hat{z}^2}{c^2} - 1 = 0 \tag{3.52}$$

  when $\hat{x}$ and $\hat{z}$ are known, the latter equation becomes a quadratic for $\hat{y}$ of the form:

$$\sum_{i=0}^{2} D_i y^i = 0 \tag{3.53}$$

  where:

$$D_0 = b^2c^2x^2 + a^2b^2z^2 - (abc)^2 \tag{3.54}$$

$$D_1 = 0 \tag{3.55}$$

$$D_2 = (ac)^2 \tag{3.56}$$

  The roots of a quadratic formula of the form $q_2x^2 + q_1x + q_0 = 0$ are given by:

$$x = \frac{-q_1 \pm \sqrt{q_1^2 - 4q_0q_2}}{2q_2} \tag{3.57}$$

- Calculating distance from the point (x_s, y_s, z_s) to the point (x_p, y_p, z_p) :

  The points on the ellipsoid surface (x_s, y_s, z_s) and the nearest grid point (x_p, y_p, z_p) outside the ellipsoid were calculated. The distance between these two points can be calculated via the relation:

$$d(x_p, y_p, z_p) = \sqrt{(x_s - x_p)^2 + (y_s - y_p)^2 + (z_s - z_p)^2} \tag{3.58}$$

  Then equation 3.22 can be used to calculate the potential at the grain surface.

Alternatively, one can express the polynomial with respect to the y-coordinate and get:

$$\sum_{i=0}^{6} B_i y^i \tag{3.59}$$

in which:

$$B_0 = -b^{10} y_p^4 \tag{3.60}$$

$$B_1 = -2a^2 b^8 y_p^3 - 2b^8 c^2 y_p^3 + 4b^{10} y_p^3 \tag{3.61}$$

$$\begin{aligned} B_2 = a^2 b^6 x_p^2 y_p^2 + b^6 c^2 y_p^4 z_p^2 + b^8 y_p^4 - a^4 b^6 y_p^2 - 4a^2 c^2 b^6 y_p^2 + 6a^2 b^8 y_p^2 \\ - c^2 b^6 y_p^2 + 6b^8 c^2 y_p^2 - 6b^{10} y_p^2 \end{aligned} \tag{3.62}$$

$$\begin{aligned} B_3 = 2a^2 c^2 b^4 x_p^2 y_p - 2a^2 x_p^2 b^6 y_p + 2a^2 b^4 c^2 y_p^2 z_p^2 - 2a^2 b^4 c^4 y_p + 2a^2 b^6 y_p^3 + 2c^2 b^6 y_p^3 \\ - 4b^8 y_p^3 + 2a^4 b^4 c^2 y_p + 2c^4 b^6 y_p + 8a^2 b^2 c^2 y_p - 4c^2 b^6 z_p^2 y_p^3 \\ - 6a^2 b^8 y_p - 6b^8 c^2 y_p + 4b^{10} y_p \end{aligned} \tag{3.63}$$

$$B_4 = b^2a^2c^2x_p^2 - 2a^2b^4c^2x_p^2 + a^2b^6x_p^2 + a^4b^2c^2z_p^2 + 4a^2b^4c^2y_p^2 - 6b^6c^2y_p^2 + a^4b^4y_p^2 + a^4b^4y_p^2 + 6b^6c^2y_p^2z_p^2 - 4a^2b^4c^2y_pzp^2 + 4a^2b^4c^2yp^2 - 6a^2b^6y_p^2 + b^4c^4y_p^2 - 6b^6a^2y_p^2 + 6b^8y_p^2 - a^4b^2c^4 + 2a^4b^4c^2 - a^4b^6 + 2a^2b^4c^4 - 4a^2b^6c^2 + 2a^2b^8 - b^6c^4 + 2c^2b^8 - b^{10} \tag{3.64}$$

$$B_5 = -2c^4b^4y_p + 2a^4b^2c^2y_p + 2a^2b^2c^4y_p - 8a^2b^4c^2y_p + 6a^2b^6y_p - 2b^4a^4yp + 6b^6c^2yp - 4b^8yp - 4b^6c^2z_p^2y_p + 2a^2b^4c^2z_p^2 \tag{3.65}$$

$$B_6 = a^4c^4 - 2a^4c^2b^2 + a^4b^4 - 2b^2c^2a^2 + 4b^4c^2a^2 - 2a^2b^6 + b^6c^2z_p^2 + b^8 \tag{3.66}$$

This is solved numerically via The Newton-Raphson Method to give the $\hat{y}$ coordinate of the point of the ellipsoid surface which gives the perpendicular distance to point (x_p, y_p, z_p). The corresponding $\hat{x}$-coordinate is obtained via Eq. 3.52. This equation, when $\hat{y}$ and $\hat{z}$ are known, becomes a quadratic for $\hat{x}$:

$$\sum_{i=0}^{2} E_i x^i = 0 \tag{3.67}$$

where:

$$E_0 = a^2c^2y^2 + a^2b^2z^2 - (abc)^2 \tag{3.68}$$

$$E_1 = 0 \tag{3.69}$$

$$E_2 = (bc)^2 \tag{3.70}$$

The roots of quadratic formula 3.67 are given by equation 3.57

Also the polynomial can be expressed in relation to z via following similar procedure ,

$$\sum_{i=0}^{6} C_i \tag{3.71}$$

in which:

$$C_0 = -c^{10} z_p^4 \tag{3.72}$$

$$C_1 = -2c^8 a^2 z_p^3 - 2c_8 b^2 z_p^3 + 4c^{10} z_p^3 \tag{3.73}$$

$$C_2 = c^6 a^2 x_p^2 z_p^2 + c^6 b^2 z_p^2 y_p^2 + c^8 z_p^4 - a^4 c^6 z_p^2 - 4a^2 c^6 b^2 z_p^2 + 6a^2 c^8 z_p^2 - b^4 c^6 z_p^2 + 6b^2 c^8 z_p^2 - 6c^{10} z_p^2 \tag{3.74}$$

$$C_3 = 2a^2 c^4 b^2 x_p^2 z_p - 2a^2 x_p^2 c^6 z_p + 2a^2 b^2 c^4 z_p y_p^2 - 2a^4 b^2 c^4 z_p + 2a^2 c^6 z_p^3 + 2b^2 c^6 z_p^3 - 4c^8 z_p^3 - 2a^2 b^4 c^4 z_p + 2a^4 c^6 z_p + 8a^2 b^2 c^6 z_p + 2c^6 b^4 z_p - 6a^2 c^8 z_p - 6b^2 c^8 x z_p + 4c^{10} z_p \tag{3.75}$$

$$C_4 = b^4 a^2 c^2 x_p^2 - 2a^2 b^2 c^4 x_p^2 + a^2 c^6 z_p^2 + a^4 b^2 c^2 y_p^2 + a^4 c^4 z_p^2 - 2a^2 b^2 c^4 y_p^2 + 4a^2 b^2 c^4 z_p^2 - 6a^2 c^6 z_p^2 + b^4 c^4 z_p^2 - 6b^2 c^6 z_p^2 + 6c^8 z_p^2 - a^4 b^2 c^4 + 2a^4 b^2 c^4 - a^4 c^6 + 2a^2 b^4 c^4 - 4a^2 b^2 c^6 + 2a^2 c^8 - b^4 c^6 + 2b^2 c^8 - c^{10} \tag{3.76}$$

$$C_5 = -2a^4 c^4 z_p + 2a^4 b^2 c^2 z_p + 2a^2 b^4 c^2 z_p - 8a^2 b^2 c^4 z_p + 6a^2 c^6 z_p - 2b^4 c^4 z_p + 6b^2 c^6 z_p - 4c^8 y_p \tag{3.77}$$

$$C_6 = b^4 c^4 - 2a^4 c^2 b^2 + a^4 c^4 + b^4 c^4 - 2b^4 c^2 a^2 + 4a^2 b^2 c^4 - 2a^2 c^6 - 2b^2 c^6 + c^8 \tag{3.78}$$

The technique described here is better than simply making the grid size small enough that any irregularity in boundary conditions is negligible. Equation 3.22 is used to describe the electric potential based on the distance $d(\hat{x}, \hat{y}, \hat{z})$ from the source. One can simply refine the mesh size to be very tiny and calculate the surface potential to be the source potential in 3.22 without ignoring the distance $d(\hat{x}, \hat{y}, \hat{z})$ from the ellipsoid surface and the nearest mesh points. The result can be seen in fig.3.2, which shows an example of the ellipsoid grain potential calculated using only a simple method to set a small grid size. It can be noticed the un accurate boundary conditions and a messy potential on the ellipsoid surface. In contrast, Fig.3.3 shows the electric potential of an ellipsoidal dust using the technique described in this chapter, where Eq. 3.22 is used and the distance $d(\hat{x}, \hat{y}, \hat{z})$ from the source to the nearest grid points is calculated using the technique of Lagrange multiplier and the Finite difference method to compute the potential outside the ellipsoidal grain. It is clear from the figure the accurate and smooth boundary conditions when using the interpolator methods described in this chapter.

3.3 Ions' surface deposition

In the presence of the electric field and the absence of the magnetic field, ions that have certain kinetic energy follow the electric field lines of charged grains; consequently, one can calculate the hitting positions of the ions on the grain surface $(\hat{x_d}, \hat{y_d}, \hat{z_d})$ by calculating the intersection points between the grain and lines joining the initial position outside the grain and the final ion positions inside the grain [Stark et al. (2006)]. However, the presence of the magnetic field in this study may affect the trajectories of the ions, let them diverge from electric field lines. A way to compare the two situations is therefore, needed. Calculation of the hitting positions of ions in the presence of electric and magnetic fields is done using the RK technique. To find the expected collision positions under the influence of the electric field only, the points of intersections between the equation of the ellipsoid and the equation of the line join the initial

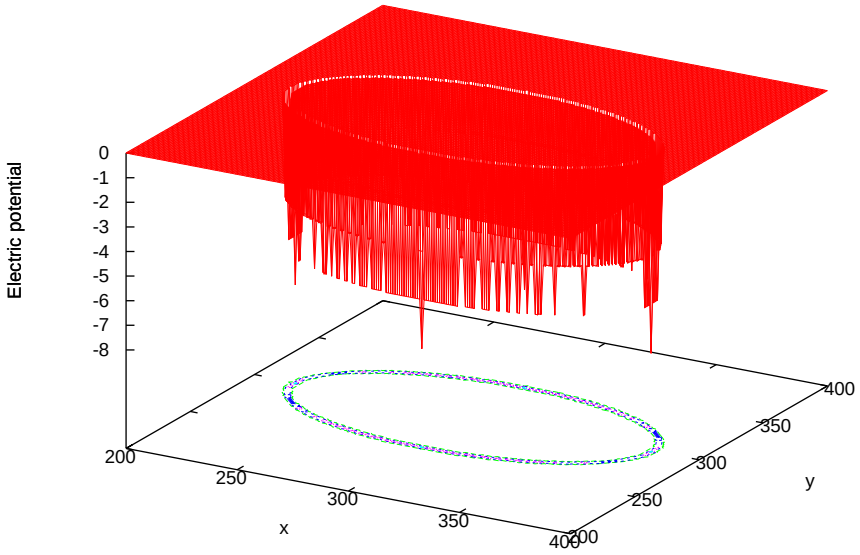

Figure 3.2: Plot shows the surface boundaries of a 2D slice of the electric potential for a dust grain has a = 80, b=40 and c = 40. The calculation here based on making the grid size small enough that any irregularity in boundary conditions is negligible with ignoring calculating the distance $d(\hat{x}, \hat{y}, \hat{z})$ from the ellipsoid surface and the nearest mesh points in Eq.3.22. The graph illustrates messy boundary conditions.

position of the ion outside the grain $(\hat{x_1}, \hat{y_1}, \hat{z_1})$ and the final ion positions inside the grain $(\hat{x_2}, \hat{y_2}, \hat{z_2})$ are calculated:

The equation of the ellipsoid is:

$$\frac{\hat{x}^2 - \hat{x_0}}{a^2} + \frac{\hat{y}^2 - \hat{y_0}}{b^2} + \frac{\hat{z}^2 - \hat{z_0}}{c^2} - 1 = 0 \tag{3.79}$$

where $(\hat{x_0}, \hat{y_0}, \hat{z_0})$ is the centre of the ellipsoid.

if M is the slop of the line joining the points $(\hat{x_1}, \hat{y_1}, \hat{z_1})$ and $(\hat{x_2}, \hat{y_2}, \hat{z_2})$ then:

$$\hat{y} = M(\hat{x} - \hat{x_1}) + \hat{y_1} \tag{3.80}$$

$$\hat{y} = M\hat{x} + d \tag{3.81}$$

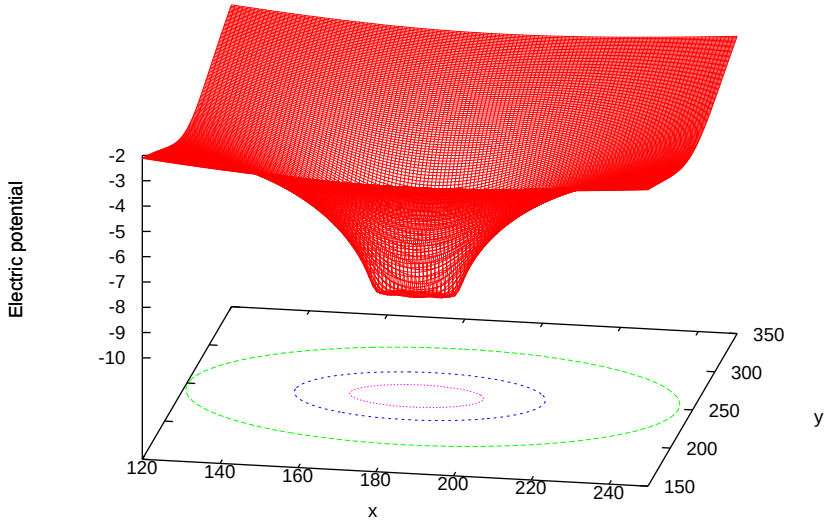

Figure 3.3: Plot shows the surface boundaries of a 2D slice of the electric potential for a dust grain has a = 10, b=5 and c = 5. The calculation used the technique of Lagrange multiplier and the Finite difference method to compute the potential outside the ellipsoidal grain. Graph illustrates the smooth boundary conditions obtained via the interpolator method introduced in the text.

$$\hat{z} = M(\hat{x} - \hat{x_1}) + \hat{z}_1 \tag{3.82}$$

$$\hat{z} = M\hat{x} + e \tag{3.83}$$

$$\hat{z} = M(\hat{y} - \hat{y_1}) + \hat{z}_1 \tag{3.84}$$

$$\hat{z} = M\hat{y} + i \tag{3.85}$$

where:

$$d = \hat{y}_1 - M\hat{x}_1 \tag{3.86}$$

$$e = \hat{z}_1 - M\hat{x}_1 \tag{3.87}$$

$$i = \hat{z}_1 - M\hat{y}_1 \tag{3.88}$$

expanding the equation of the ellipsoid gives:

$$\frac{\hat{x}^2 - 2\hat{x}\hat{x}_0 + \hat{x}_0^2}{a^2} + \frac{\hat{y}^2 - 2\hat{y}\hat{y}_0 + \hat{y}_0^2}{b^2} + \frac{\hat{z}^2 - 2\hat{z}\hat{z}_0 + \hat{z}_0^2}{c^2} = 1 \tag{3.89}$$

substituting equation 3.81 and 3.82 in equation 3.89 yields a quadratic equation in $\hat{x}$:

$$\sum_{i=0}^{2} G_i \hat{x}^i = 0 \tag{3.90}$$

in which:

$$G_0 = b^2c^2 + a^2c^2M^2 + a^2b^2M^2 \tag{3.91}$$

$$G_1 = -2b^2c^2\hat{x}^2 + (2a^2c^2d - 2a^2b^2\hat{y}_0 + 2a^2b^2e - 2a^2b^2\hat{z}_0)M \tag{3.92}$$

$$G_2 = b^2c^2\hat{x}_0^2 + a^2c^2d^2 - 2a^2c^2d\hat{y}_0 + a^2c^2\hat{y}_0^2 + a^2b^2e^2 - 2a^2b^2e\hat{z}_0 + a^2b^2\hat{z}_0^2 - a^2b^2c(M\hat{x} + e)\hat{z}^2 \tag{3.93}$$

The roots of equation 3.90 are given by the quadratic formula:

$$x = \frac{-G_1 \pm \sqrt{G_1^2 - 4G_0G_2}}{2G_2} \tag{3.94}$$

A quadratic equation in terms of $\hat{y}$ can be obtained by substituting equation 3.81 and 3.82 in equation 3.89 yielding:

$$\sum_{i=0}^{2} H_i \hat{y}^i = 0 \tag{3.95}$$

where:

$$H_0 = a^2 c^2 \tag{3.96}$$

$$H_1 = -2a^2 c^2 \hat{y}_0^2 \tag{3.97}$$

$$H_2 = b^2 c^2 \hat{x}_0^2 + a^2 c^2 d^2 - 2 * a^2 c^2 d\hat{y}_0 + a^2 c^2 \hat{y}_0^2 + a^2 b^2 e^2 - 2 * a^2 b^2 e\hat{z}_0 + a^2 b^2 \hat{z}_0^2 - a^2 b^2 c(M\hat{y} + i)\hat{z}_0^2 \tag{3.98}$$

The polynomial is solved for $\hat{y}$ using the quadratic formula (Eq.3.3). Once the $\hat{x}$, and $\hat{y}$ coordinates have been obtained, the corresponding $\hat{z}$ coordinate can be found from equation 3.89. This yields the point of deposition on the ellipsoid surface $(\hat{x}_d, \hat{y}_d, \hat{z}_d)$ in the presence of the electric field only.

3.4 Conclusion

This chapter set out to extend the work carried out by Stark (2008) and develop the technics of calculating the electric potential of the ellipsoidal dust in three dimensions to be applied in the dust growth treatment in the magnetised plasma context . A relaxation method used to solve the diffusion equation instead of Laplace equation described the electric potential of a charged dust grain. The finite difference method was explained in three dimensions and was applied to calculate the potential of ellipsoidal grains in three dimensions. An accurate technique based on the Lagrange multiplier was discussed and used to set potential on an ellipsoid grain surface. It was demonstrated that the technique described in this chapter is better than simply making the grid size small enough that any irregularity in boundary conditions is negligible. The

calculating of the electric potential of an ellipsoidal dust using the technique described in this chapter, where Eq. 3.22 is used and the distance $d(\hat{x}, \hat{y}, \hat{z})$ from the source to the nearest grid points is calculated using the technique of Lagrange multiplier and the Finite difference method to compute the potential outside the ellipsoidal grain, gives an accurate boundary conditions of the ellipsoidal grain. Computing the electric potential in such a way is the first step in studying ellipsoidal dust grain growth in a more reliable way. The next chapter uses the method by which the electric potential of ellipsoids grains was calculated here to study dust grain growth in three dimensions.

4

2D and 3D ellipsoidal dust growth simulation

4.1 Introduction

This chapter aims to develop the work done in chapter 2. A fully three dimensional model consisting of negatively charged ellipsoidal grains is considered. The finite difference method discussed in Chapter 3 is applied to calculate electric potential of the grain. The technique of setting a potential on an accurate ellipsoidal dust surface which was investigated in the previous chapter is used. One important question is what conditions imply a large aspect ratio growth for ellipsoidal grains. Results in this chapter attempt to answer this question.

4.2 2D and 3D Model Description

In dust in plasma studies, several scale lengths can be examined; for example, grain size, separation distance between dust and Debye length. In addition, Larmor radius at launch is an important scale length in electromagnetic environments. In this simulation, the relative sizes of Larmor radius versus characteristic grain length ($\alpha = R_L/b$

were considered, where R_L is the ion's Larmor radius at launch and b the minor axes of the grain) can be an important parameter affecting the possibility of ions hitting the grain. Here three cases of α are considered: $\alpha \simeq 1$, $\alpha \ll 1$ and $\alpha \gg 1$. Parameter p (which gives the relative size between the electric field to the magnetic field) will set to three values ($p = 0.1, 30, 8$). These values covers the high magnetic field, high electric field cases, and the case where both electric and magnetic effects are present. The number of simulated ions in the ions loading section is about 10^4 to be correspond to Coulomb dust crystals (see table 2.2). For typical space and laboratory plasmas, there is a distribution of grain sizes $\sim 0.01 - 5\mu m$ and $\sim 0.01 - 10\mu m$ for terrestrial and space plasmas respectively. At the sheath edge, the electric potential is taken to be zero. In such model, the grain size is assumed to be much smaller than the sheath length as in astrophysical environments.

Ions were launched within the sheath with launch velocity v_{launch} at $t = 0$ at two different initial positions; ions were distributed evenly along x axis, from $2a-15-2a+5$ where a is the major axis of the grain, and at perpendicular distance= $\sqrt{y^2 + z^2} = 2$ from the long grain axis, where (x, y, z) is the initial position of the ion, and the grain was parallel to x axis. The second initial positions ions were launched radially from same distance from the grain's centre. The value of this distance was equal to the perpendicular distance in the first initial positions set and ions were launched with same velocity=v_{launch}.

4.3 Numerical Simulation

The electric potential of dust grain were calculated. The grain's major axes was chosen to be twice the grain's minor axes; $a = 2b = 2c$, where a , b , and c are the major and minor axes of the grain in x ,y, and z directions, respectively. By following ions trajectories toward the dust grain and tracing their deposition sites on the grain surface, the dust growth trend can be examined. Number of colliding ions on the grain surface were compared with colliding ones at grain's ends.

Table 4.1: Parameters used in numerical simulations.

Simulation property	Value
$x-, y-$boundaries	$\phi = 0$
Number of launched ions	10^4
p	$0.1, 8, 30$
$d\hat{t}$	0.1
number of time steps	1500
ϕ	$-10V$
α	$1, \ll 1, \gg 1$
$a : b : c$	$10 : 5 : 5$
initial x	$a - 15$ to $2a + 5$
perp. launch distance	$2a/5$

4.4 Results and Discussion

4.4.1 Ion Dynamics

The ratio of Larmor radius to the grain size ($\alpha = R_L/b$, where R_L is the ion's Larmor radius at launch and b the minor axes of the grain) can be an important parameter affecting the possibility of ions hitting the grain. Here three cases of α are considered: $\alpha \simeq 1$, $\alpha \ll 1$ and $\alpha \gg 1$. The Larmor radius at launch is modified by changing the launch velocity only, while parameter p will set in the three cases to 8. In general, ion dynamics in the three choices of α have some similarity in that ions starting near the grain surface tend to collide on grain surface, whereas ions starting further away move in an orbital motion. The following sections illustrate the details of ion' behaviours.

[$\alpha \simeq 1$,$p = 8$]

The ion's launch velocity is chosen to give a Larmor radius at launch comparable to the grain size, as shown in Fig. 4.1. This velocity corresponds to $v_{launch} = 5$. Fig. 4.2 shows

some ion trajectories toward the grain. Most ions starting near the grain surface collide, while those starting further away execute an orbital motion around the magnetic field lines and drift toward the grain. Most of these ions collide on the grain at different sites. Only three ions from those represented in Fig. 4.2 miss. This can be explained as follows; the non-colliding ions start from positions far from the grain and as a result, they acquire energy while moving. Then these ions move near the grain's corner, which provides more gained energy, therefore, their Larmor radius increases. Hence they missed colliding because of their high velocities, resulting in their movement onto different electric field regions.

Ion Energy

The gained energies by some of the ions are shown in Fig. 4.3. It can be noticed that there are three ranges of acquired energies, according to the differences in the ions' trajectories. For example, ions moving directly from their initial positions near the grain's surface gained the lowest energies, while ions starting from positions far from the grain tend to acquire higher energies, as a result of moving for a longer time than the nearer ions. The highest energies seen in the graph are acquired by those ions which do not hit the grain, but instead follow trajectories near the grain's corners, as shown previously.

$[\alpha \ll 1, p = 8]$

Here the Larmor radius is much smaller than the grain size (see Fig. 4.4); the velocity is chosen as $v_{launch} = 2$. Other initial conditions are the same as in the previous case. Fig. 4.5 shows fewer colliding particles on a grain's surface than in the former case. Non colliding ions have a smaller Larmor radius that does not intersect with the grain position.

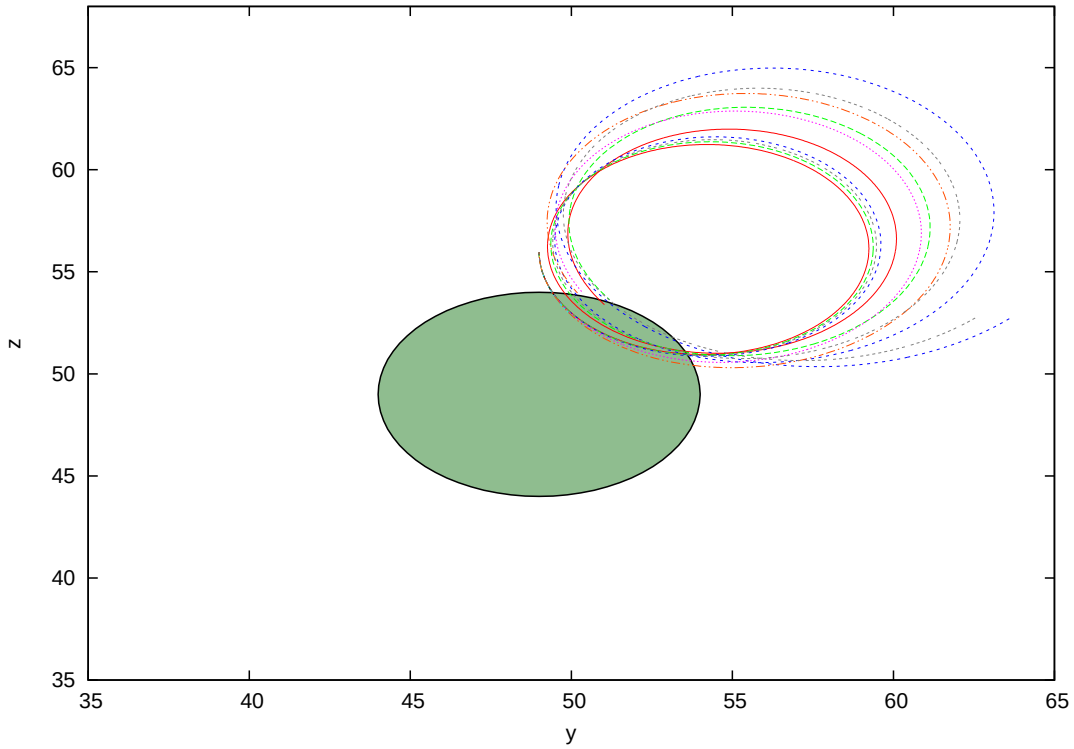

Figure 4.1: Ions' Larmor radius(R_L) at launch, which is comparable to the grain's semi axes (b),where parameter $p = 8$ [$R_L/b \simeq 1$,$p = 8$]. The ellipsoidal dust grain is represented in green.

Ion Energy

Similar energy patterns to previous cases can be noticed in Fig. 4.9 for those particles whose Larmor radius at launch is smaller than grain size in which colliding ions have lower energies than non-colliding ones . However, the reduction of the initial energies lead to a reduction in the final energies gained.

[$\alpha \gg 1$,$p = 8$]

In this situation, the Larmor radius at launch is grater than the grain size (see Fig. 4.7) where initial velocity $v_{launch} = 8$ is used. It is clear from Fig. 4.8 that all ions hit the grain. Unlike the two previous cases, the colliding ions are distributed along the grain's surface and corners, indicating that most ions with a Larmor radius at launch greater than the grain size are more likely to contribute to the grain's end growth.

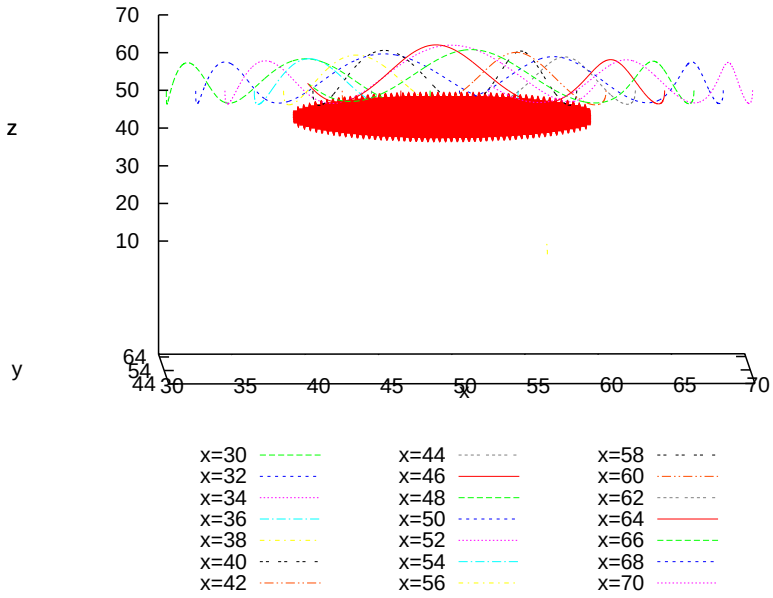

Figure 4.2: Ions' trajectories toward an ellipsoidal grain. The grain semi-axes a, b, c are $10, 5, 5$, in length respectively. Ions' Larmor radius(R_L) at launch is comparable to the grain's semi-axes (b),where parameter $p = 8$ [$R_L/b \simeq 1$,$p = 8$]. Note that most ions collide with the grain. The pink shape represents the dust.

Ions Energy

As the magnitude of the initial velocity increases, the magnitude of the maximum gained energies for particles have a larger Larmor radius than grain size also increases as it is clear in Fig. 4.6. It can be seen that the highest energies were gained by colliding ions, unlike the latter case, which start far from the grain and move near the grain's corners. However, the net acquired energies are lower here than previously (when $R_L/b \simeq 1$) for same particles at the same period of time.

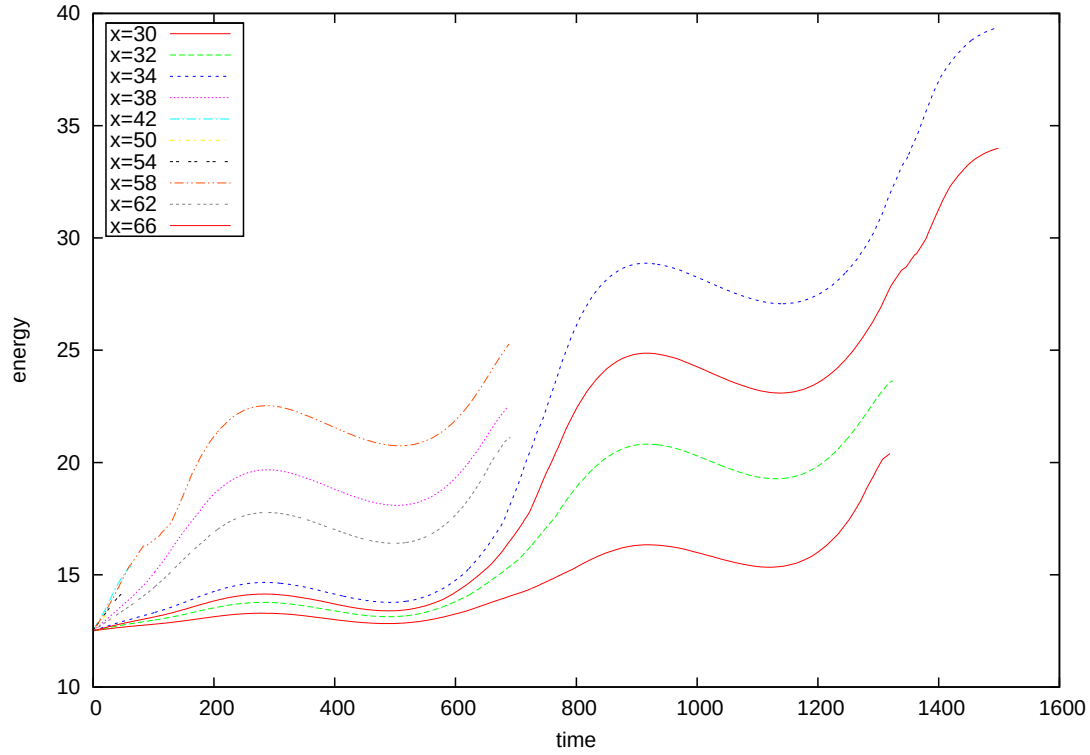

Figure 4.3: Energies of some ions represented in Fig.2 [$R_L/b \simeq 1$,$p = 8$]. Plot represents non-colliding ions which gain the highest energies. Note that the lowest energies are gained by ions start directly above the grain's surface . Ions starting further away gain higher energies.

4.5 Effect of Parameter p

An other important parameter is where the ratio of electric field to the magnetic field demonstrates the effect of parameter p (where $p = \frac{qE_0}{mw_c v_0}$). The following subsections indicate two cases of parameter p; large p value and small p value respectively. In both cases only the value of p changes; otherwise, all other conditions are similar to $\alpha \simeq 1$ case.

4.5.1 Dominant Electric Field

[$\alpha \simeq 1$,$p = 30$]

The parameter p here is large, corresponding to $p = 30$. Fig. 4.10 shows some

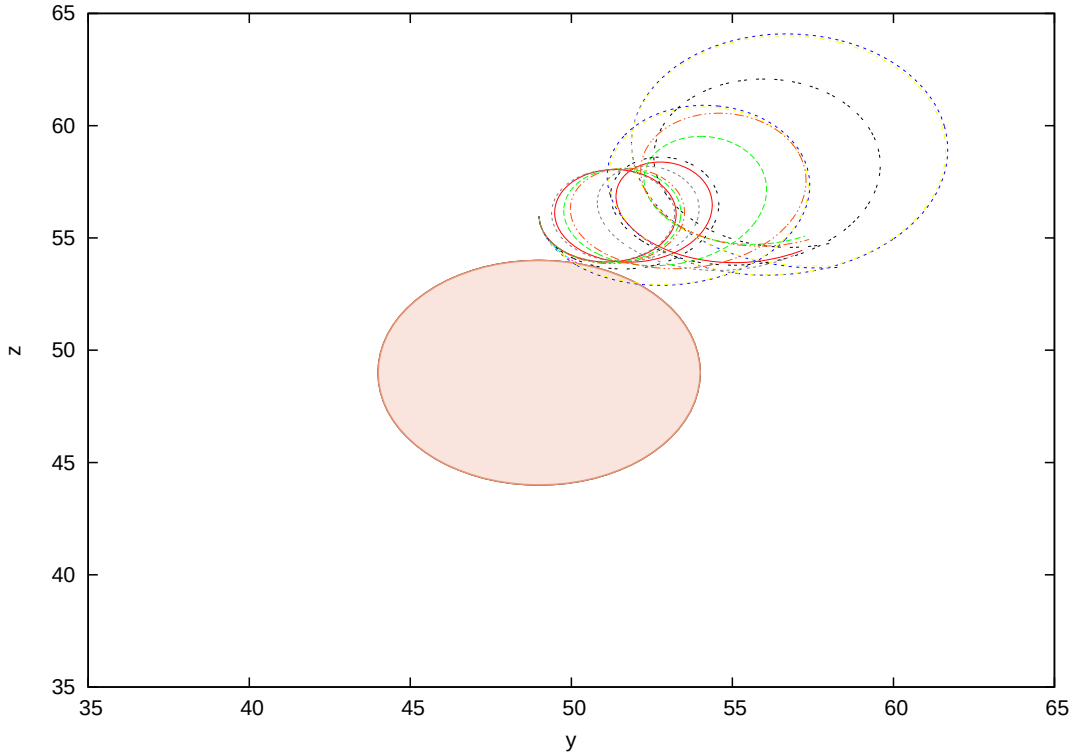

Figure 4.4: Ions Larmor radius(R_L) at launch which is much less than the grain's semi axes (b),where parameter $p = 8$ [$R_L/b \ll 1$,$p = 8$]. The pink shape represents the dust.

ions trajectories. As the electric field increases, the effect of drift motion becomes clearer than orbital motion. Ions are accelerated by the electric field resulting in large Larmor radii. Consequently, ions tend to gain high energies as shown in Fig. 4.11. The colliding ions have their lowest energies, whereas those starting from positions far from the grain gain the highest energies before their energies become almost stable.

4.5.2 Dominant Magnetic Field

[$\alpha \simeq 1$,$p = 0.1$]

Here parameter p is given a small value, corresponding to $p = 0.1$ to insure a dominant magnetic field effect. Particles starting near the surface collide, while other ions are forced into Larmor orbits that prevent them from reaching the grain, as shown in Fig. 4.12. Fewer colliding ions can observed than in the previous case, as illustrated

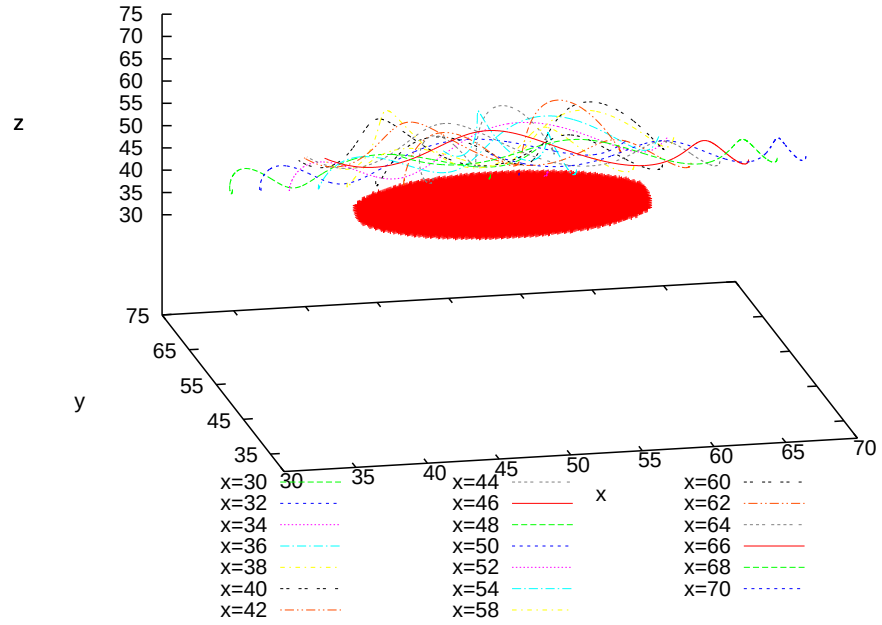

Figure 4.5: Ions trajectories toward an ellipsoidal grain.The grain semi-axes a, b, c are of lengthes $10, 5, 5$,respectively. Ions Larmor radius(R_L) at launch is much lesser than the grain's semi-axes (b),where parameter $p = 8$ [$R_L/b \ll 1$,$p = 8$]. Note that most ions do not collide the grain.

in the figure. Fig. 4.13 represents energies curves for some ions. Again, colliding ions have the lowest energies, while those moving near corners have the highest; then energies decrease as particles move toward the grain from positions further away.

4.6 Mass Loading

The effect of electric field, magnetic field and the orientation of the magnetic field on dust growth patterns have been investigated. This was examined in two different ways. First, many ion batches with significant number of ions are launched from different directions toward the grain. Every batch contains about 100 ions. Second, 10^4 ions are

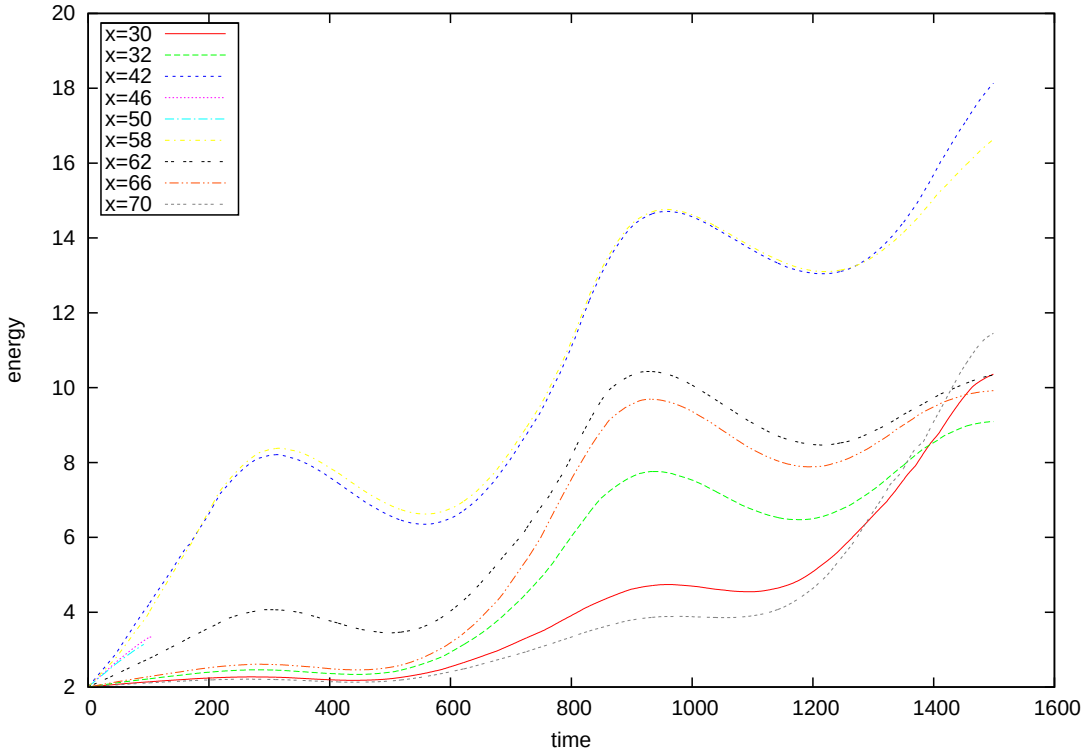

Figure 4.6: Energies of some ions represented in Fig.4.5 [$R_L/b \gg 1$,$p = 8$]. The plot represents colliding ions. Note that the lowest energies are gained by ions start directly above the grain's surface . Ions starting further away gain higher energies.

launched from a circular bar surrounding the ellipsoidal grain. The initial conditions are similar to those in case ($\alpha \simeq 1$), except for the initial particles positions. The following subsections address these effects.

4.7 The effect of electric and magnetic fields

Two cases will be considered: the growth of a spherical grain in the presence of an electric field only and the growth of an ellipsoidal grain in the presence of electric and magnetic fields, where the effect of magnetic field orientation will investigated.

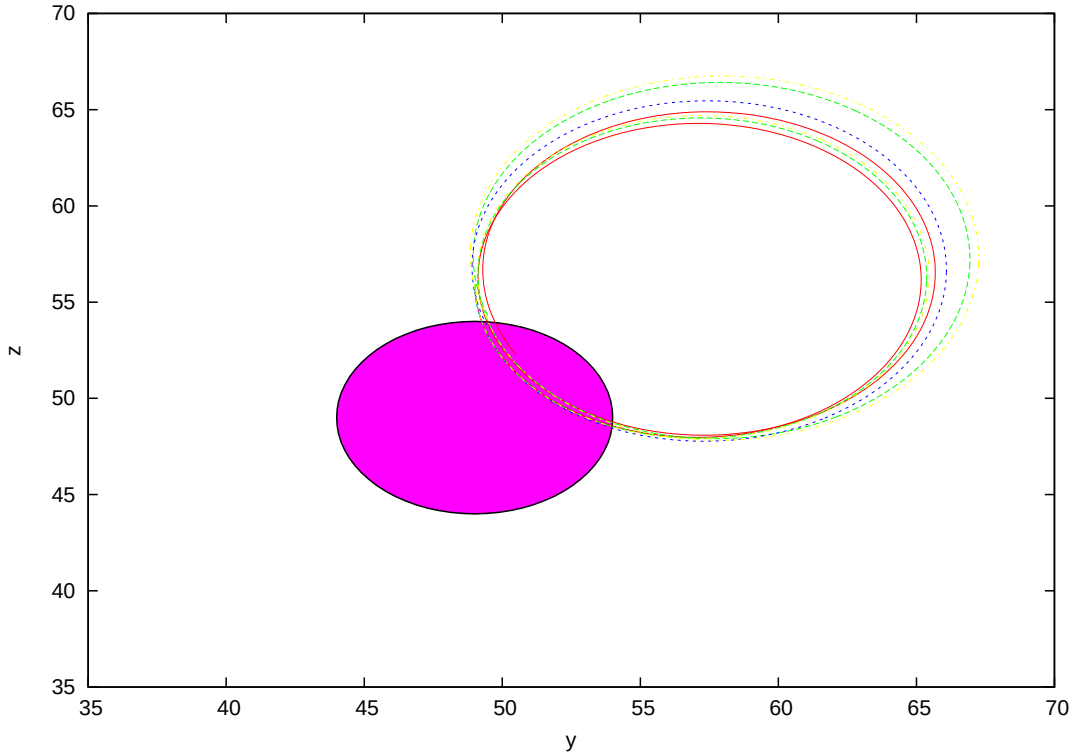

Figure 4.7: Ions' Larmor radius(R_L) at launch which is much greater than the grain's semi axes (b),where parameter $p = 8$ [$R_L/b \gg 1$,$p = 8$]. The dust is represented in pink color.

4.7.1 Growth of spherical grain in electrostatic field only

In the presence of an electrostatic field and absence of a magnetic field for a spherical dust grain, ions mass loading was studied. Ions were launched from a circular bar around the sphere. As shown in Fig. 4.14 ions follow the electric field lines of the negatively charged grain and hit the grain. Therefore, ions are distributed equally on grain surface.

4.7.2 Growth of ellipsoidal grain in electrostatic and magnetostatic fields

For an ellipsoidal grain and in the presence of electrostatic and magnetostatic fields, ions loading on grain surface will be investigated. The direction of the magnetic field

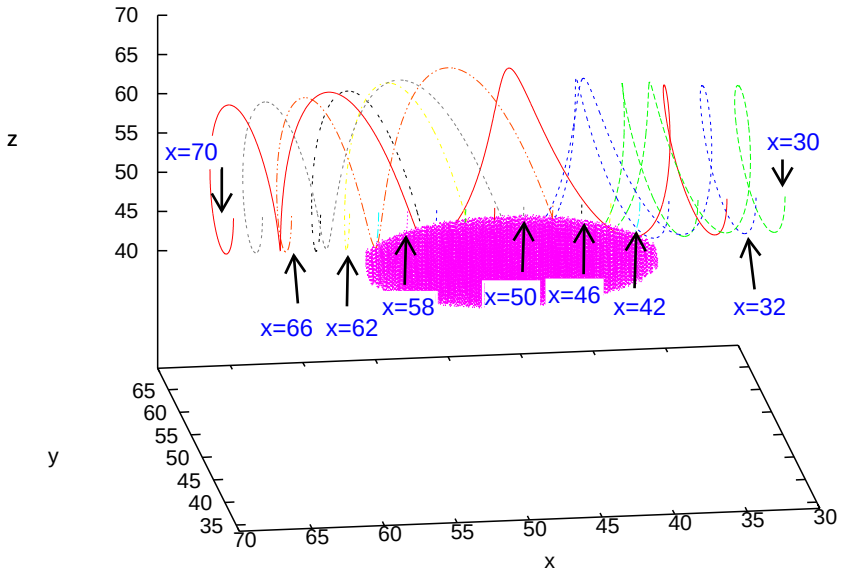

Figure 4.8: Ions trajectories toward an ellipsoidal grain.The grain semi-axes a, b, c are $10, 5, 5$ in length respectively. Ions Larmor radius(R_L) at launch is much greater than the grain's semi-axes (b), where parameter $p = 8$ [$R_L/b \gg 1$,$p = 8$]. Note that all ions collide with the grain's surface.

is critical for dust growth. Two situations will be considered: the growth of ellipsoidal grain in the presence of a parallel oriented (in respect to the major axes of the grain) magnetic field and the growth of ellipsoidal grain in the presence of a magnetic field perpendicular to the grain's surface (in z direction).

4.7.3 Parallel magnetic field

Batches of launched ions

Fig. 4.15 shows the density of ions colliding onto ellipsoidal grain surface. Every colour represents positions of ions from the same batch. Colours represent the density of colliding ions in different locations onto the grain's surface. It can be noticed there

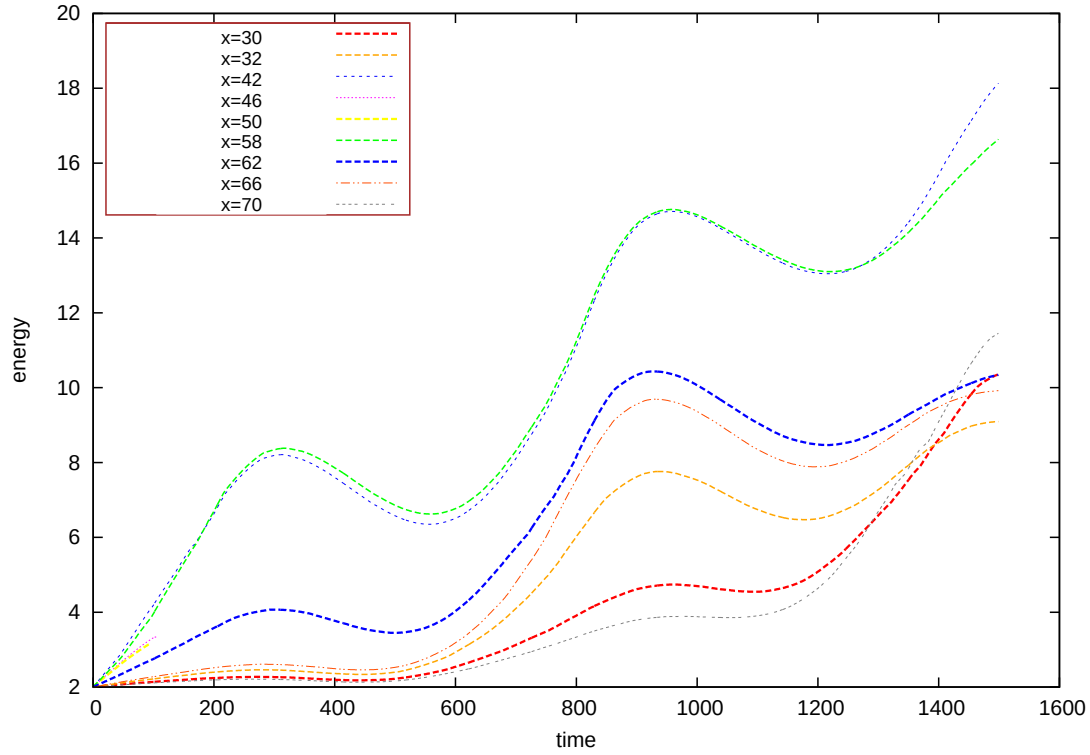

Figure 4.9: Energies of some ions represented in Fig.6 [$R_L/b \ll 1$,$p = 8$]. Note that the lowest energies are gained by colliding ions which start directly above the grain's surface. Ions starting further away (non-colliding ions) gain higher energies.

is higher ion accumulation near the grain's ends. The salient point here is that some ions which start far from the gain tend to collide onto the grain's surface as well as the grain ends. The situation is different when the magnetic field is perpendicular to the grain, as will be discussed later. Fig. 4.16 is similar to Fig. 4.15 represents ion density on the grain's surface with the initial batches positions are added. Ions' Larmor radius (R_L) at launch is comparable to the grain's semi-axis (b), where parameter $p = 8$ [$R_L/b \simeq 1$,$p = 8$], and magnetic field is parallel to x-axis. Figs. 4.17- 4.23 each represents the initial positions of one of the ion batches, the direct expected colliding position in the absence of a magnetic field and the actual colliding positions due to the combined influence of the grain's electrostatic field and the applied magnetic field. As the ions initial positions are near the grain's surface, ions shift from their directed

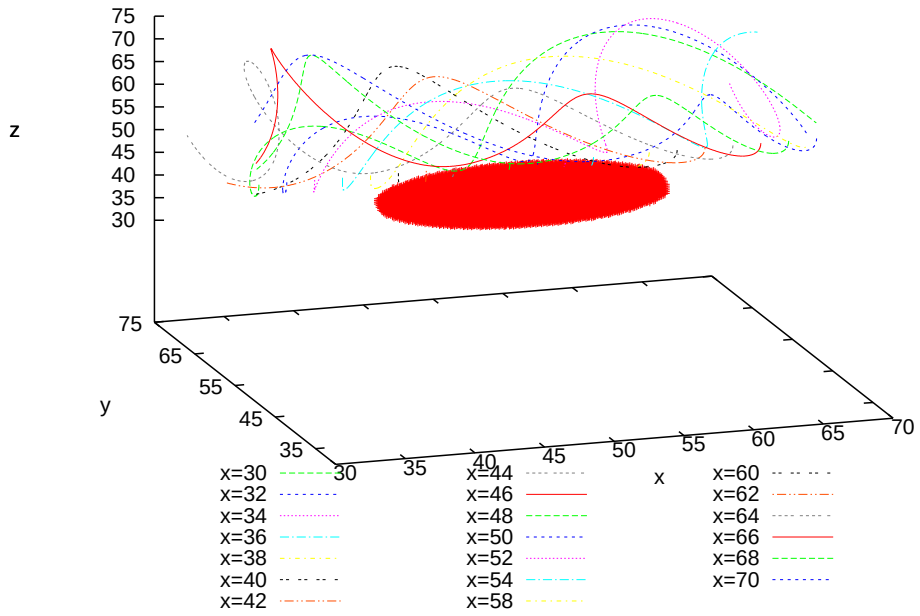

Figure 4.10: Ions trajectories toward an ellipsoidal grain. The grain semi-axes a, b, c are $10, 5, 5$ in length, respectively. Ions Larmor radius(R_L) at launch is comparable to the grain's semi-axes (b), and the electric field is large $p = 30$ [$R_L/b \simeq 1$,$p = 30$]. Note that the effect of drift motion is clearer than orbit motion. Some ions collide with the grain.

hitting positions towards the grain surface as in Fig.4.17. As ions start closer to the grain's end, they tend to hit the corner as well as the grain's surface as can be seen in Figs.4.18, and 4.19. For ions that start from batches that in front of the grain's ends or grain's sides, the ions tend to spread around their expected hitting positions on the grain, as in Figs.4.20-4.23. Fig. 4.24 shows frequency plot of the impact energies of ions where the magnetic field is parallel to the x-axis . It can be noticed from Fig. 4.24 that there are discrete energy bands. The following section discusses this effect.

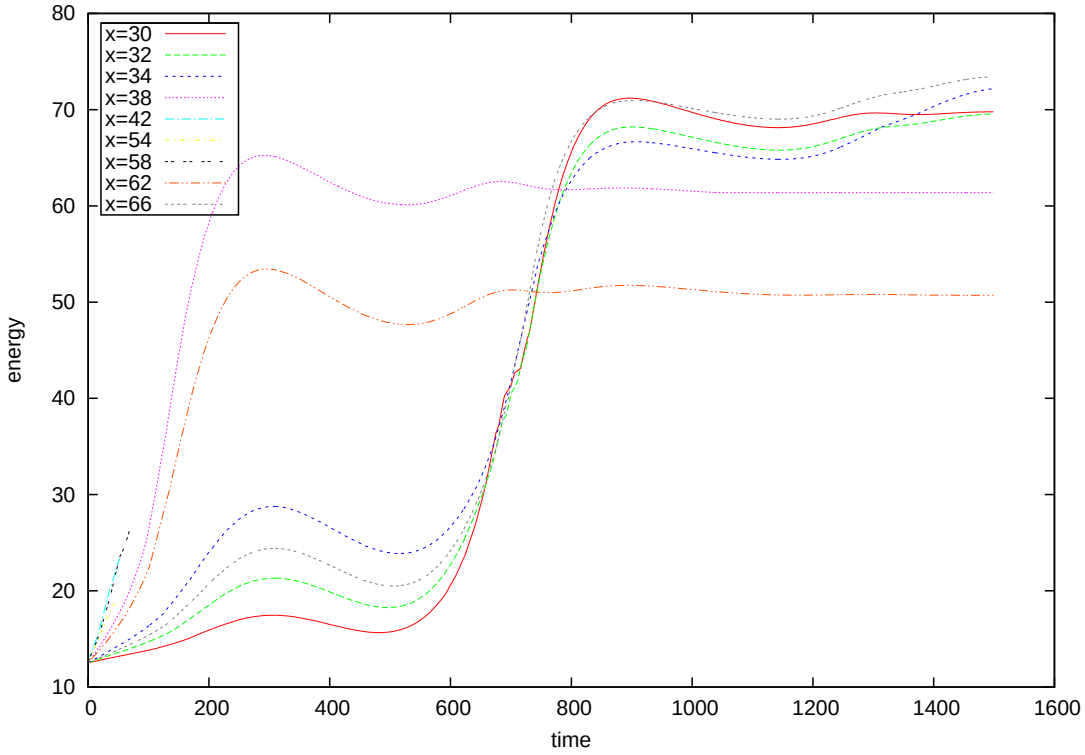

Figure 4.11: Energies of some ions represented in Fig.10 [$R_L/b \ll 1$,$p = 30$]. Note that the lowest energies are gained by colliding ions which start directly above the grain's surface . Ions starting further away (non-colliding ions) gain the highest energies before they become stable.

4.7.4 Distribution of ion energy

In the case of a perpendicular magnetic field and a constant electric field in x direction, the equations of motion in two-dimensions are given by,

$$\frac{dv_x}{dt} = \frac{q}{m}E_x \pm \omega_c v_y \tag{4.1}$$

$$\frac{dv_y}{dt} = \pm\omega_c v_x \tag{4.2}$$

by solving equations 4.1 and 4.2 the total speed $v = \sqrt{v_x^2 + v_y^2}$ gained by the particle is $v = \mu v_D$, where v_D is the drift velocity and μ is given by,

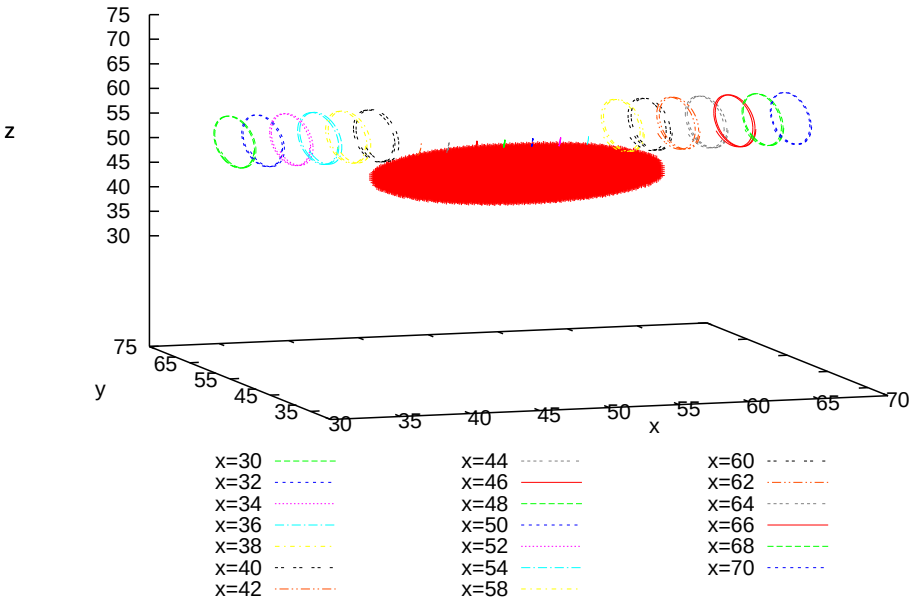

Figure 4.12: Ions trajectories toward an ellipsoidal grain.The grain semi-axes a, b, c are $10, 5, 5$ in length respectively. Ions' Larmor radius(R_L) at launch is comparable to the grain's semi-axes (b), where parameter is small $p = 0.1$ [$R_L/b \simeq 1$,$p = 0.1$]. Note that the effect of orbit motion is clearer than drift motion. Fewer ions collide with the grain than in the previous case $p = 30$.

$$\mu^2 = 2[1 - cos(\omega_c/\omega_p] \tag{4.3}$$

and the energy acquired by the particle becomes,

$$\varepsilon = \frac{1}{2}\mu^2 m v_D^2 = [1 - cos(\omega_c/\omega_p)] m v_D^2 \tag{4.4}$$

where $\omega_c = \frac{|q|B}{m}$ and $\omega_p = q\sqrt{\frac{n}{\epsilon_0 m}}$

The reason of the presence of ions that have a final energy lower than the initial energy is set in the following discussion: in the case of presence of a magnetic field, where $\omega_c > \omega_p$ then Debye length is larger than the Larmor radius and particles may be prevented from reaching grain position. In addition, particles execute further orbits

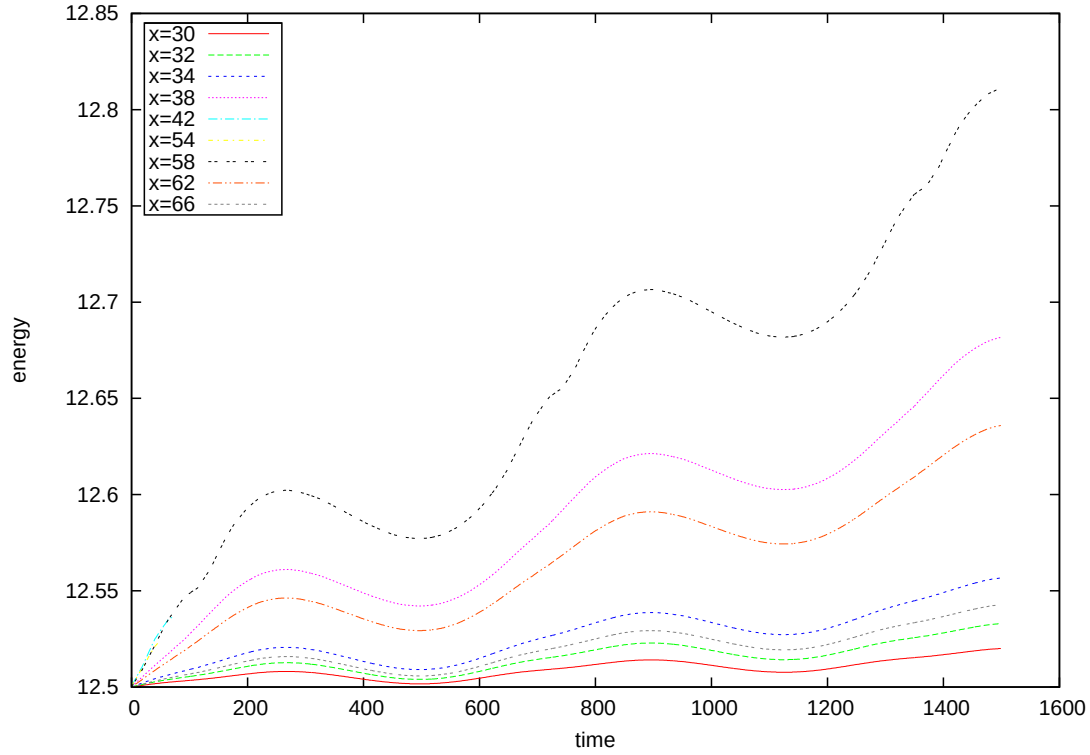

Figure 4.13: Energies of some ions represented in Fig.12 [$R_L/b \ll 1$,$p = 0.1$]. Note that colliding ions which start directly above the grain's surface gain low energies . Some other Ions (non-colliding ions) gain higher energies.

during cyclotron orbit. This means that the energy of colliding particles that collide at a time when they move against electric field direction reaches its minimum.

The reason of appearing of energy gaps is the following: for every half cycle of Larmor orbit, ions gain a magnitude of energy while moving in a drifting motion and they lose a magnitude of energy in the second half of the cycle. However, at these points ions can not collide with the grain as they are moving away from it. Therefore, gaps in energy curve are appeared and as ω_c increases more energy gaps are produced. That can be seen from Fig. 4.24 which shows a frequency plot of gained energies for the hitting ions. The energy gaps are result of presence of non colliding ions that moving in a second half of the Larmor orbit directed away from the grain or toward the grain but did not collide at this time, therefore, their energies are not recorded in

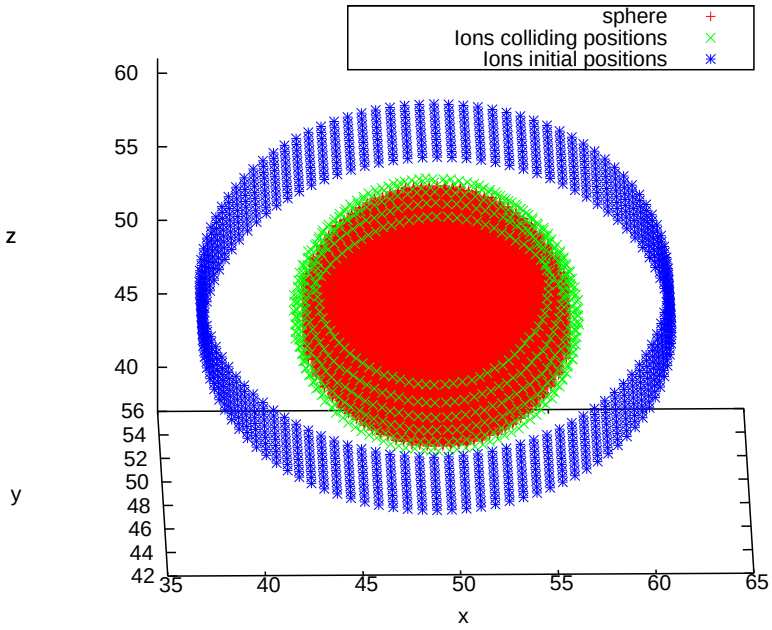

Figure 4.14: Ions follow electric field lines of the negatively charged spherical grain in the absence of a magnetic field (parameter $p = 500$). Therefore, ion distribution on the grain's surface is equal.

the energy curve.

Circular bar of launched ions

Figs. 4.25, and 4.26 shows ion distribution on an ellipsoidal grain. Ions are launched from a circular bar around the grain. It is clear from the graph that ions tend to hit the grain's ends. Ions moving parallel to magnetic field direction (ions starting near the grain's edge) do not meet any impediment to reaching the grain, while those ions moving perpendicularly to the direction of the magnetic field orbits around the grain preventing them from colliding with it.

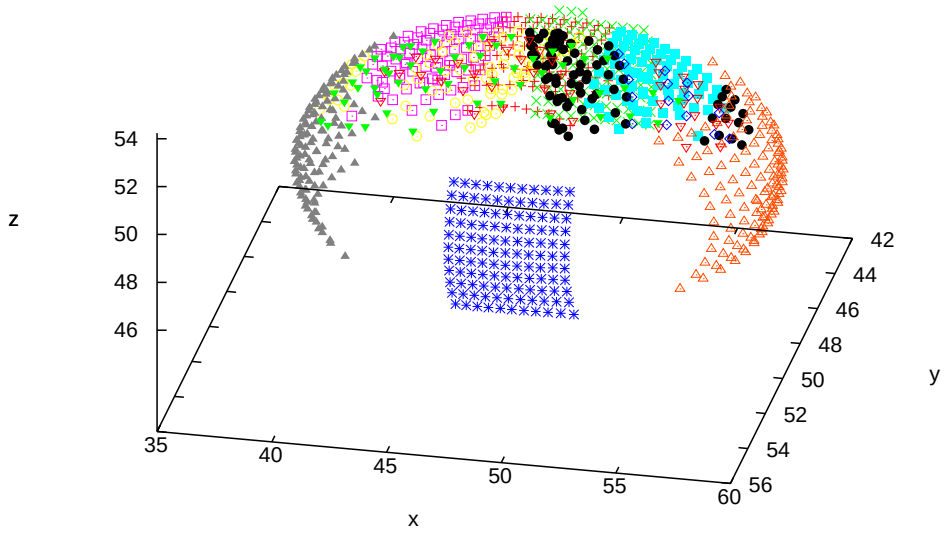

Figure 4.15: Coloured points represent ion density on the grain's surface. Every coloured symbol indicates ions belonging to the same batch. The grain's semi-axes a, b, c are $10, 5, 5$ in length respectively. Ions Larmor radius(R_L) at launch is comparable to the grain's semi-axes (b),where parameter $p = 8$ [$R_L/b \simeq 1$,$p = 8$],and magnetic field is parallel to x-axis.

4.7.5 Perpendicular Magnetic field

Batches of launched ions

Under the same initial conditions as the previous case, except for the direction of the magnetic field, the growth pattern of an ellipsoidal grain is addressed. Fig. 4.27 shows ion density on the grain surface sites, represented by coloured points. Ion density and their original batches are shown in Fig.4.28. It is clear from the figures that fewer ions hit the grain than in the previous case (81% in this case against 92% in the parallel magnetic field case). Most ions starting further away do not hit. However, colliding ones tend to collide at the grain's corners, accumulating in one corner more than others. Applying a stronger magnetic field, as shown in $1D$ simulation, causes more growth at

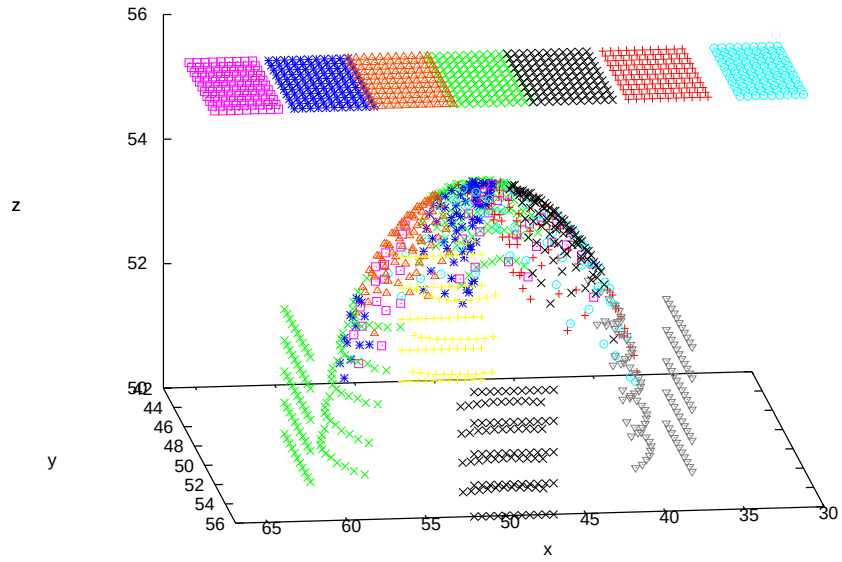

Figure 4.16: As the previous figure except the The initial positions of ion batches are added here.

one end than another as a result of $E \times B$ drift, i.e. ions drift towards end where there is greater growth, whereas ions near the other end drift away from it. That indicates more rapid growth at one corner than the other. Therefore, dust is likely to grow more elongated, although slowly, while the parallel magnetic field may cause more rapid growth in size. This may indicate the presence of size and shape distribution of dust in space environments. Figs. 4.29- 4.35 represent the initial positions of ion batches, the expected direct colliding position in the absence of a magnetic field (ions follow electric field lines) and the actual colliding positions due to the combined influence of the grain's electrostatic field and the applied magnetic field. Fig. 4.35 shows a frequency plot of energies of ions [$\alpha \ll 1$,$p = 8$], where the magnetic field is perpendicular to the x-axis. Fig. 4.35 shows a continuum energy distribution.

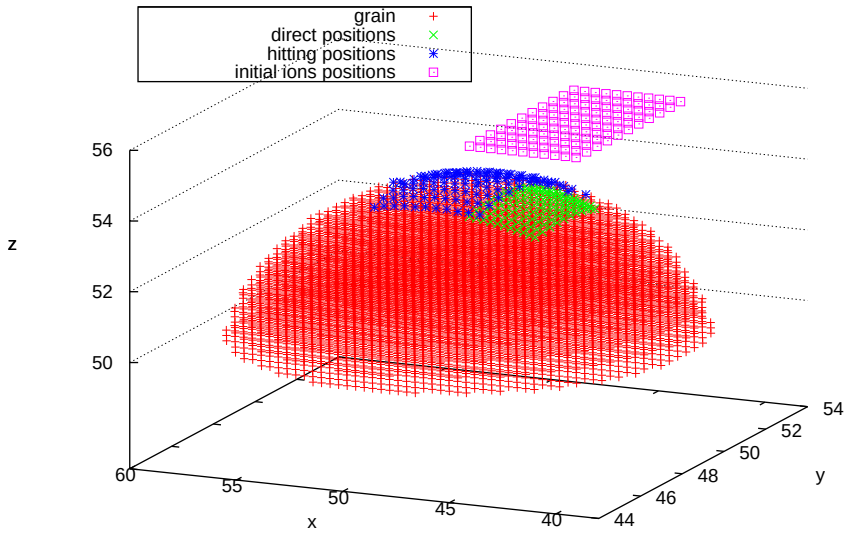

Figure 4.17: The initial positions of the ion batches, the expected direct colliding positions in the absence of a magnetic field and the actual colliding positions due to the combined influence of the grain electrostatic field and the applied parallel magnetic field. Ions have shifted from their directed hitting positions towards the grain surface.

Circular bar of launched ions

Ions were launched from a circular bar around the grain when the magnetic field was oriented perpendicularly to the grain's long axis. Figs. 4.36 and 4.37 represent the distribution of ion density and ions energies for this situation respectively. Ions tend this time to hit both the grain's surface and ends, although not in a symmetric way, while their energies have a continuum distribution.

4.8 Grain Shielding

The closed orbital motion of ions (trapped ions) in the vicinity of dust grains leads to a reduction in the effective sheath length of the grains. Estimating the number of trapped particles in the vicinity of grains is of significance in understanding dust growth mech-

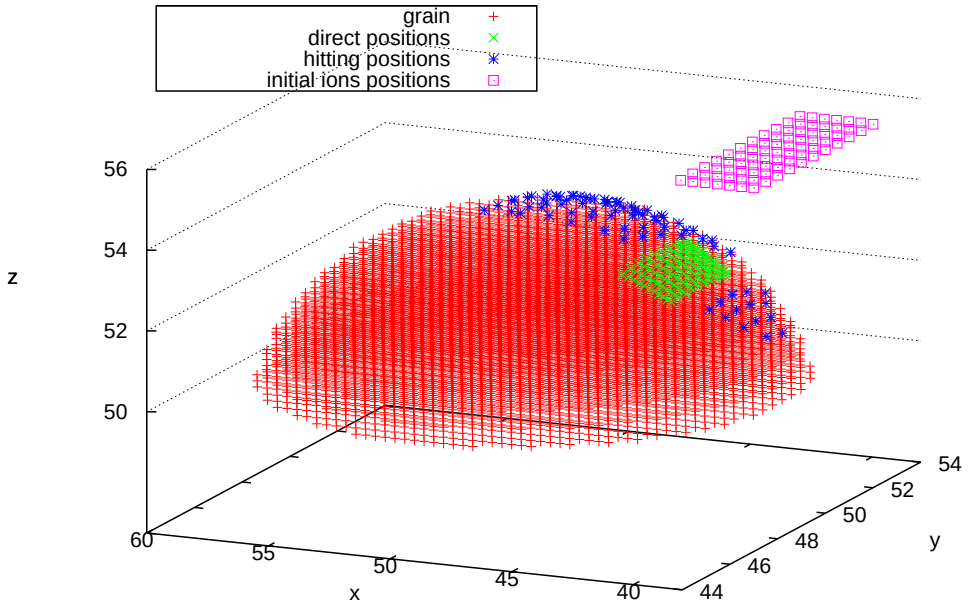

Figure 4.18: As Figure 4.17 but for a different ion batch. Here ions tend to hit the grain's surface and end as they start their motion closer to the grain's end.

anism. In this section we try to estimate the percentage of grain growth reducing as a result of the trapped ions effect. A cylinder of orbiting ions surrounding the grain was simulated. The magnetic field was oriented along the x-axis. About 1000 ions beyond the cylinder of trapped ions were launched from a circular bar.This can be compared to the same simulation without the cylinder of trapped ions. With trapped ions effect, only 95 ions collide with the grain corresponding to fewer than 25 percentage of ions miss colliding with the grain as a result of the trapped ions effect. Trapped particles shield electrostatic field of the grain and reduce its magnitude for other coming particles. The estimated percentage of non-colliding ions, as consequence of the effect of trapped ions, is not low and can not be negligible in simulation.

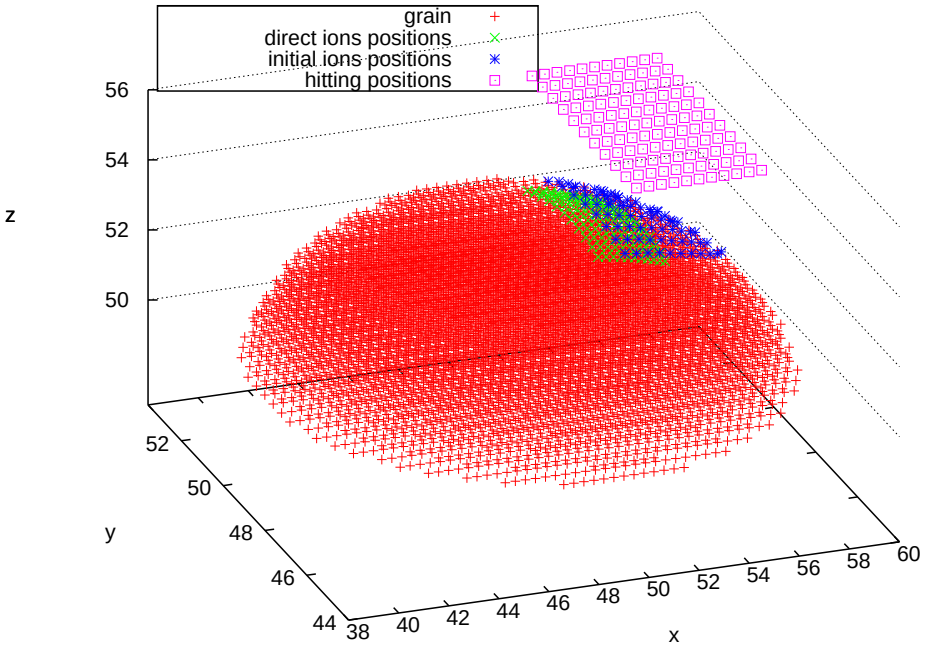

Figure 4.19: As Figure 4.17 but for a different ion batch. As ions started moving near the corner, their hitting positions shifted toward grain's corner.

4.9 Mass Loading implications in $3D$ simulation

Chapter 2 addressed the growth of $1D$ dust grain in presence of electrostatic and magnetostatic fields. Mass loading simulation showed more colliding ions at the grain's edges than at dust surface under the influence of a magnetic field in a direction parallel to the grain. Mass loading when magnetic field was oriented perpendicular to grain direction was unbalanced, where loading at one edge higher than the other which showed higher loading from the opposite direction. The simulation in $3D$ for ellipsoidal grain has some similarity in that a parallel magnetic field encourages mass loading at grain's ends, while prevents ions from reaching the grain's surface. $3D$ simulation showed much ellipsoidal growth than $1D$ case. Indicating that $3D$ simulation is required for accurate dust growth simulation in the presence of a magnetic field. The perpendicular magnetic field increase mass loading in one end more than the other end. However,

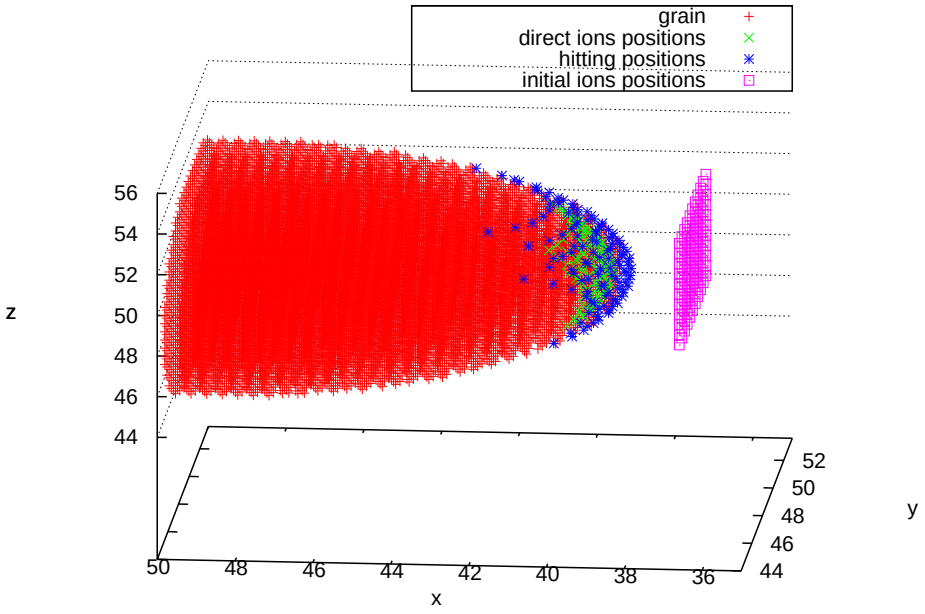

Figure 4.20: As Figure 4.17 but for a different ions batch. Ions from the the batch in front of grain's end tend to spread on the end.

overall, there was mass loading on the entire grain surface.

4.10 Conclusion

Numerical simulations in this chapter for the growth of an ellipsoidal grain in $3D$ under influence of electrostatic field arising from the charged grain and an applied uniform magnetic field oriented perpendicularly and parallel to the major axis of the grain , respectively, have been addressed. The significance of the presence of a magnetic field on the growth of dust grains was investigated via varying the parameter p . In an electrostatically dominated regime, there were more deposited ions on dust surface was than in the magnetically dominated case. The direction of the magnetic field also played an important role in ellipsoidal dust growth , encouraging grain ends growth

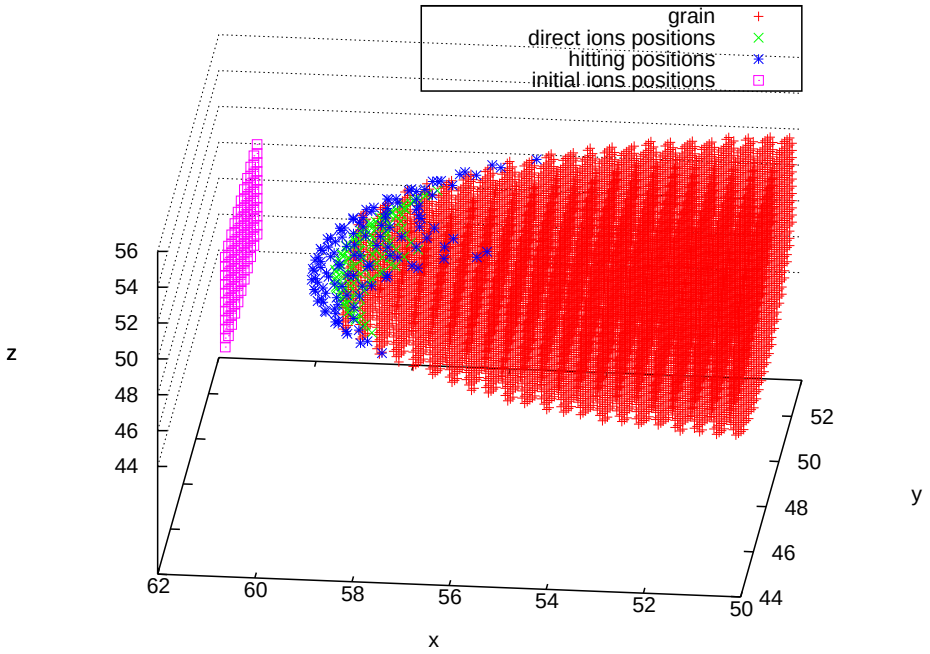

Figure 4.21: As the previous Figure but for the other end of the grain.

as well as giving rise to size growth when oriented parallel to the major axis of the dust grain. A perpendicular magnetic field permitted surface and ends grain growth in an asymmetrical manner. Simulations showed a significance of trapped ions on dust grain growth. While Stark (2008) research of elongated dust growth in astrophysical plasmas shows that the suggested growth process is an active tool providing the growth mechanism in the Supernova remnant, results in this chapter can assist to understand the the process of dust growth in magnetised plasma. In addition to be as an instrumental detection in the solar system to the presence of elliptical dust grains especially in magnetized regions, which can be tool in aligning the dust grains giving rising to the light polarization. Collisions between ions and neutrals, if involved in this simulation, could reduce the velocity of the ions and so making them subject to the field near the grain surface. Therefore, the ellipsoidal growth may increased. The question arising here is what the situation would be if this work is extended to consider multiple grain

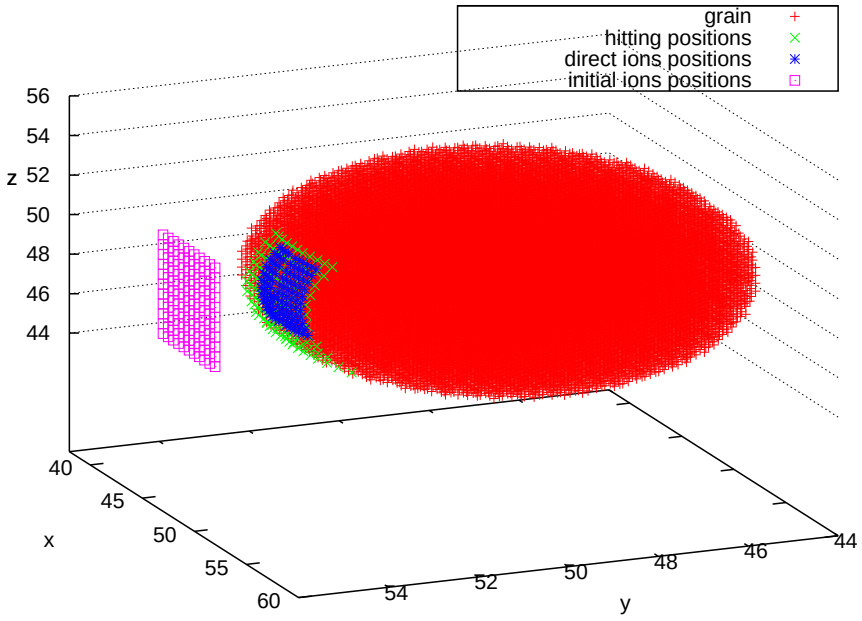

Figure 4.22: As Figure 4.17 but for a different ion batch. Ions here start their motion from the front of the grain's side. Ions hit the directed positions on the grain's surface and positions around it.

charging, where charged grains are in close proximity and what possible process could be initiated in such a situation. The next chapter investigates these questions.

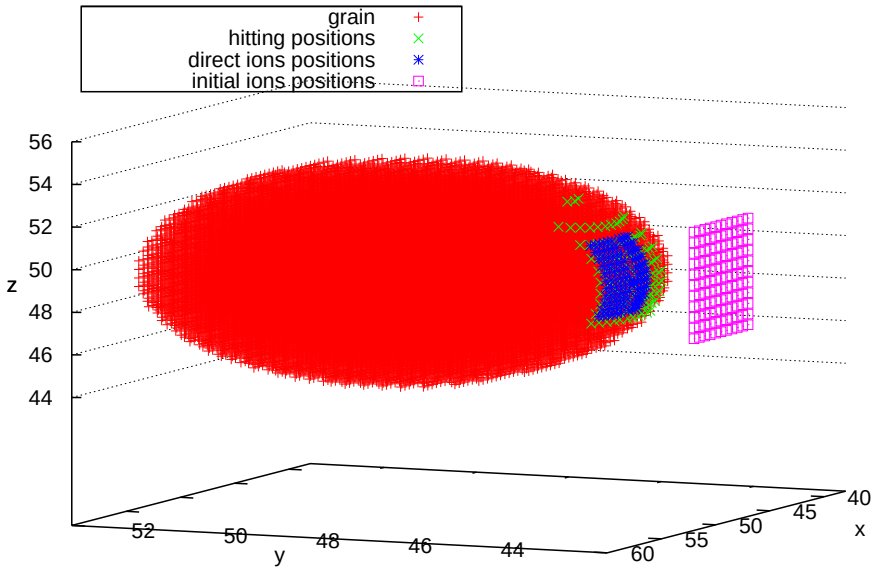

Figure 4.23: As the previous figure but ions start close to the other side of the grain.

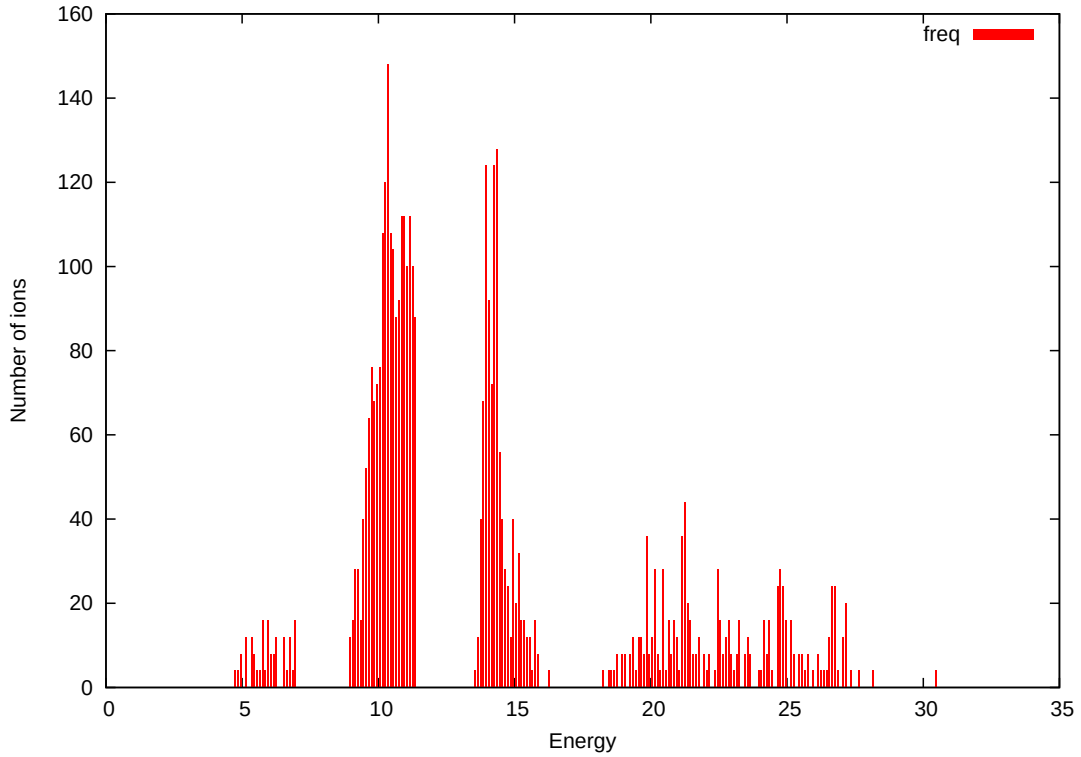

Figure 4.24: Frequency plot of energies of ions where the magnetic field is parallel to the x-axis. The presence of a discrete structure is evident. Explination for this is mentioned on p 100.

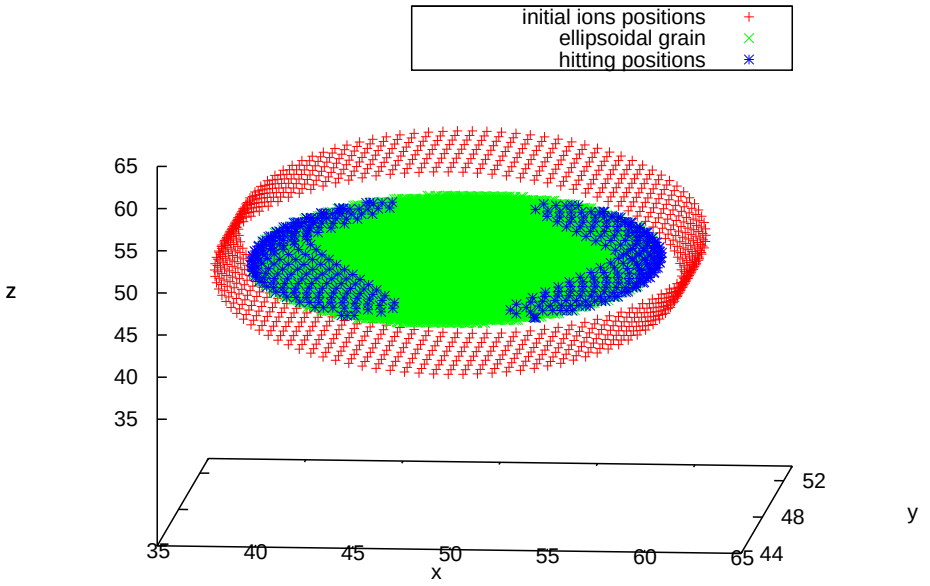

Figure 4.25: Figure represents the initial positions of ions, and the colliding positions due to the combined influence of the grain electrostatic field and the applied parallel magnetic field. Ions tend to hit the grain's ends.

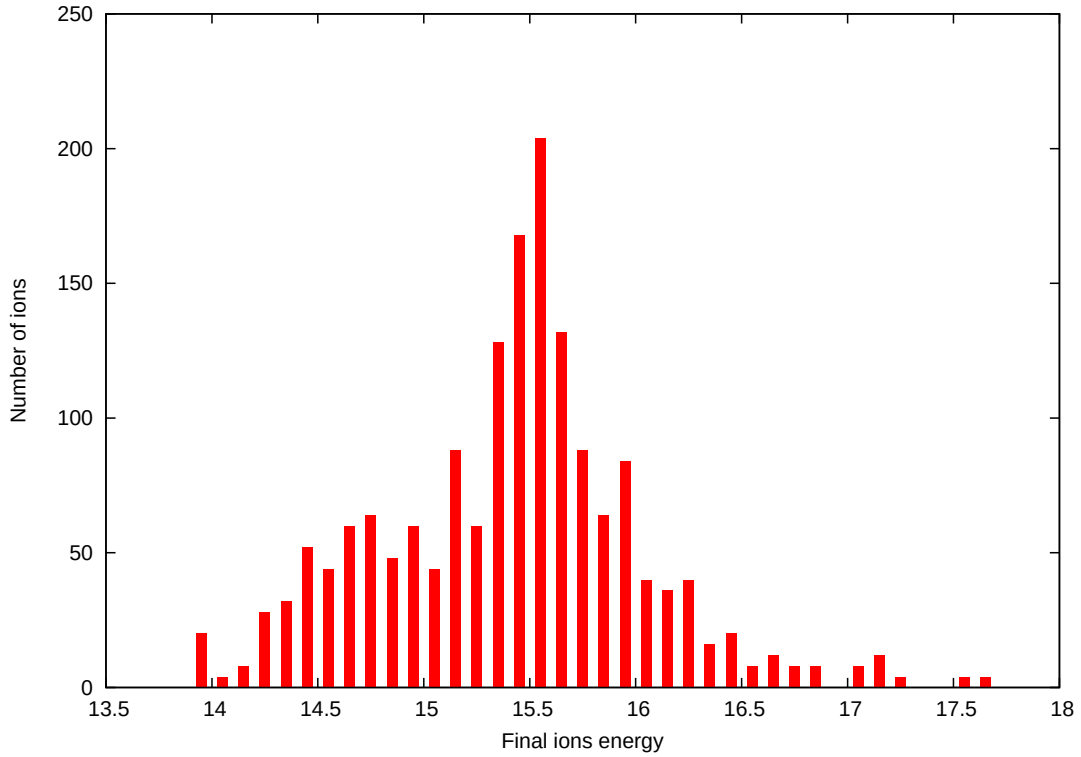

Figure 4.26: Frequency plot of energies of ions represented in the previous figure where the magnetic field is parallel to x-axis and ions were launched from circular bar from the grain. Figure shows a continuum energy distribution .

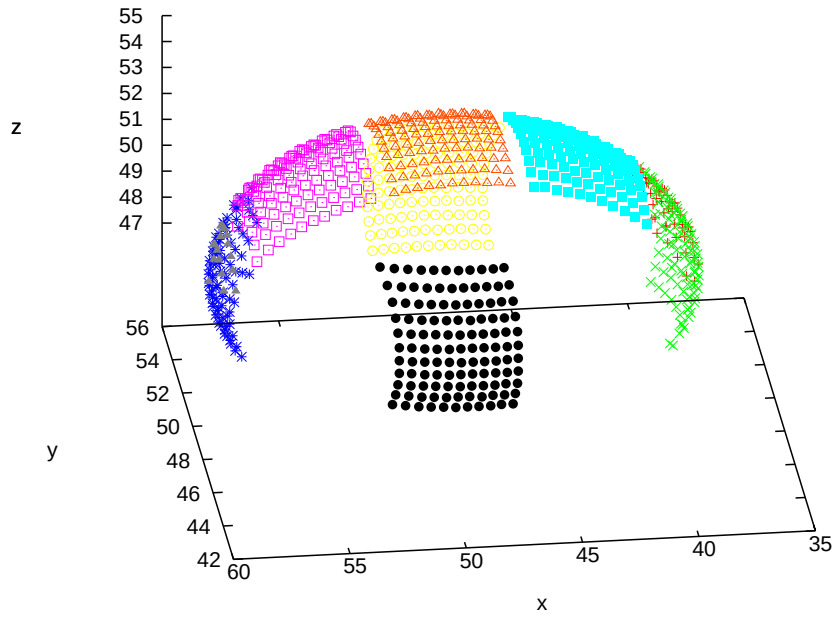

Figure 4.27: Coloured points represent ion density on grain surface. Each colour indicates ions belonging to the same batch. The grain's semi-axes a, b, c are $10, 5, 5$ in length, respectively. Ions' Larmor radius(R_L) at launch is comparable to the grain's semi-axes (b), where parameter $p = 8$ [$R_L/b \simeq 1$,$p = 0.1$], and the magnetic field is perpendicular to the x-axis.

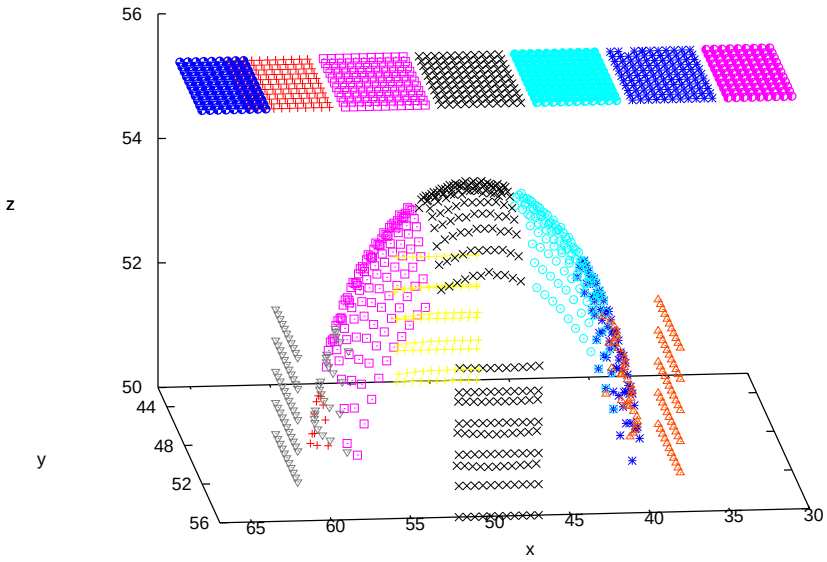

Figure 4.28: Coloured points represent ion density on grain surface. Each colour indicates ions belonging to the same batch. The grain's semi-axes a, b, c are$10, 5, 5$ in length, respectively. Ions' Larmor radius(R_L) at launch is comparable to the grain's semi-axes (b),where parameter $p = 8$ [$R_L/b \simeq 1$,$p = 0.1$],and the magnetic field is perpendicular to x-axis. Ions seem to hit their directed positions , however, some ions from batches further away tend to hit the grain's ends. This figure is similar to the previous one. However, here the original batches are added.

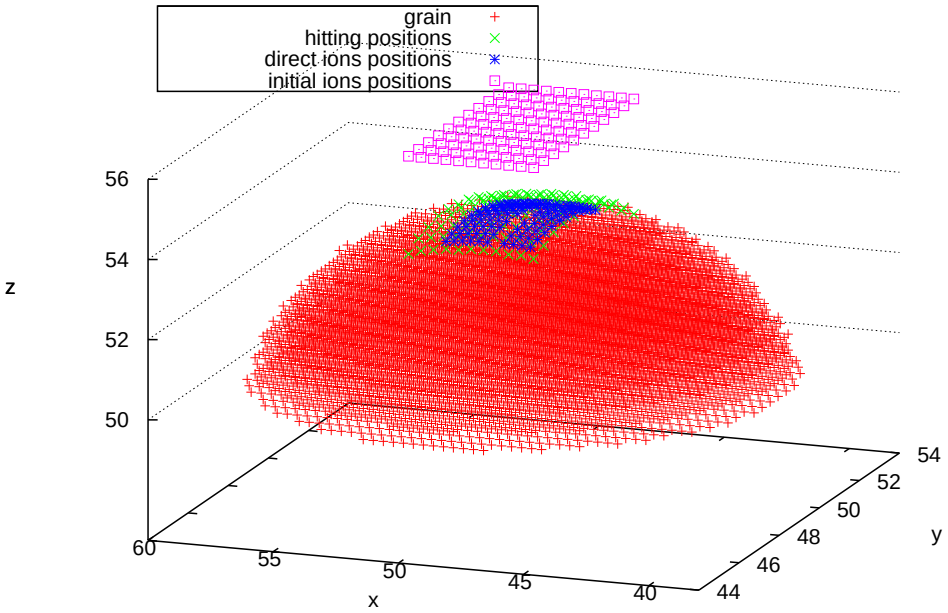

Figure 4.29: The initial positions of ion batch, the expected direct colliding positions in the absence of a magnetic field and the actual colliding positions due to the combined influence of the grain's electrostatic field and the applied magnetic field. Ions starting their motion near grain's surface tend to hit near their expected hitting positions.

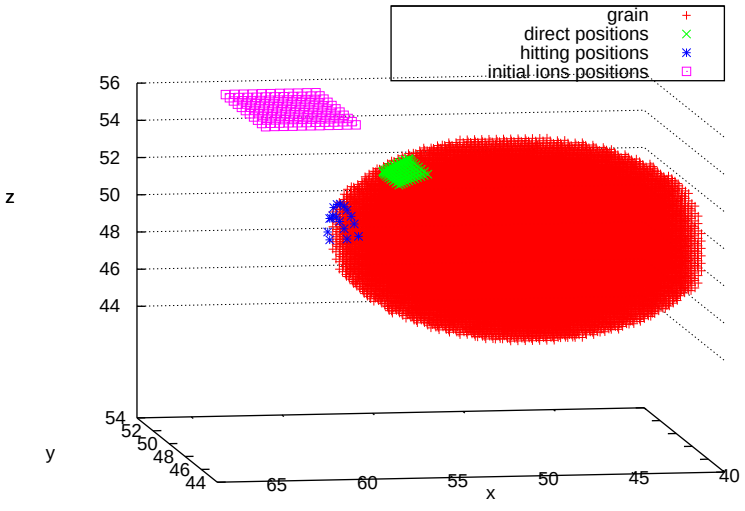

Figure 4.30: As Figure 4.29, but for a different ions batch. Some of the ions that start near the grain's end miss their expected hitting positions and shift toward the end, while the rest of ions miss.

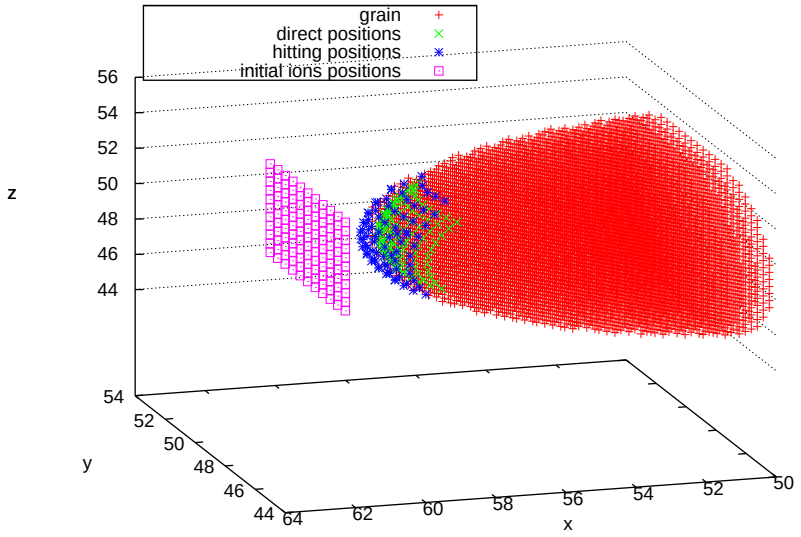

Figure 4.31: As Figure 4.29, but for a different ions batch. Ions close to the grain's corner hit near their expected positions.

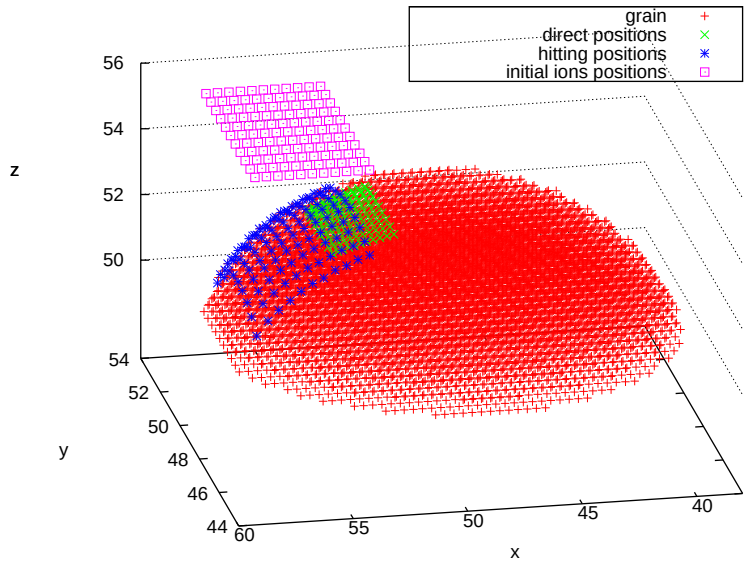

Figure 4.32: As Figure 4.29, but for a different ions batch. As ions start further from the grain's surface, their hitting positions shift toward the grain's end.

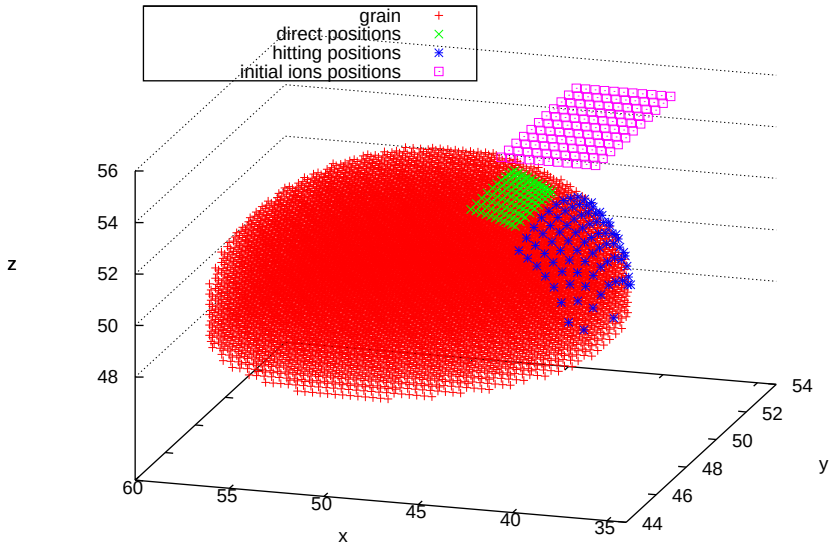

Figure 4.33: As Figure 4.32, but for a different ion batch.

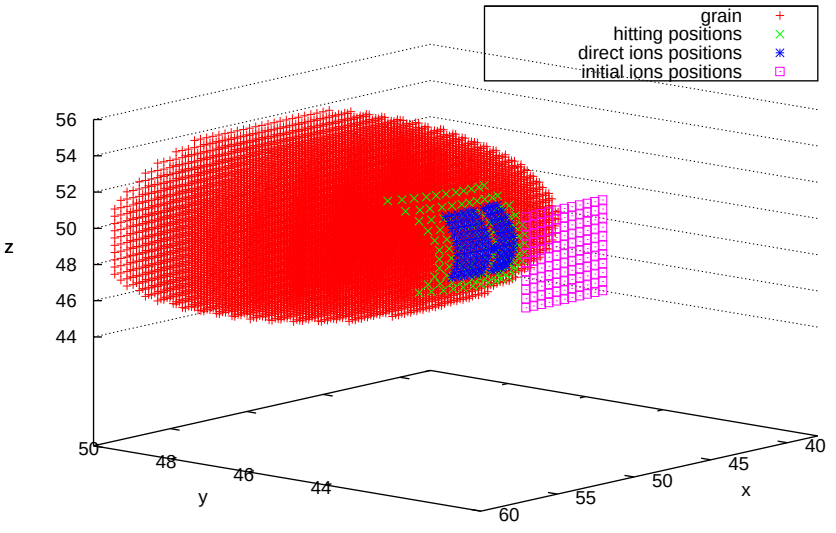

Figure 4.34: As Figure 4.29, but for a different ion batch. Ions that start close to the grain's end, tend to hit near the expected positions.

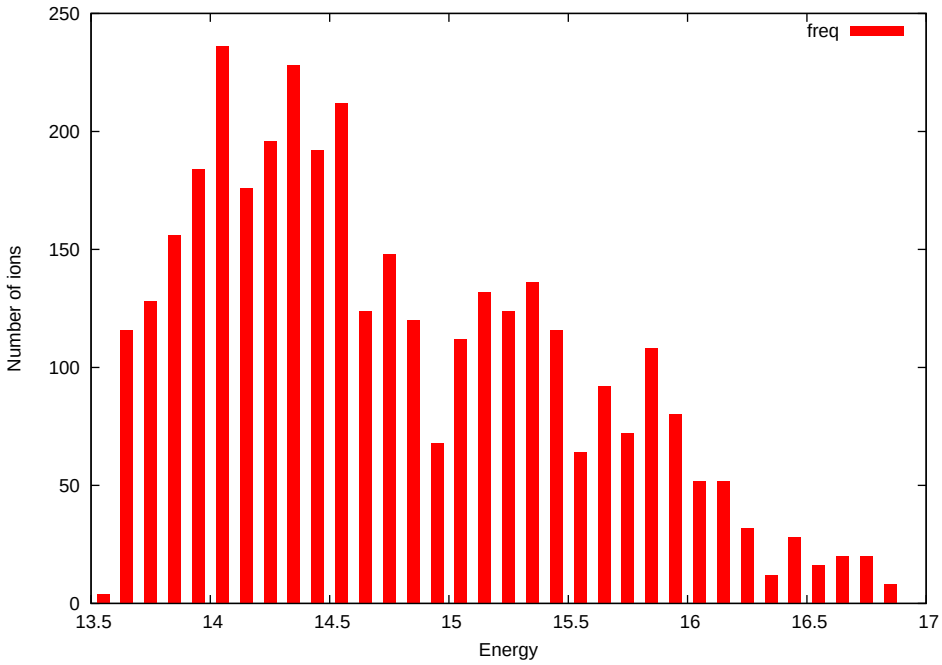

Figure 4.35: Frequency plot of energies of ions where the magnetic field is perpendicular to the x-axis. Figure shows a continuum energy distribution .

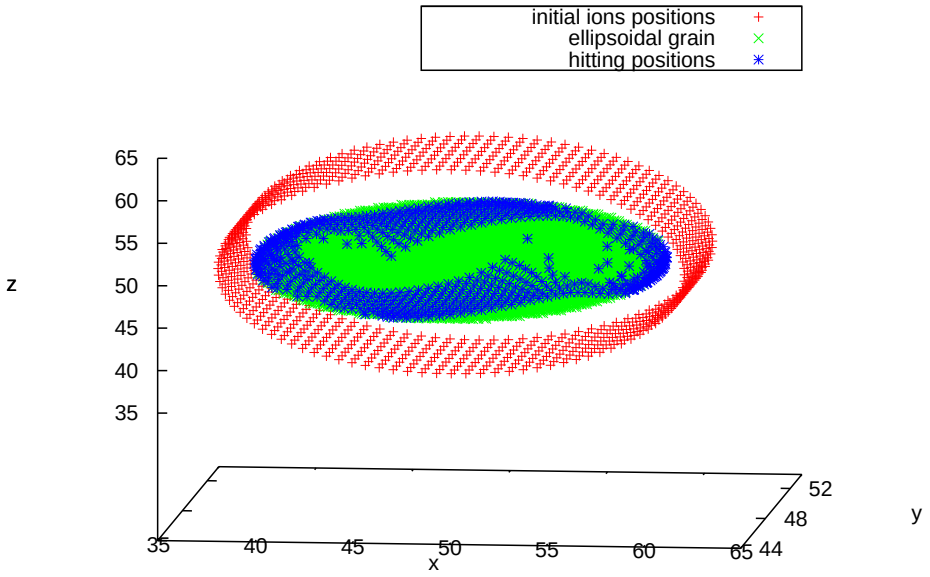

Figure 4.36: The initial positions of ions, and the colliding positions due to the combined influence of the grain's electrostatic field and the applied perpendicular magnetic field.

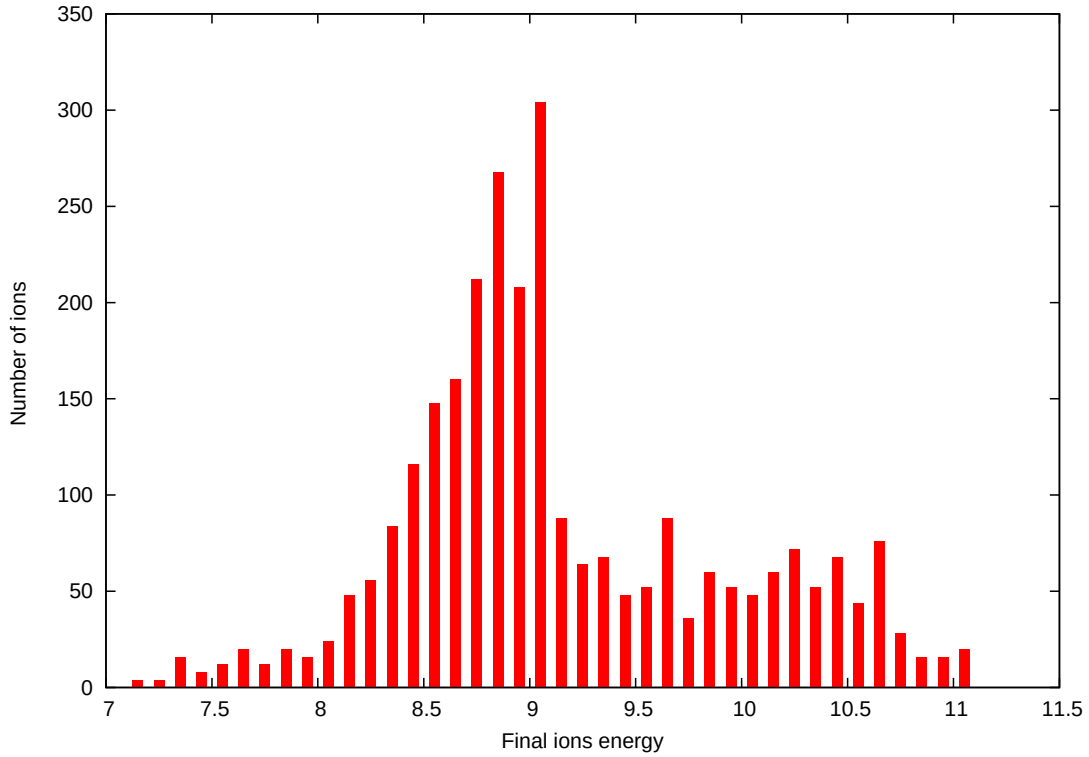

Figure 4.37: Frequency plot of energies of ions where the magnetic field is perpendicular to x-axis and ions are launched from a circular bar around the grain. The figure shows a continuum energy distribution .

5

Dust grains interactions in micro discharge scales

5.1 Introduction

In this chapter, a more extreme situation than microdischarge plasma, the recent attracted field, is investigated. Microdischarge plasmas are special case of electrical discharges that occur in geometries where one dimension at least is in the range of sub-millimetre length scales. However, small size charged dust grains may cause discharge for the neutral gas when dust gaps reach to sub-micro scales. An overview of microdischarge and its importance and implications is introduced. Our simulation model followed by results on charged dust interaction and its effect in the gas neutrals chemistry are presented.

5.2 Microdischarge plasma

Recently, microdischarge plasmas have attained much attention because of their significance in industrial applications. In addition, microdischarge plasmas helps to gain better understanding of processes that take place in small-scales configurations [Wilson

and Gianchandani (2001); Eijkel et al. (2000); Radmilović-Radjenović et al. (2005); Radmilovic-Radjenovic and Radjenovic (2007); Iza et al. (2008); Mariotti and Sankaran (2010a); Eichwald et al. (2011); Jeon et al. (2014)]. Although the microdischarges studies have started in 1990s, new applications have followed very quickly. As a result of their small physical dimensions, micro plasmas have unique features such as:

1. Confining the plasma to scales of 1*mm* or less is a good way to generate stable operation at atmospheric pressure. While low pressure plasmas need a large cost due to the vacuum system, operation at atmospheric pressure is cheaper and much favourable for industrial applications [Petrovi et al. (2007)].

2. Other properties make microplasmas desirable for different applications are non-Maxwellian electron energy distribution functions and high electron densities. Furthermore, the significant populations of energetic electrons (i.e.10 eV or higher) lead to non-thermal dissociation of molecular gases which results in high density of reactive radical species [Mariotti and Sankaran (2010b)].

3. As a consequence of their small size, microplasmas are used in etching or sputtering films locally to create microsize patterns directly without the use of photolithography [Mariotti and Sankaran (2010b)].

4. One advantage of using discharges in microscales is the low voltage and power required to produce a discharge. In addition, Nonthermal plasmas (a plasma that has species in thermal equilibrium only with similar mass species, and the velocity distribution of each specie can be represented by a Maxwell-Boltzmann distribution) are more favourable for materials collection because of the possibility of encouraging chemical reactions that may not be simple by thermal means. Also, low temperature processes permit temperature-sensitive materials to be evolved.

In general, these properties differentiate microplasmas from other high-pressure plasma sources such as arcs although arcs generate at atmospheric pressures makes

them similar to microdischarge. Otherwise, the electron temperature and the nonequilibrium properties of glow discharge are similar to those of microplasma [Radmilović-Radjenović and Radjenović (2007)].

Microdischarge is not only interesting because of its applications, but also because it is a good system to examine some electric discharge scaling laws, such as the known Paschen law, that expresses the dependence of the breakdown voltage on the pressure times the electrode gap. However, the failure of the Paschen law has been observed in small gaps [Mariotti and Sankaran (2010b); Go and Pohlman (2010); Klas et al. (2011)]. This departure from the Paschen law has been thought to be a result of electron field emission from the negative electrode in presence of the high electric field at small gap. To describe gas breakdown at all separation distances, the modified Paschen law has been introduced. At short gaps distances, the modified Paschen law shows approximately linear increase in the breakdown voltage then data curve follows the macroscale Paschen law. A numerous number of papers has revealed a departure from the Paschens law at small gaps [Boyle and Kisliuk (1955); Chen et al. (2006)]. However, only over the last few years the deviation from Paschen law has been understood and referred to the field emission effect [Radmilovi-Radjenovi and Radjenovi (2008); Torres and Dhariwal (1999)].

In this chapter, we will demonstrate through simulations that the small charged dust grains in plasma at small inter-grain distances can acquire sufficient number of charges that may lead to electrical discharge and may change the chemistry of the ambient neutral gas.

5.3 Model of dust interaction

In order to simulate dust interaction properly, typical dust grains properties such as dust size, density, plasma temperature, and plasma density have to be included. In table 6.1, some typical dust parameters are shown. Dust grains immersed in plasma can acquire such charge. For elliptical dust, if one suppose that the capacitance of the

dust is equivalent to that of a conductor of the same size, therefore, the net number of negative charges a grain can acquire can given by [Stark et al. (2006)]:

$$N = \left(\frac{4\pi\epsilon_0 k_B}{e^2} T_e \sqrt{a^2 - b^2 ln(\frac{m_i}{2\pi m_e})}\right) / ln\left(\frac{a + \sqrt{a^2 - b^2}}{a - \sqrt{a^2 - b^2}}\right) \tag{5.1}$$

One can use the electrostatic potential for a charged ellipsoidal conductor which is given by:

$$\phi = \frac{Ne}{8\pi\epsilon_0 \sqrt{a^2 - b^2}} ln\left(\frac{a + \sqrt{a^2 - b^2}}{a - \sqrt{a^2 - b^2}}\right) \tag{5.2}$$

where a and b can be the major and minor axes of the grain respectively and they were chosen to be in range of astrophysical grains.

In order to the dust can interact electrostatically with another charged dust grain, the distance between them must be $\sim d < L_s$, where L_s is the dust sheath L_s and it is equal to a few Debye length if consider an astrophysical environment, and d is the average distance between two adjusted grains and it can approximate as:

$$d = n_d^{\frac{-1}{3}} \tag{5.3}$$

where n_d is the dust density. When the potential difference of two adjusted grains is larger than the work function of material of one of them, then electrons can be emitted from dust surface of the higher work function:

$$(\phi_1 - \phi_2) > \omega_{f1} \tag{5.4}$$

where ω_{f1} is work function of the emitter dust surface. For these electrons to be collected by the other dust grain, they must gain energy enough to overcome its energy barrier $E_{barrier}$.

$$E_{barrier} = \omega_{f2} - e(\phi_1 - \phi_2) \tag{5.5}$$

where ω_{f2} is work function of the collector dust material.

Table 5.1: Some typical parameters of different dusty plasma regimes [Shukla and Mamun (2010)].

Plasma regimes	dust density(n_d/m^{-3})	Electron temperature ($T(K)$)	Electron density (n_e/m^{-3})	Dust radius(μm)
Interstellar plasma	10^{-6}	10^4	10^5	$2-10$
DC discharge	10^9-10^{10}	10^4	10^{16}	$1-5(Al_2O_3, 50-65(Silicate)$
Tokamak	10^4	10^8	10^{20}	$1-10?(Carbon)$

5.4 The model equations

The governing equations of grains interaction in plasma model are,

$$m\frac{d\mathbf{v}}{dt} = -q(\mathbf{E} + \mathbf{v} \times \mathbf{B}), \tag{5.6}$$

$$\nabla^2\phi = \frac{q}{\varepsilon_0}(n_+ - n_e), \tag{5.7}$$

$$\mathbf{E} = -\nabla\phi \tag{5.8}$$

These equations are the equation of motion, Poisson equation, and electric field, respectively. In order to carry out the numerical simulation, the model equations are required to be non dimensional. In chapter 2 the non dimensional treatment in addition to setting an appropriate parameters have been done. However, self potential of the charged particles have not been considered in the previous work (chapters 2 and 3). Therefore, the non dimensional form of Poisson equation and electric field are:

$$\hat{\nabla}^2\hat{\phi} = P_c(\hat{n_+} - \hat{n_e}), \tag{5.9}$$

$$\hat{E} = -P_d\hat{\nabla}\hat{\phi} \tag{5.10}$$

where the parameters in the non-dimensional equations are:

$$P_c = \frac{ql_0^2n_0}{\varepsilon_0\phi_0} \tag{5.11}$$

$$P_d = \frac{\phi_0}{E_0l_0} \tag{5.12}$$

For further simplicity, the following substitutions can be used;

$$n_0 = \frac{1}{l_0^3} \tag{5.13}$$

$$E_0 = \frac{\phi_0}{l_0} \tag{5.14}$$

$$\phi_0 = \frac{q}{\varepsilon_0 l_0} \tag{5.15}$$

therefore:

$$P_c = 1 \tag{5.16}$$

$$P_d = 1 \tag{5.17}$$

5.5 Numerical model

A Fortran95 code was written to show what happens to electrons when they become detached from the dust surface and move freely under the influence of the electric field. At the beginning of the simulation, an isolated charged dust grain is assigned a specific potential on its surface using the same techniques described in the previous chapter. The isolated charged grain has a set of potential contours that can be calculated with mean of Finite difference solver (details can be found in chapter 3). The distant plasma allowed to set the zero potential to the edge of the grid. Perhaps bringing a second charged grain close to the first one changes the surface electric field on both grains, possibly triggering field emission.

To investigate what happens to detached electrons from the dust surface and move freely under the influence of the electric field or combination of electric and magnetic field, modifications were implemented in the code which was used in chapter 3. In that code scheme, the equations that correspond to the charged particles motion and the electric field interpolation are solved. Here the total electric field is self field of charged dust in addition to field which contributed by the charged particles. To include the effect of electrons emission on gas breakdown, following parts were introduced to

the code: at the beginning of the modified simulation, the ejected electrons were accelerated by the high electric field and the particles new positions were calculated. The self-created field and, hence, the force acting on the particles will change. Therefore, at every time step weighting the positions of the particles to the nearest grid, yielding changing the charge densities on the mesh point. Then the potential and electric fields are updated on the grid points using finite difference solver. During collisions, energy was conserved. Gas molecules were assumed to be fixed in space. Electrons interact through their self field. To investigate the effect of magnetic field on energy acquired by the emitted electrons, and consequently on the gas breakdown, a uniform magnetic field will be applied. A background of molecular Oxygen at atmospheric pressure and a temperature of approximately room temperature ($300K$) is assumed. Other gases can be selected with appropriate cross sections. Secondary processes such as electron-ion recombination, photon emission and absorption were not taken into account in this simulation. Only the following collisions are taken in consideration attachment, metastable excitation ($O_2(a^1\Delta_g)$), metastable ionisation and ionization of neutral gas [Gudmundsson (2004)]. To simulate these collision processes for neutral gas in plasmas, the collision probability for every particle (electron) at each time step should be computed.

The probability of a particle having a collision is dependent on the relevant cross-sections. Inelastic collisions cross sections, such as collisions considered here, depend strongly on the energy of the electron moving through the gas and can be written as:

$$P_i = n_t \sum_{i=1}^{n} \sigma_i(\varepsilon)\upsilon\Delta t \tag{5.18}$$

where P_i is the probability of the collision , n_t is the number density of the target atoms, υ is the electron speed, σ_i is the value of the cross-sections summation at electron energy ε and Δt is the computational time steps.

The cross-sections of the desired collisions (attachment, metastable, and ionization) for electrons colliding with Oxygen melocules (O_2) are taken from Phelps database

(Phelps database, www.lxcat.net, retrieved on February 20, 2014)[Lawton and Phelps (2008)]. The metastable ionization collision is taken from Morgon database (Morgon database, www.lxcat.net, retrieved on February 20, 2014).The ionisation energy threshold of O_2 is 12.06 eV, the excitation threshold for the metastable is 0.97 eV and the energy threshold for ionisation of the metastable is 11.0 eV. Cross sections of electron attachment, metastable, ionization of metastable and ionization of ground state oxygen molecules are represented in Figures 5.1, and 5.2.

Given the energy of the incident electron the probability of a collision can be determined by selecting a random number. The collision is considered when the collision probability is higher than the random number. To determine the type of such collision, another random number is compared with the relative probability of every collision type to the probability of the collisions. During the collision the total energy ,included the kinetic energy plus the ionisation energy, is conserved. If ε_e is the energy of the ionising electron, and ε_i is the ionisation energy, then the equation expressing the ionizing electron energy during the collision can be written as:

$$\varepsilon_{post} = \varepsilon_e - \varepsilon_i \tag{5.19}$$

where ε_{post} is the energy remained post collision which can be shared between the two electrons by ratio determined again using a random number. However, since the incident electron has a significant energy in respect to the target and the possible produced ion, the latter have considered to be at rest during collision reflected the high mobility of electrons than ions and neutrals. The available energy post collision can be shared between the ionizing electron and the resulting electron only.

5.6 Initial conditions

A domain of $M \times N = 500 \times 500$ grids is used to simulate dust grains interactions. All domain boundaries set to have zero potential. Two adjusted grains in different orientations and different potentials were set within the domain with separation distance

between them d. The major to minor axes of the first and the second grains are: a:b 5 : 2 and 4 : 8 respectively. The gap size was in range of $120\mu m$ and this size is nearly 12 order of the grain size (which is $10\mu m$) and about 10^4 of the dust Debye length (which is about 10 m). The dust sheath L_s is equal to a few Debye length if consider an astrophysical environment. The dust grains acquire charge from the plasma, and when two such grains come into close contact, the potential difference (caused by geometrical effects mainly) could cause electron transfer from one to the other. The potential distribution in such model was evaluated using finite difference method in similar technique to the one described in Chapter 3. The motion of emitted electrons was derived via Rung-Kutta on equation of motion and acquired energies of electrons were calculated. Electrons energies can provide an initial guide to possibility of ionization, and excitation of neutrals.

The two grains were separated by distance d in a range of micrometers. Fig.5.3 shows electric potential of the two adjusted grains. The magnetic field was oriented along z-axis. The emitted electrons population consists of five hundreds electrons moving from rest. Table 5.2 summaries initial conditions used in this simulation.

5.7 Results

The emission of surplus electrons from charged dust grains in Oxygen plasma and their evolution in space between dust was calculated for several values of the parameter p, which describes the relative sizes of the electric and magnetic forces. Electrons-gas collisions were examined (including electron attachment, metastable, metastable ionization, and molecules ionization). Results with different values of p were discussed to represent some of the possible electrons process result in presence of dust in plasma. In each case, snapshots were taken at regular time intervals from the start until electrons hit the second grain . Snapshots were recorded for the parameters; electron density, metastable density, and ions density. In addition, electrons energy and self electrons potential at same intervals were presented. To simplicity, units of all these parameters

Table 5.2: Parameters used in numerical simulations.

Simulation property	Value
Domain dimensions	220×220
$x-, y-$boundaries	$\phi = 0$
Number of initial electrons	500
p	$10^2, 10^3$
$d\hat{t}$	0.1
ϕ_1	$-10V$
ϕ_2	$+10V$
d	$120\mu m$
$a : b(1^{st} grain)$	$5 : 2\mu m$
$a : b(2^{nd} grain)$	$4 : 8\mu m$

are dimensional.

5.7.1 [$p = 10^3$]

The case where $p = 10^3$ is presented in Figs.5.4-5.8. The evolution of electrons is faster than the following case (when $p = 10^2$). Electrons are drifted close to the second grain position. While the effect of the magnetic field (represented in an orbital motion) lead to bend the electrons (the upper set of electrons) trajectories in the lower electric field region, this effect is nearly trivial in the highest electric field region (the region between the grains), where the drift motion leads to move the electrons (the bottom set) toward the second grain directly. Electrons self field is not changing noticeably as a result of the small change in the electrons density as shown in Figs. 5.7 and 5.5 for the electrons self field and electrons density, respectively. The small change in the electron density is a consequence of the high effect of drift motion which leads to directing the electrons toward the second grain.

Fig.5.6 shows metastables collisions positions where metastables are expected to

form. Comparing this plot with Fig. 5.4, white spaces in between metastables positions in Fig.5.6 and minimum energy regions in Fig.5.4 can be seen. These regions of minimum energy (black regions) correspond to metastables formation collisions positions. Electrons gain energy over the metastable collision threshold (0.97 eV) then lose this energy in metastable production.

It can be seen from Fig.5.8 different histograms showing the number of electrons that acquire specific energy at some time intervals. Most electrons gain energy lower than metastable collisions energy and only small number of electrons exceed metastable collision threshold. However, electrons will lose their energy in a metastable collision before they start to acquiring enough energy for a new collision.

Because of the lower energy required for metastable collision, it can be seen as the dominant collision in this case and electrons do not have the chance to gain energy high enough to exceed other collisions process such as attachment and ionization. However, electrons may reach to higher energy leading to discharge of the neutral gas if the simulation extend to contain enough number of charged dust. Therefore, a simulation with reasonable number of charged dust grains may be required.

5.7.2 [$p = 10^2$]

For this case, $p = 10^2$, the motion of electrons in a direction perpendicular to the magnetic field is inhibited. Electrons orbit the magnetic field lines. Figs.5.9-5.13 represent the evolution of electrons trajectories, electrons density, electric potential, and electrons energy at some time intervals for this case. Fig.5.9 shows an evolution of one electron de-attached from the first grain associated with its energy which is represented in colors. The electron orbits the magnetic field lines which is directed to the z-axis and drifts slowly toward the second grain position. It is noticed that the orbital motion is lower at the region between grains as a results of increasing the electric potential in that region.

Electrons self field is decreased slightly as shown in Fig.5.12 as a consequence of

electron density decreasing as can be seen in Fig. 5.10.

Fig.5.11 shows the metastables production positions plotted in red color in the region between grains. The empty regions represent where electrons start to gain energy before losing it in other metastable formation collisions.

The energy that electrons gain in some time intervals is showing in Fig.5.13. Histograms imply that a number of electrons that exceed the metastable collision energy is low at the selected times. However, the high number of metastables represented in Fig.5.11 indicates that most of the selected intervals represent electrons energy just after or between metastable collisions. The lower gained energy positions in Fig.5.9 may show where the metastables collisions take place.

5.7.3 Comparison

Electrons in the case when $p = 10^3$ accelerate as they drift with electric field lines gaining maximum energy at the closest region to the second grain. Fig.5.4 shows electrons energy of this case presented in colors. Electrons in case $p = 10^2$ start to gain energy since they move parallel to the electric field of the emitter grain. The orbital motion of electrons around magnetic field lines causes electrons energy to fluctuate as can be seen in Fig.5.9. When electrons travel a quarter of the cyclotron orbit, they move with electric field direction of the emitter grain, hence start to gain energy. Then in the following quarter of the orbit, electrons move perpendicularly to the electric field lines, therefore, they keep their acquired energy. In the second half of gyromotion, electrons travel against electric field lines results in decelerate them particularly when electrons move close the grain region. That results in the reduction of the energy acquired by the electrons. These fluctuations in energy do not give the electrons the chance to gain enough energy to make more collisions. Therefore, the metastable number in this case is less than the previous one. In both cases electrons energy does not exceed metastable collision threshold. Although the increase of the electric field causes increasing in the metastable production in the case ($p = 10^3$), case ($p = 10^2$) spreads out the electrons

and metastables in a larger distance in the domain. That may have an effect when a large number of charged dust and electrons is present.

5.8 Conclusion

Microdischarge plasmas is a special case of electrical discharges which occurs in geometries where one dimension at least is in range of sub-millimetre length scales. However, in this chapter a much extreme situation than microdischarge plasma where small size charged dust grains may cause discharge for the neutral gas when dust gaps reach to sub-micro scales was investigated. The importance of the magnetic field was explored by varying the parameter p which gives the relative size of the electric field to the magnetic field. The distribution of electrons kinetic energies was investigated in two cases when ($p = 10^3$) and ($p = 10^2$). In the first case the gained energy increased dramatically, however, the gained energy did not exceed further than the metastables threshold as a result of consuming electrons energy in metastable collisions. When magnetic field is increased ($p = 10^2$), gained energy is fluctuated as a result of contribution in gyromotion orbits. Therefore, a number of metastable in this case is lower than ($p = 10^3$) case. The presence of the magnetic field can help electrons to persist for longer and this gives electrons higher chance to involve in extra collisions.

The presence of he charged dust grains in plasma can activate the neutral gas in a non-thermal way. The metastable population is an important key in determining the required breakdown voltage as well as they can be a source of photons. The metastables have longer lifetime than the excited state. In addition, the metastables can be ionised by electrons with a lower energy than the ground state neutral. Therefore, the required electric field for breakdown becomes lower.

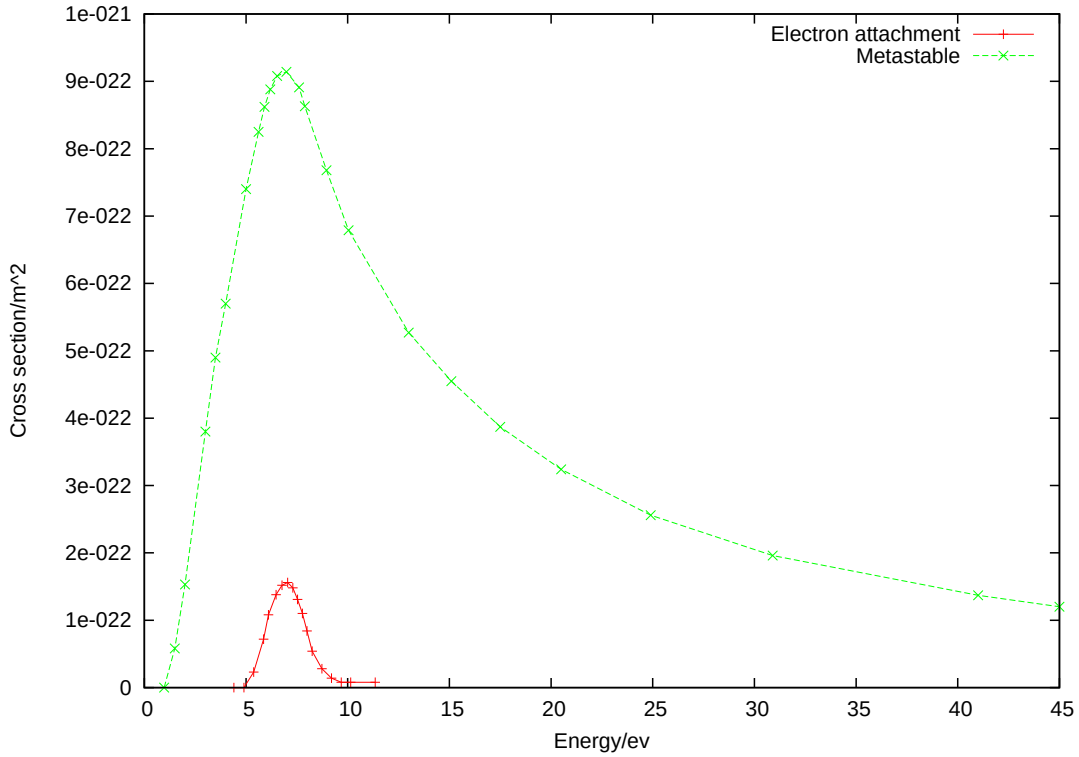

Figure 5.1: Electron attachment and metastable cross sections for molecular Oxygen [Lawton and Phelps (2008)].

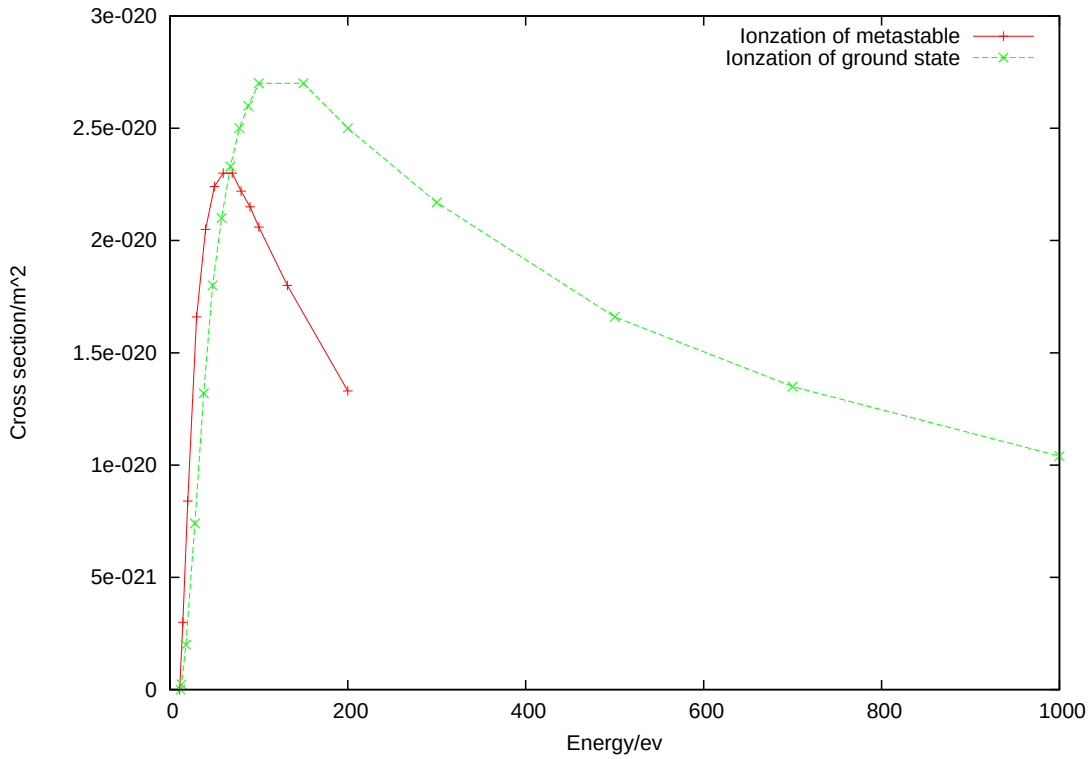

Figure 5.2: Metastable ionization and ground state ionization cross sections for molecular Oxygen (Morgon database, www.lxcat.net, retrieved on February 20, 2014).

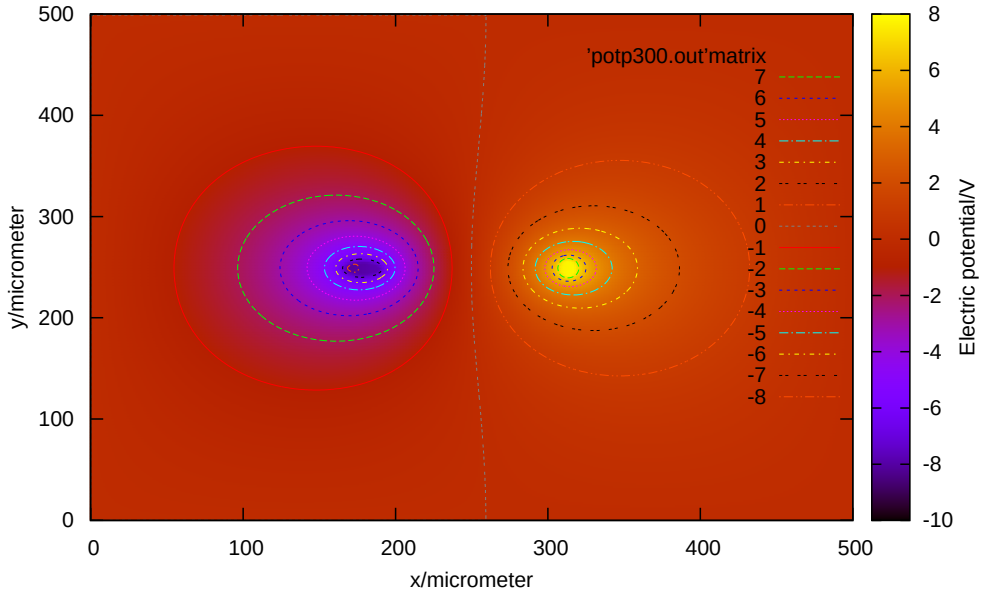

Figure 5.3: Plot of electric potential when two grains approaching each other to a gap distance equivalent to $d = 120\mu m$. The dust at left has potential corresponding to $\hat{\phi} = -10V$, its size is $a : b = 5 : 2$. The right dust has potential corresponding to $\hat{\phi} = 10V$, its size is $a : b = 4 : 8$ Contour lines show the change in the electric potential distribution of both grains.

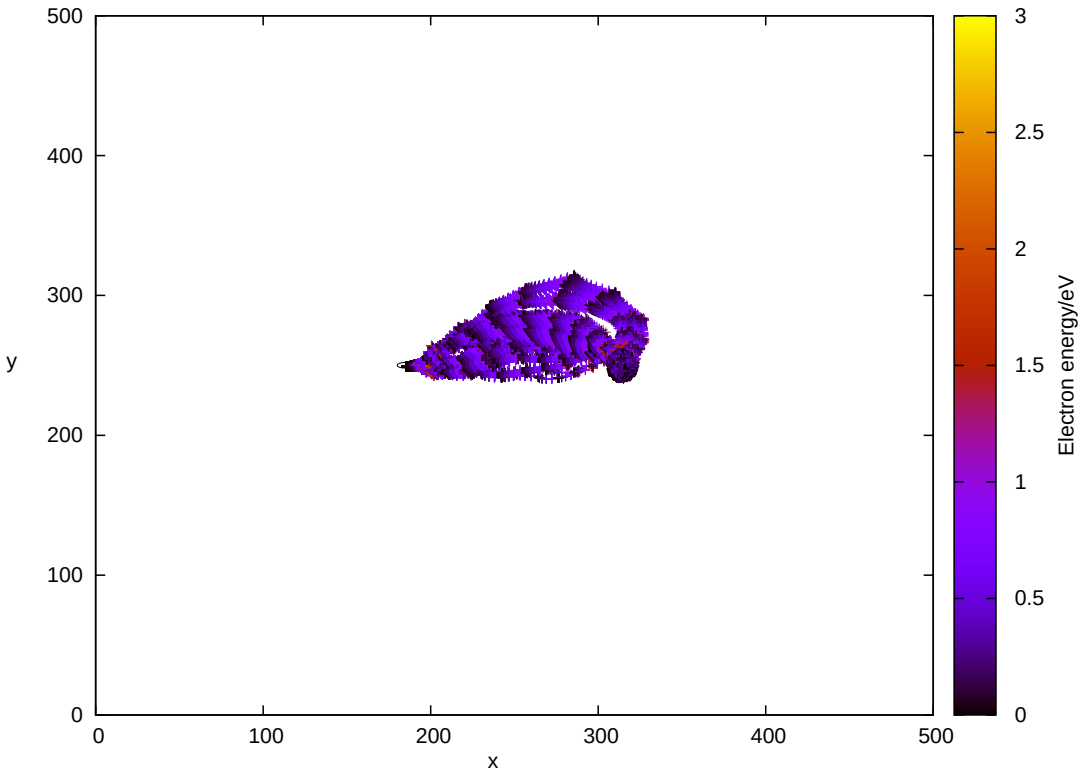

Figure 5.4: Plot shows the evolution of electrons trajectories at $p = 10^3$. Electrons started from the first grain at left toward the second one at right (showed as a small ellipse). Colors represent the electrons energy in eV. Dark regions represent metastables formation when electrons lose their energy.

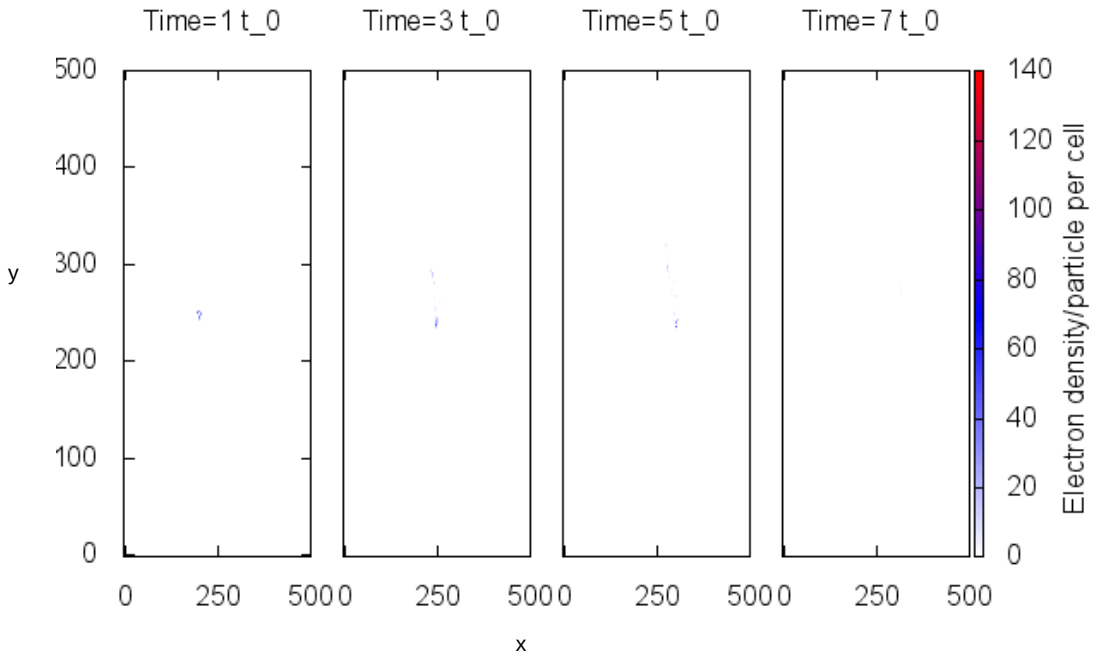

Figure 5.5: Snapshots for the electrons density evolution when $p = 10^3$ at some time intervals.

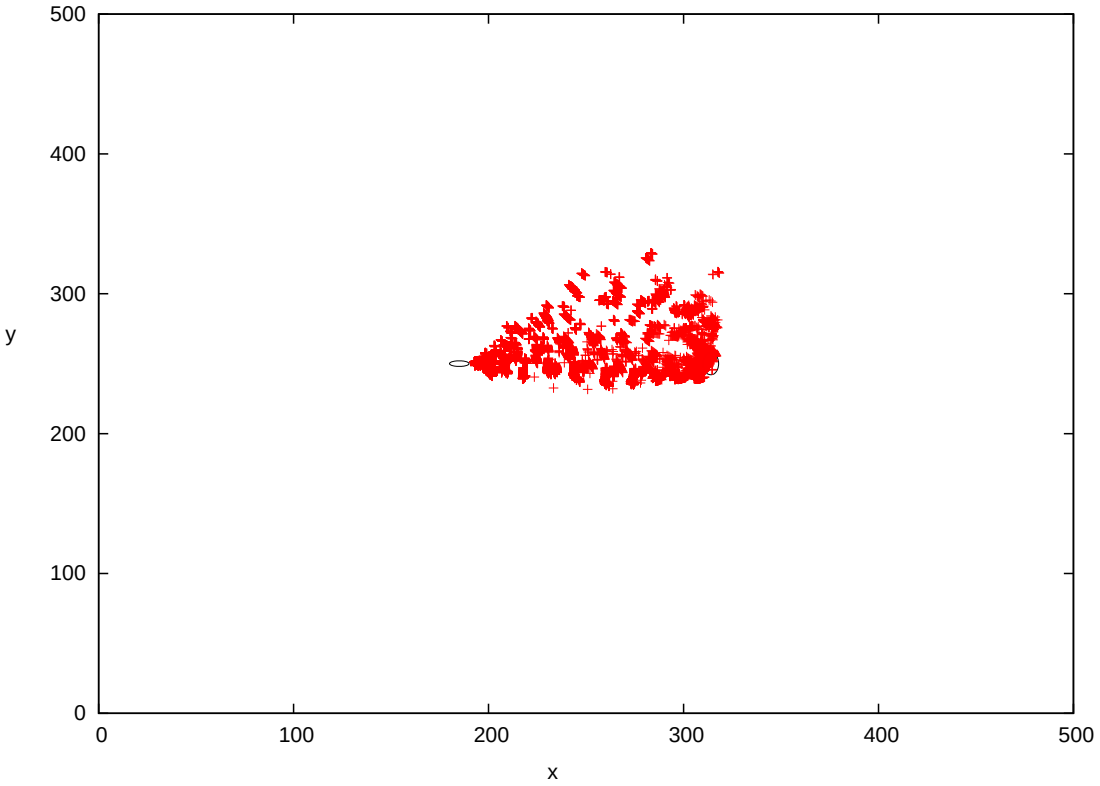

Figure 5.6: Plot shows metastables formation positions when $p = 10^3$.

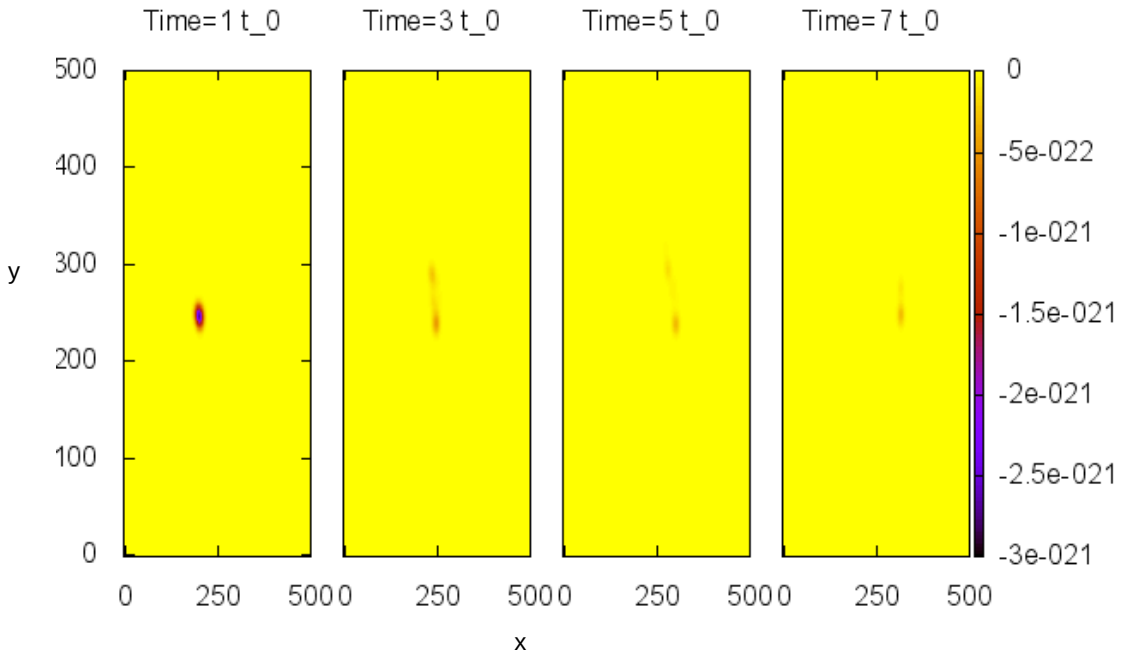

Figure 5.7: Snapshots for self potential of the electrons when $p = 10^3$ at some selected time intervals.

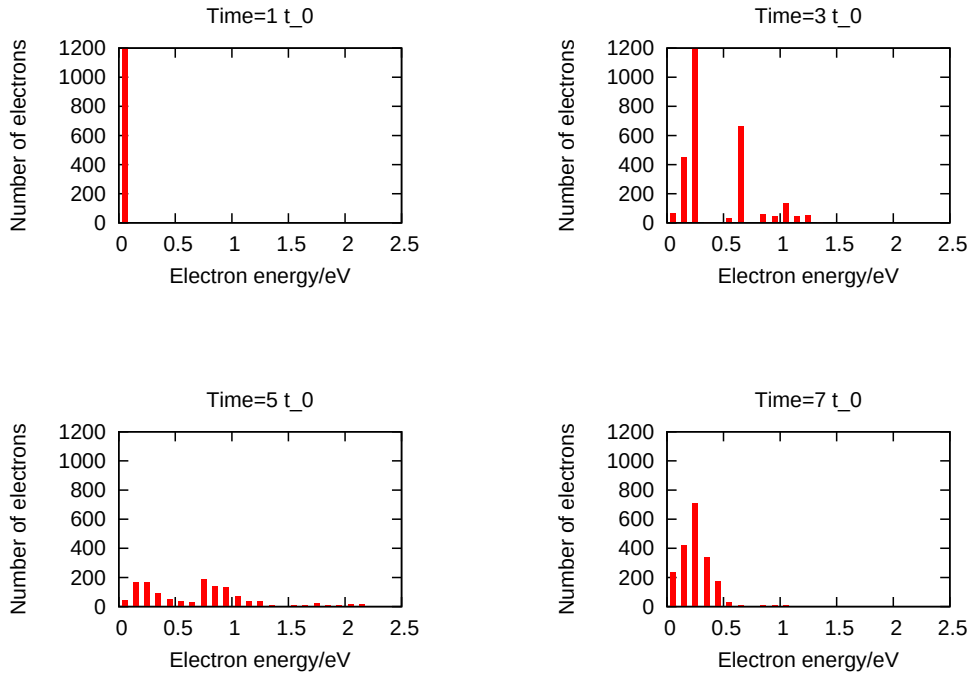

Figure 5.8: Histogram for the electrons gained energy evolution when $p_a = 10^3$ at some time intervals.

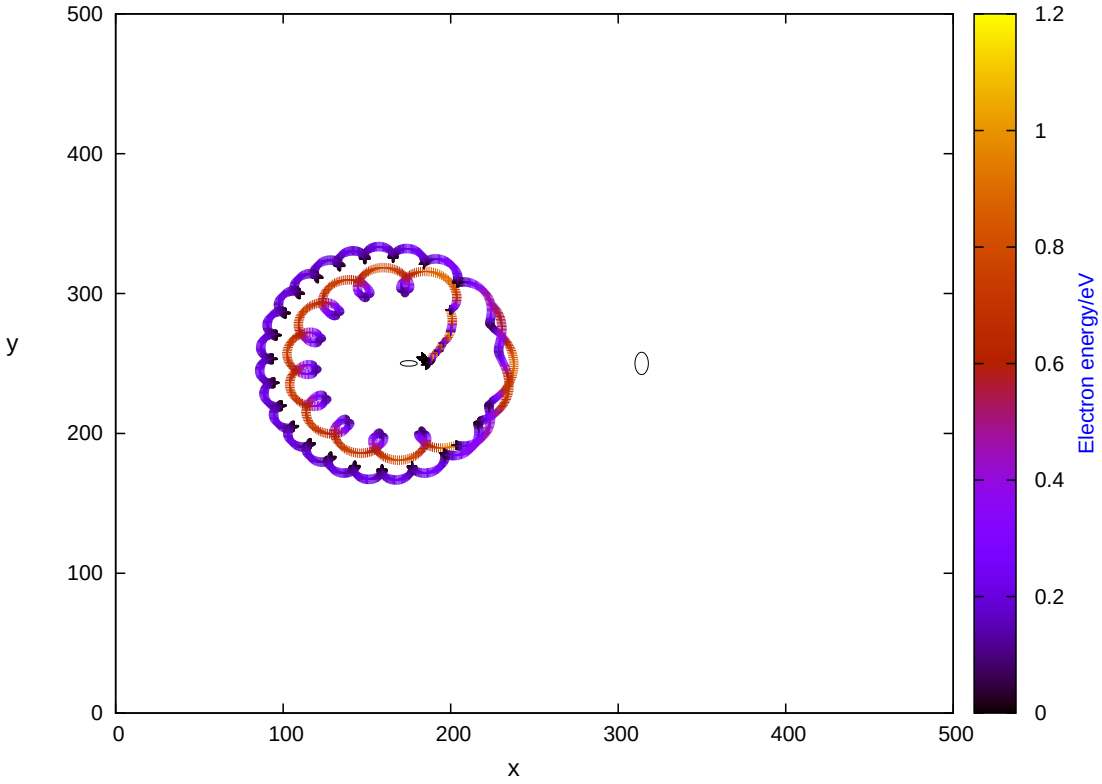

Figure 5.9: Plot shows the evolution of one selected electron at $p_a = 10^2$. The electron started from the first grain at left and then evolved in an orbital motion around the magnetic field lines and drifting motion around the first grain.

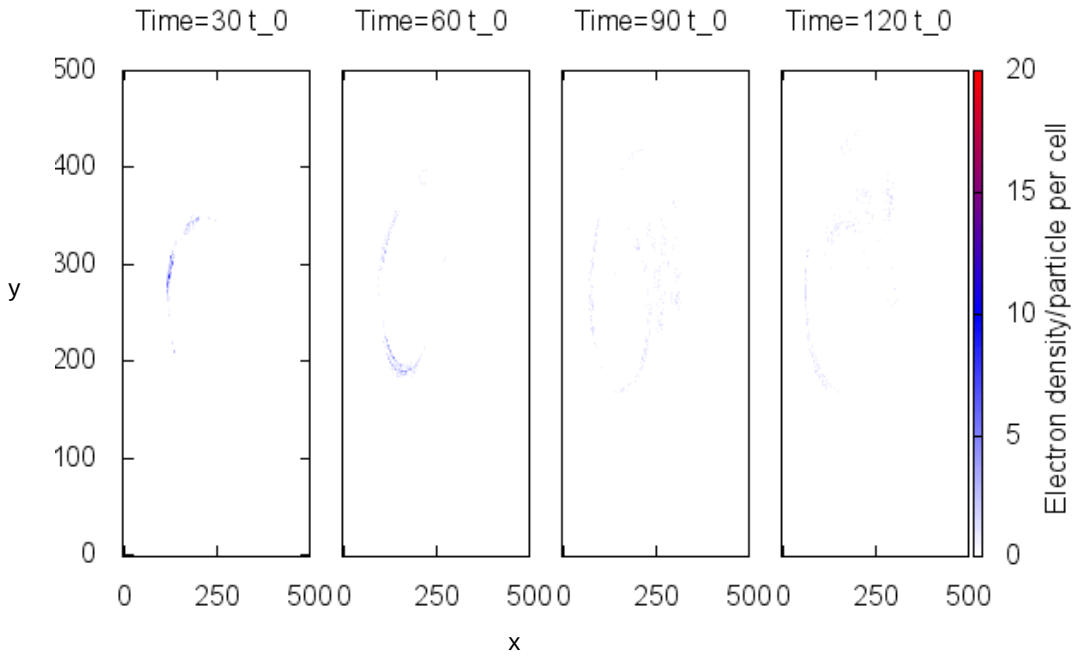

Figure 5.10: Snapshots for the electrons density evolution when $p = 10^2$ at some time intervals.

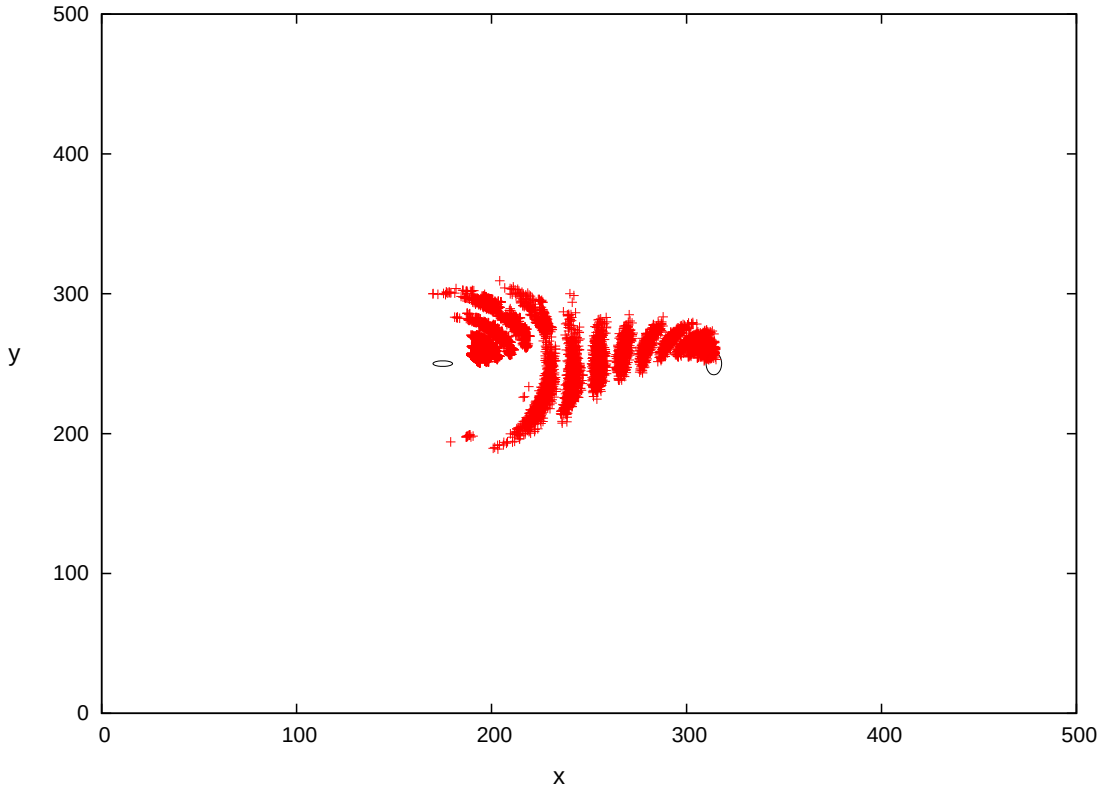

Figure 5.11: Plot shows metastables formation positions when $p = 10^2$ at some time intervals.

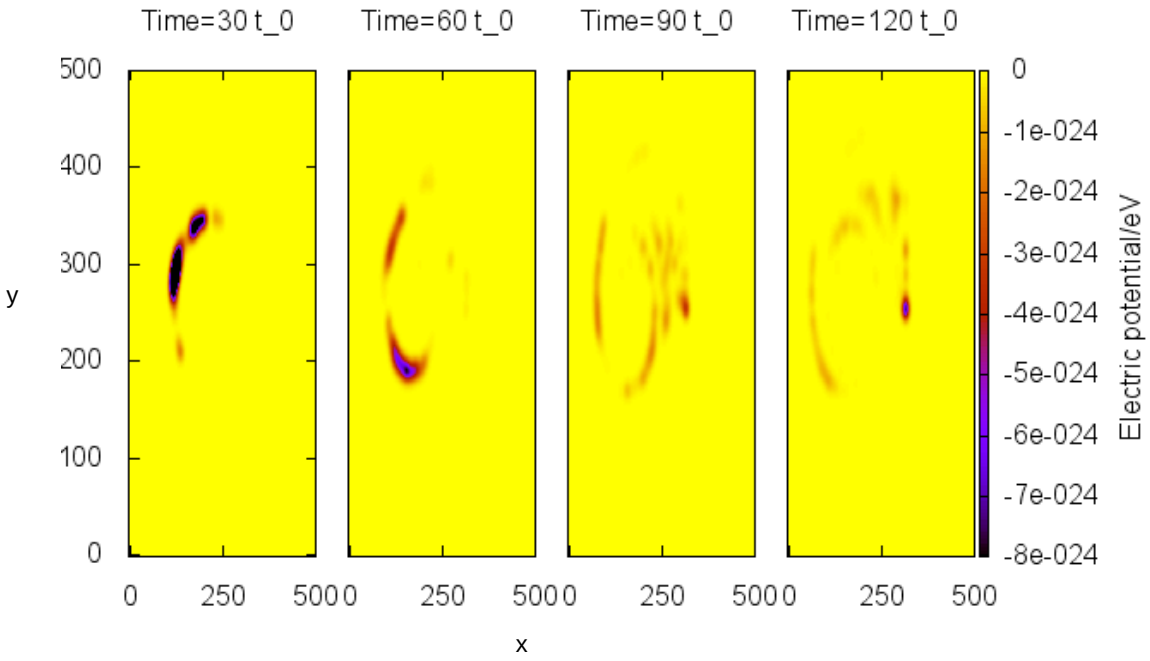

Figure 5.12: Snapshots for self electrons potential when $p = 10^2$ at some selected time intervals.

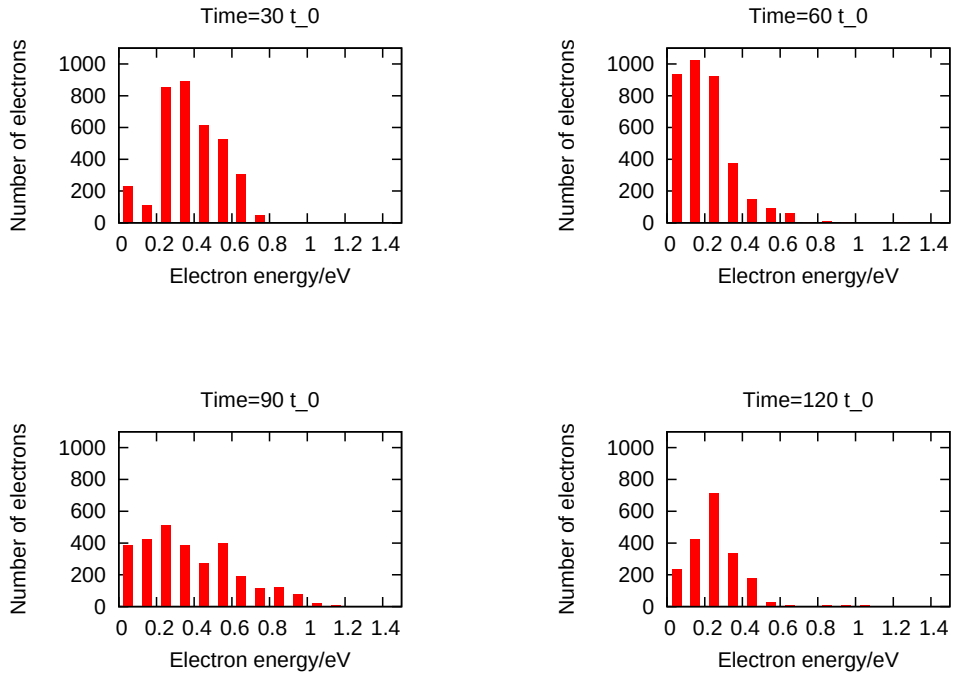

Figure 5.13: Histogram for the electrons gained energy evolution when $p = 10^2$ at some time intervals.

6

The collective dust grains interaction above thundercloud

Luminous relativistic electron beams inside thunderclouds have attracted scientists attention in recent years [Dwyer (2010); Füllekrug et al. (2013b); Cohen et al. (2010); Dwyer et al. (2008)]. They have been noticed via remote sensing radio waves of low frequency in a range of $\sim 40-400\ kHz$. These electron beams appear $\sim 2-9\ ms$ after positive cloud-to-ground lightning discharges at altitudes of between $\sim\ 22-72\ km$ above thunderclouds [Füllekrug et al. (2011b)].

Electron beams above thunderclouds are thought to be initiated by cosmic ray showers which are associated with intense lightning discharges [Füllekrug et al. (2011a)]. Cosmic rays which enter the Earths atmosphere with an energy of about $\sim\ 10^{16}\ eV$ [Gurevich and Zybin (2005)] lead to the emission of electrons from air molecules. The resulting electrons are accelerated by the strong electric field existing above $284\ kV/m\times n$, where n is the density of air relative to that at sea level, following an intense lightning discharge. Such electrons can produce secondary electrons by collisions with gas constituents. These secondary electrons can also acquire energy from the electric field leading to an avalanche of runaway electrons. While the process proceeds, the avalanche grows exponentially with time and distance resulting in a gas break-

down [Babich et al. (2004); Dreicer (1960); Chanrion and Neubert (2010)]. The primary electrons can reach relativistic energies with a mean energy of $\sim 7\ MeV$ [Füllekrug et al. (2011b)] and move upwards with a charge of $\sim -10\ mC$ and a current of $\sim 3 \times 10^{-3}\ Am^{-2}$ directed downwards. The seed particles must have a population above the runaway threshold of $\sim 10\ keV$ or more, depending on the strength of the electric field [Gurevich and Zybin (2005); Ebert et al. (2010)].

It was suggested that the fast removal of charges ($\sim ms$) from thunderclouds through lightning can also initiate sprites. Sprites are physical process observed in the mesosphere and lower ionosphere at altitudes about $40 - 100\ km$ [Dowds et al. (2003a); Barrington-Leigh et al. (2001)]. The cause of sprites formation is the strong electric field initiated in the lower ionosphere as a result of the fast charge removal from thunderclouds. The accelerated electrons ionize and excite the ambient neutral particles during collision, which leads to a discharge [Hiraki and Fukunishi (2006)]. This discharges can consist of thousands of growing channels which have diameters of the order of tens to hundreds of meters [Ebert et al. (2010)].

6.1 Role of charged dust in electron beam formation

The special electrostatic field configuration in a hollow cathode pulsed discharges efficiently assists beam electrons acceleration [Baker et al. (2007)]. It is suggested that a similar physical configuration might occur above thunderclouds in the presence of aerosols [Füllekrug et al. (2013a)]. The free electrons produced through lightning discharge attach to the aerosols and produce a quasi-static electric field. This electric field represents the geometric design and the physical properties of the environment above the thundercloud.

Recent observations regarding stratosphere layers which are possibly charged [Renard et al. (2010)] have shown the presence of charged aerosols which supports the suggestion that these stratospheric aerosols could be involved in the formation of relativistic electron beams above the thunderclouds, a process initiated by the lightning

discharges. It is likely that the convective updrafts in the convective storm assist in transporting the dust upwards into the troposphere. Furthermore, an ensemble of ice particles was detected at $\sim 13-14$ *km* height by CALIPSO [Helling et al. (2013)]. The alignment and orientation of such dust could be proven in a similar scenario with ice crystals in the electric field regions of thunderstorms [Saunders and Rimmer (1999); Ulanowski et al. (2007)].

These accumulated ice particles above the thundercloud may have helped produce a special electrostatic configuration which assisted electron beam formation. The following section presents more details about the formation of electron beams and the role of the dust.

6.2 Physical model for electron beam initiation

The role of charged dust in electron beam formation can be expressed as follows [Füllekrug et al. (2013b)] (see Fig 6.1): when a large thundercloud has exceeded the electrons near its upper surface, the region under the bottom surface of the cloud becomes positively charged. As a result of losing electrons through strikes from the thundercloud, electrons tend to gather at the top side of the cloud. By gaining extra electrons on the cloud surface, the electric field becomes large; consequently, electrons are launched to the region above the cloud. These electrons may cause the gas ionization of molecules, however their energies vary depending on the initial parameters. The resulting free electrons attach to the present dust population above the thundercloud and positive tails of ions are created to act as a seed for the electric field in a radial direction, paving the way for the creation of another acceleration of electrons starting from the top of the thundercloud and directed upwards. Then, the ions columns that were created from the previous event assist in acceleration the electrons and charged dust and help to guide these accelerated electrons and to dislodge them from the top of the cloud. As a result, more energetic and beamed electrons are produced. As was mentioned before, the configuration that causes these subsequent events is close to a

hollow-cathode discharge [Mavrodineanu (1984); Lidsky et al. (2004)] (see Fig. 6.2 where a cathode-shaped configuration, which is analogous to negatively charged dust, and outside anode ,which is similar to the positive ions tail produced from the previous event, cause a strong electron beam.

In this chapter, a simulation of such an environment above the thundercloud is presented, setting up suitable initial conditions including the presence of charged dust, and showing their role in simulating the subsequent electron beam in a second event.

6.3 Numerical model

The simulation model of electron beam formation used in this study is the particle model which has been discussed in detail in previous chapters (see chapters 2, and 3). However, no collision processes are included here.

Calculations have been made with fixed background potential and zero potential boundaries.

6.4 Governing equations

The model equations used to simulate the formation of electron beam are:

$$m\frac{dv}{dt} = -qE, \tag{6.1}$$

$$\frac{dx}{dt} = v, \tag{6.2}$$

$$\nabla^2\phi = \frac{q}{\varepsilon_0}(n_+ - n_e), \tag{6.3}$$

$$E = -\nabla\phi \tag{6.4}$$

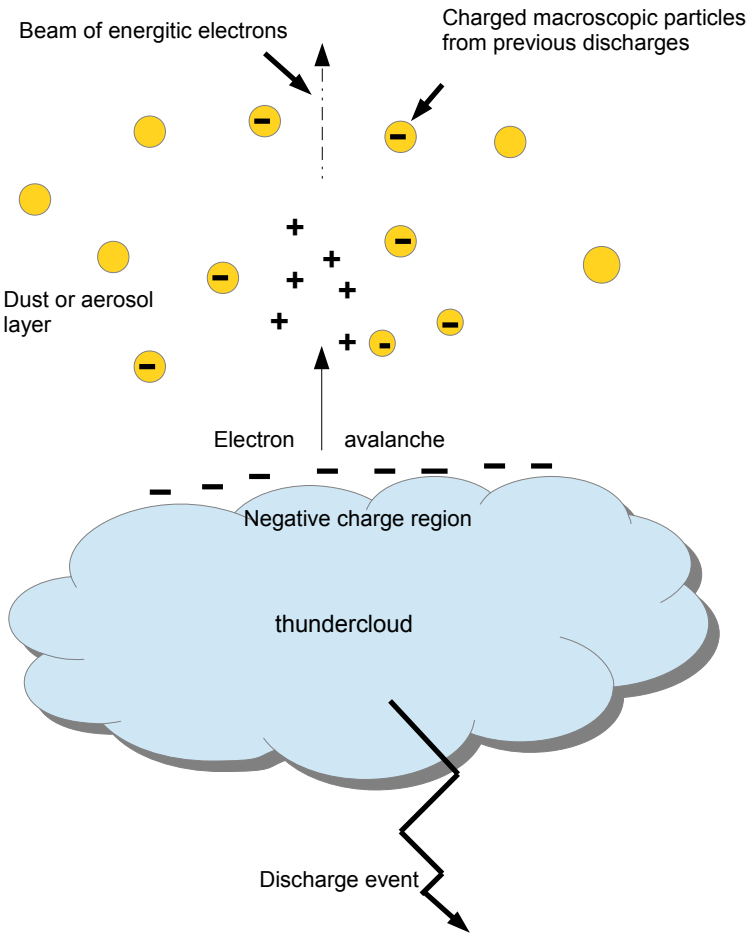

Figure 6.1: An electron beam form when electrons were ejected from a thundercloud top and moved in an electrical distribution of positive ions and negatively charged dust caused from a previous discharge [Füllekrug et al. (2013a)].

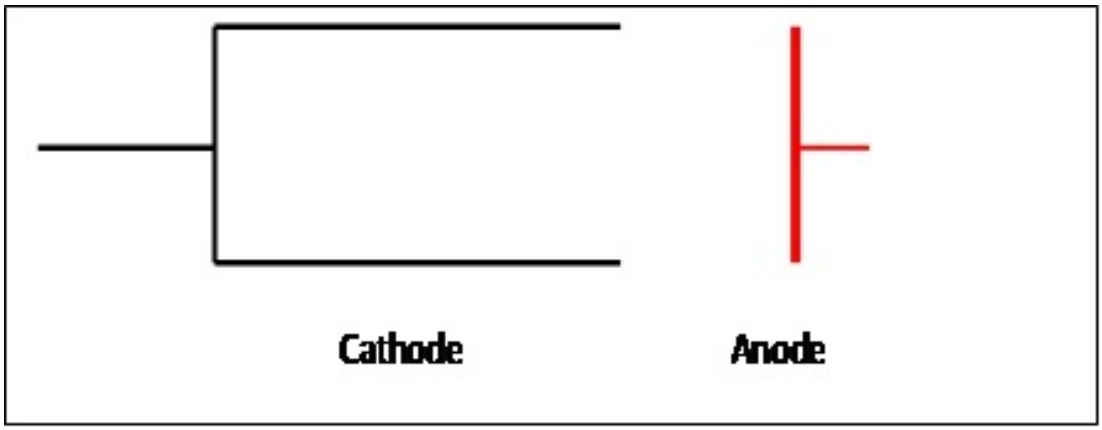

Figure 6.2: A diagram shows a hollow cathode with an outside anode.

These equations are the motion equation, a Poisson equation, and an electric field equation respectively. In order to make these equations dimensionless, the following parameters are used:

$$v \mapsto \hat{v} v_0 \tag{6.5}$$

$$t \mapsto \hat{t} t_0 \tag{6.6}$$

$$E \mapsto \hat{E} E_0 \tag{6.7}$$

$$\phi \mapsto \hat{\phi} \phi_0 \tag{6.8}$$

$$n_s \mapsto \hat{n}_s n_0 \tag{6.9}$$

$$\nabla \mapsto \hat{\nabla} s_0^{-1} \tag{6.10}$$

The denotation $\hat{}$ stands for the non-dimensional variables, whereas zero denotation represents scale variables. Hence, equations 6.1, 6.3, and 6.4 become:

$$\frac{d\hat{v}}{d\hat{t}} = P_a \hat{E} \tag{6.11}$$

$$\frac{d\hat{x}}{d\hat{t}} = P_b\hat{v}, \tag{6.12}$$

$$\hat{\nabla}^2\hat{\phi} = P_c(\hat{n_+} - \hat{n_e}), \tag{6.13}$$

$$\hat{E} = -P_d\hat{\nabla}\hat{\phi} \tag{6.14}$$

The equation for electrons kinetic energy in non-dimensional scales can be written as:

$$\hat{k} = P_e\hat{v}^2 \tag{6.15}$$

Where the non-dimensional parameters are defined as:

$$P_a = \frac{qt_0^2\phi_0}{ml_0^2} \tag{6.16}$$

$$P_b = \frac{t_0 v_0}{x_0} \tag{6.17}$$

$$P_c = \frac{q}{l_0\varepsilon_0\phi_0} \tag{6.18}$$

$$P_d = \frac{\phi_0}{E_0 l_0} \tag{6.19}$$

$$P_e = \frac{ml_0^2}{2qt_0^2} \tag{6.20}$$

The following substitutions are used to simplify the parameters:

$$n_0 = \frac{1}{l_0^3} \tag{6.21}$$

$$v_0 = \frac{l_0}{t_0} \tag{6.22}$$

$$E_0 = \frac{\phi_0}{l_0} \tag{6.23}$$

The non-dimensional parameters become:

$$P_a = \frac{q\phi_0 t_0^2}{ml_0^2} \tag{6.24}$$

$$P_b = 1 \tag{6.25}$$

$$P_c = \frac{q}{\varepsilon_0 l_0 \phi_0} \tag{6.26}$$

$$P_d = 1 \tag{6.27}$$

$$P_e = \frac{mev_0^2}{2e} \tag{6.28}$$

The non dimensional governing equations become:

$$\frac{d\hat{v}}{d\hat{t}} = P_a \hat{E} \tag{6.29}$$

$$\frac{d\hat{x}}{d\hat{t}} = \hat{v}, \tag{6.30}$$

$$\hat{\nabla}^2 \hat{\phi} = P_c(\hat{n_+} - \hat{n_e}), \tag{6.31}$$

$$\hat{E} = -\hat{\nabla}\hat{\phi} \tag{6.32}$$

$$\hat{k} = P_e \hat{v}^2 \tag{6.33}$$

6.5 Initial conditions for the simulation

A two dimensional computational domain with 15×60 grids is used to simulate the electron beam . The typical height of the environment where an electron beam above a thundercloud is produced is about $1km$ and its width is in the order of a few metres.

If a particle hits a boundary then calculations stop. The simulation is started by injecting electrons from an ellipse with size $a : b = 3 : 1$, where a and b are the major and minor axes of the ellipse, at the bottom of the simulation grids centred at position $[8, 4]$. The number of initial electrons is $\sim 10^3$. The electric potential of the suggested

hollow-cathode-like model simulation is about $-10\ eV$ at the lateral dust columns and for the top part of the thundercloud, a double positive potential for the ions column is created after the first electrons avalanche event. Table6.1 shows the initial conditions used in this simulation.

Table 6.1: Parameters used in numerical simulations.

Simulation property	Value
Domain dimensions	15×60
Domain boundaries	$\phi = -10$
Number of initial electrons	10^3
P_a	1

6.6 Results

The results for the electrons' evolution above the thundercloud with, and without the presence of the ions column are presented in Figs.6.8-6.10 and 6.5-6.7 respectively. Snapshots of the electrons' density, and their kinetic energy, are taken at four time intervals. Fig. 6.3 represents the electrostatic potential of the environment above the thundercloud without simulating an ions column. Fig. 6.4 represents the electrostatic potential of the environment above the thundercloud after producing positive ions by an electron avalanche.

6.6.1 Electron evolution without an ions column

Fig.6.5 shows the evaluated trajectory of one of the electrons which started from the initial ellipse of $\sim 10^3$ electrons at the bottom of the simulation domain. The electron trajectory evolved upwards on a wavy path with increased energy. Some electrons which started at the centre of the initial ellipse moved upwards in a straight line and gained the highest energy, as will be shown later. Decreased electron density results in

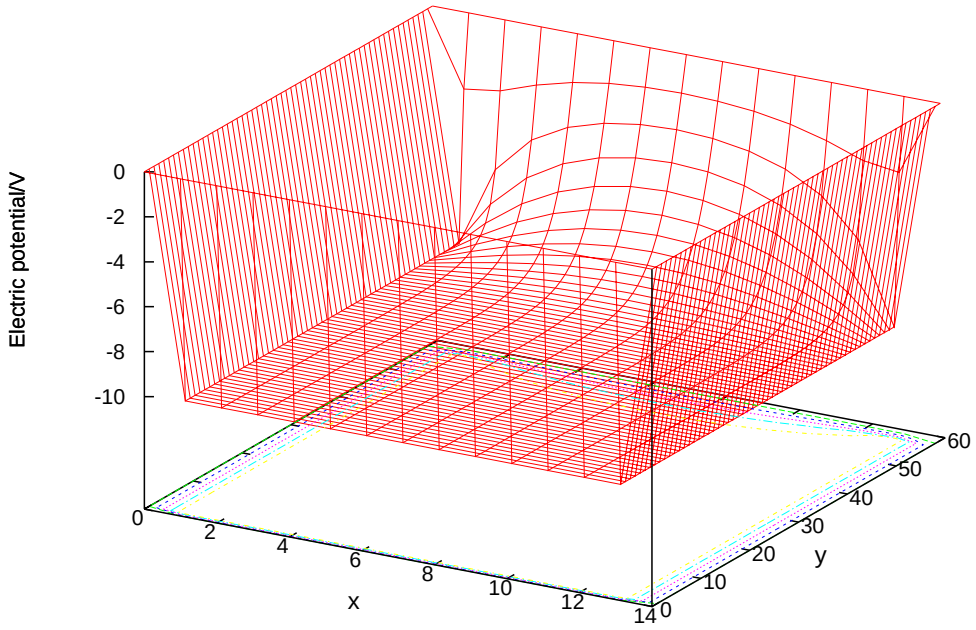

Figure 6.3: The simulated electrostatic environment after a sprite event without simulating an ions column. Dust grains have collected electrons from the sprite discharge represented by the negative region in the plot sides. The negative region at the bottom shows the top part of the cloud. This environment represent the one in Fig.6.1 but without simulating the ions column. The coloured and contour lines represent the electric potential.

reduced electric potential, as shown in Fig.6.6; however, electron density increased at some points (at the third time interval in the figure). The energy gained by the electrons in the first stage gain nearly equivalent energy, as shown in Fig.6.7 which represents the electrons final gained energy at each snapshot. Then, the energy increases slowly reaching the higher energy for the centered electrons and lower energy for the electrons which started at the ellipse edges.

If we assume that no self field is present in the calculations, the period of the oscillation of the electron can be found as follows: The equation of motion for the

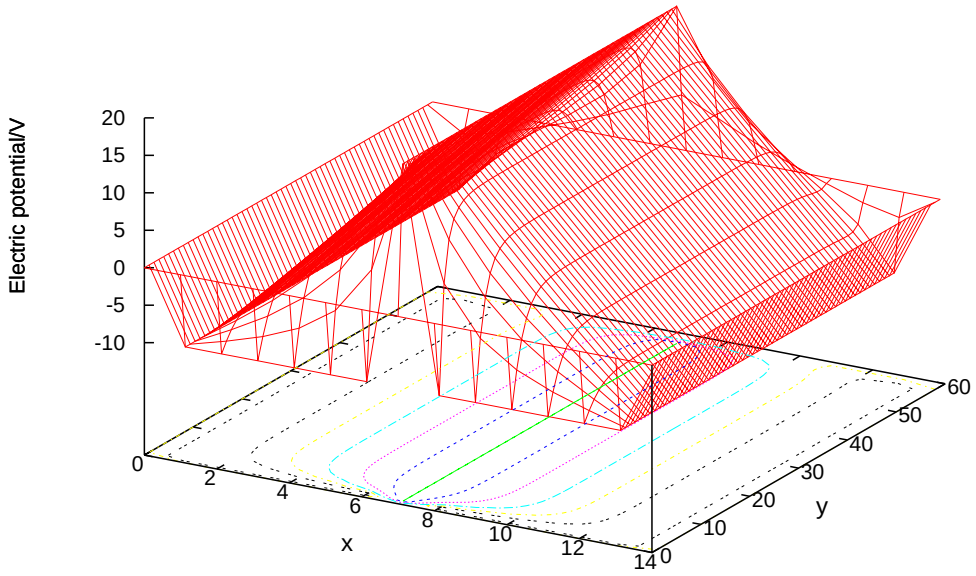

Figure 6.4: As Fig.6.3 but this time with a positive ions column created by the electrons avalanche during the sprite. This environment represent one similar to Fig.6.1.The coloured and contour lines represent the electric potential.

electron is:

$$m\dot{v} = -qE \tag{6.34}$$

$$\dot{v} = \frac{-q}{m}E \tag{6.35}$$

The electric field is the gradient of the electric potential:

$$E = -\nabla\phi \tag{6.36}$$

As the gradient of the electric potential between the central region and the sidewall is constant:

$$\nabla\phi = constant \tag{6.37}$$

therefore the electric field is constant except in the upper and lower regions of the model.

Integrating equation 6.34 gives:

$$v = \frac{-q}{m} Et \tag{6.38}$$

Integrating the equation again gives:

$$x = \frac{-q}{2m} Et^2 + x_0 \tag{6.39}$$

that gives:

$$t = (x - x_0)(\frac{-2m}{qE})^{1/2} \tag{6.40}$$

The previous equation gives the time the electron takes to reach the central axis from its original starting position. Because of the linearity of the electric field, the electron make a regular oscillator motion. Therefore, the electron's oscillation period is four times the time given in the equation. However, this is no longer applicable at the above region of the simulation domain, as the zero potential boundary at the open end will change it, increasing the time that the electron takes to make an oscillation and leading to a non regular oscillation.

6.6.2 Electron beam formation

Fig.6.8 shows the evolution of one electron which started from an ellipse presented at the bottom of the expected electrostatic environment in which a sprite event leaves a column of positive ions surrounded by electrons attached to dust grains.

The electrons transport upwards along the positive column in a wavy trajectory forming a thin path. The initial distribution of electrons spreads within the central region and does not spread sideways towards the vertical edges. That is as a result of the repulsion force from the side's negative potential and the attraction force of the central positive ions.

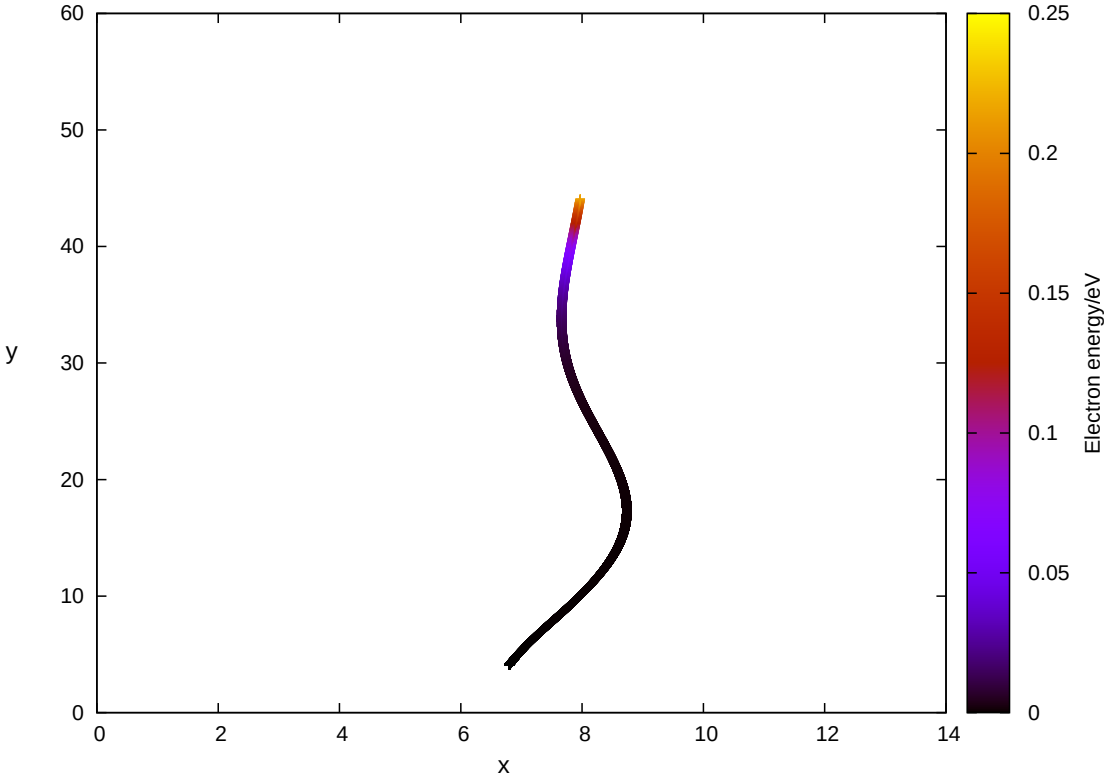

Figure 6.5: The evolution of one electron trajectory in an environment above a thundercloud where a sprite event was expected to initiate (see plot 6.3)

.

The electrons density as well as their electric potential are decreased during electrons evolution as shown in Fig.6.9. The electric ellipse evolves upwards vertically. Like the electrons' evolution without the positive ions, there is a distribution of the electrons' energy; however; they reach a higher maximum energy in a shorter time.

The distribution of the gained energy in Fig.6.10 shows that the central electrons gain higher energy than the sideways moving ones. That can be understood if the stronger electric field in the central region compared to the sides is noticed and these central electrons remain fixed in the central region. If the self field is involved in the calculations, these central electrons will gain even more energy as the self field from other electrons helps to repeal the central electrons, causing the formation of a beam. However, in this work, although the self field of electrons are included in the

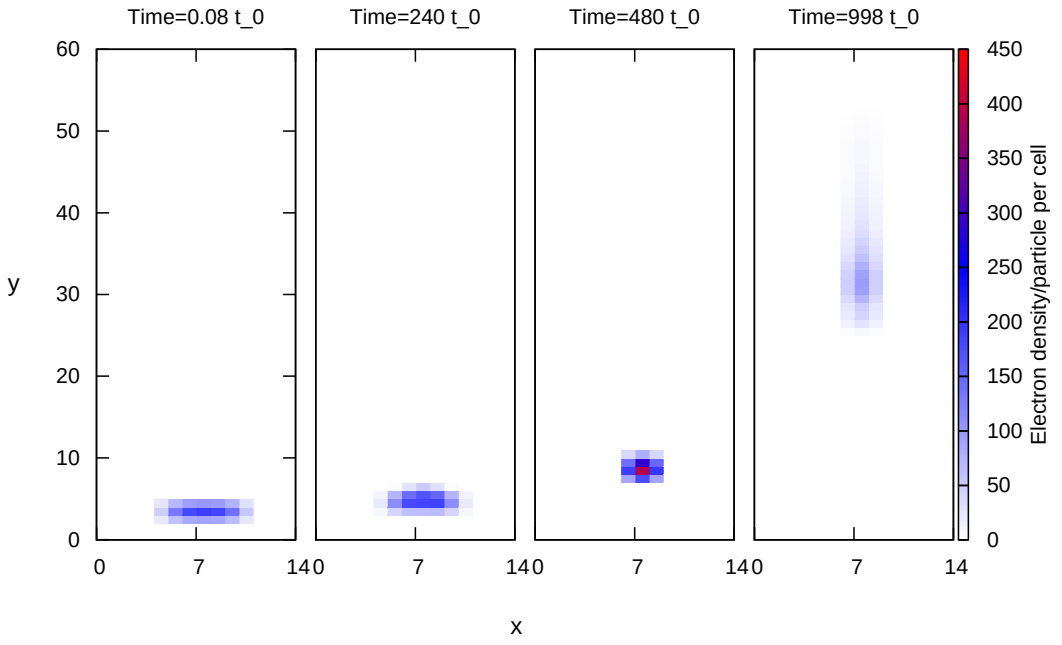

Figure 6.6: Snapshots of electron density evolution in an environment similar to Fig.6.3.

calculation, the self field's effect is nearly negligible as the number of initial electrons is not huge.

6.7 Conclusion

The electron beam can occur after sprites events. The presence of charged dust above thunderclouds is thought to have a basic role in electron beam formation in which the electrons avalanche in a sprite event leaving an environment of negatively charged dust and positive ions. This special electrostatic field configuration is similar to a hollow cathode pulsed discharges with a column of positive ions inside. The results for electrons' evolution in such an environment with and without the presence of positive ions have been presented. Electrons in an environment without positive ions evolve upwards, gaining lower final energy. In case when a positive column is presented,

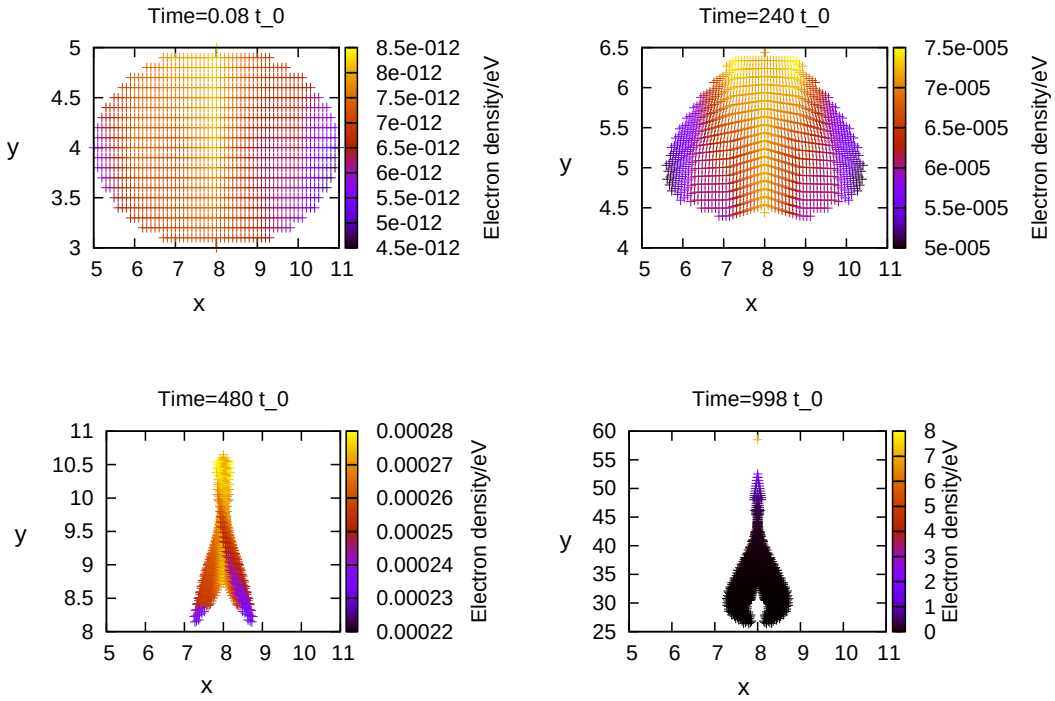

Figure 6.7: Snapshots of gained energy evolution in an environment similar to Fig.6.3.

electrons evolve upwards in a long path and do not bias to sidewalls. The trajectories of the electrons show an oscillator motion, the period of which depends on its original position. Electrons gain higher energy in a shorter time compared to the case in which the ions column is not simulated.

The distribution of the gained energy in presence of the column of positive ions shows that the central electrons gain higher energy than the sideways moving ones as a results of high electric field in the central region. Although the self field of electrons are included in the calculation, the self field's effect is nearly negligible as the number of initial electrons is not huge. Simulating a large number of electrons may cause the central electrons to gain even more energy as the self field from other electrons helps to repeal the central electrons, causing the formation of a beam.

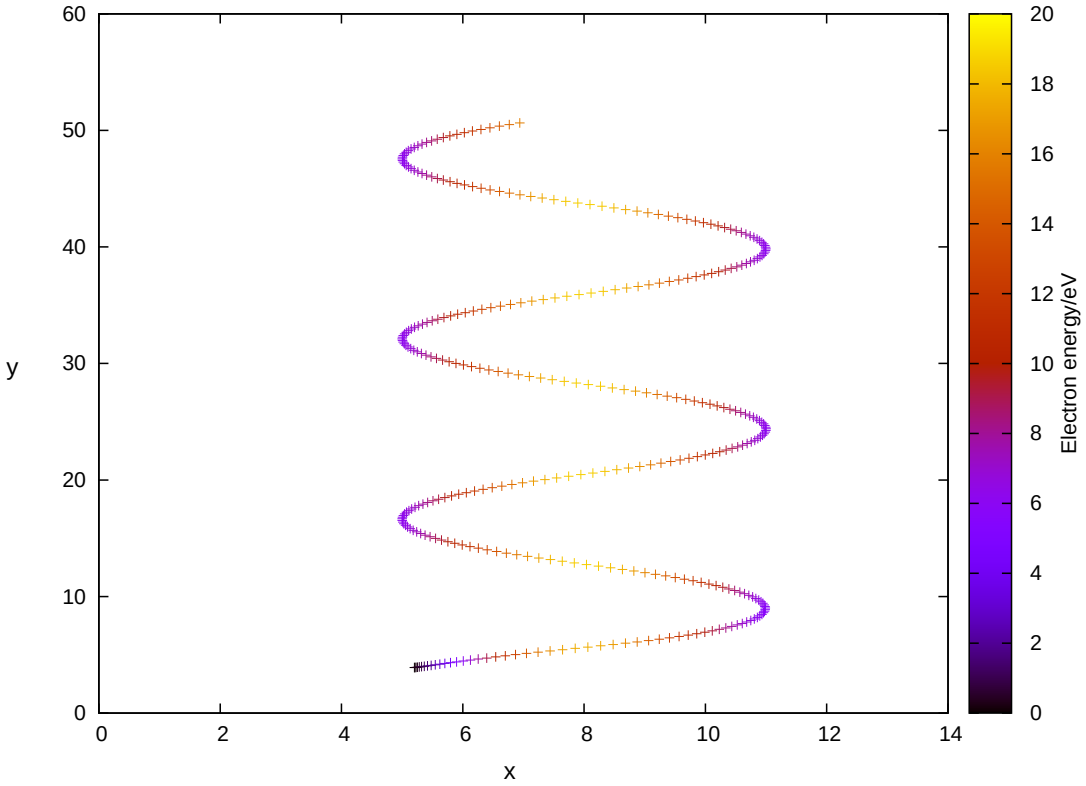

Figure 6.8: The evolution of one electron in an environment above a thundercloud and after a sprite creation where positive ions were left (see plot 6.3). The ellipse of electrons evolves in a long beam of electrons.

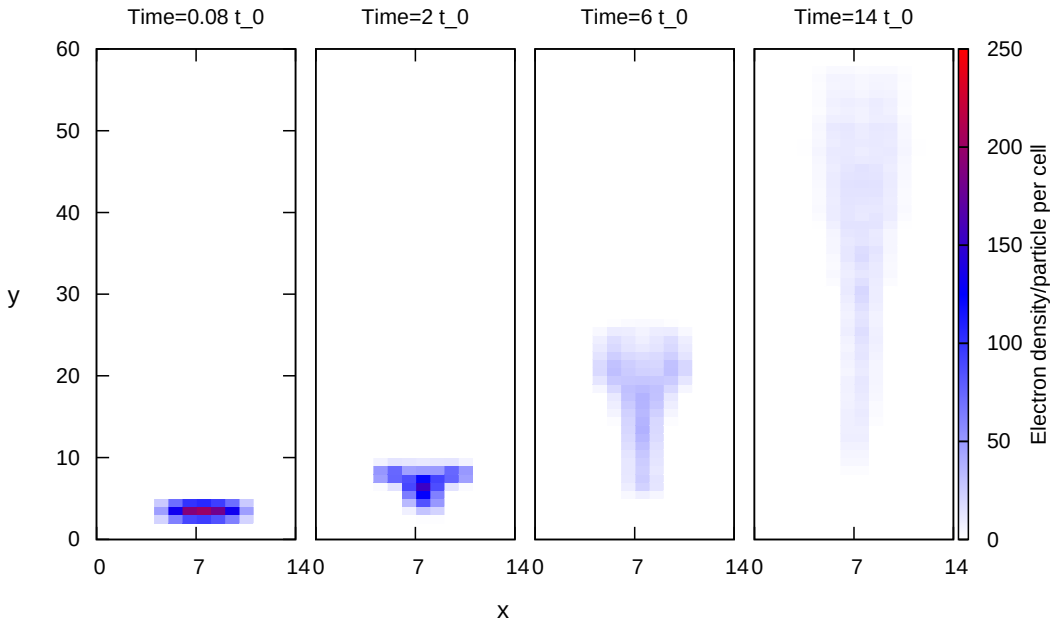

Figure 6.9: Snapshots of electron density evolution in an environment similar to Fig.6.4.

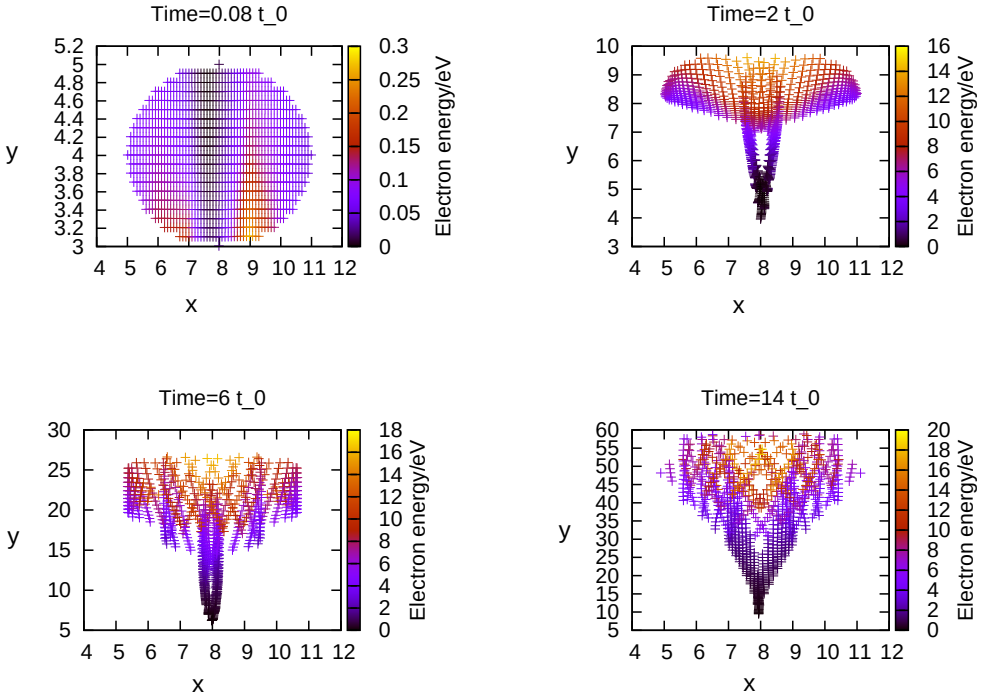

Figure 6.10: Snapshots of gained energy evolution in an environment similar to Fig.6.4.

7

Conclusion and Future work

The aim of this thesis was to investigate basic aspects of elliptical dust grains growth and interactions in plasma where electrostatic and magnetostatic background is present using various numerical techniques. Three main branches were explored: elliptical dust growth in magnetized sheath, was investigated in chapter 2 for 1-D and in chapter 4 for 3-D, dust interaction in submicron scales in chapter 5, and the collective dust grains interaction above thundercloud in chapter 6. Numerical methods were introduced and discussed to investigate these physical situations.

7.1 Elliptical dust growth

The Results from 1D simulations of dust growth presented in chapter 1 show the influence of the magnetic field on the ion loading on a charged grain surface. The electric field components acting on the ions motion were calculated analytically. Ions dynamics near the grain depend on the orientation of the magnetic field in respect to the long grain axis. For a perpendicular oriented magnetic field, ion deposition on grain surface was unbalanced, whereas at a parallel magnetic field, ions fluxes tend to increase at the grain's ends. In both cases, there was a population of trapped particles, orbiting close to the wire but not hitting it, that will effectively shield the electrostatic field from other charged particles. Chapter 4 presented a more reliable treatments of dust

growth, dealing the simulation in two and three dimensions using numerical techniques introduced in chapter 3 including finite difference method and Lagrange multiplier to solve the potential of an accurate ellipsoidal dust surface. The magnetic field was also directed perpendicularly and parallely to the major axis of the grain. The significance of the presence of magnetic field on growth of dust grains was investigated via varying the parameter p . In electrostatically dominated regime, ions distribution on dust surface was larger than magnetically dominated case. The direction of the magnetic field had also important role on ellipsoidal dust growth , encouraging grain's end growth when oriented parallel to the major axis of dust grain. Perpendicular magnetic field permits both surface and ends grain growth. Simulations showed a small significance of trapped ions on dust grains growth. While Stark (2008) research of elongated dust growth in astrophysical plasmas shows that the suggested growth process is an active tool providing the growth mechanism in the Supernova remnant, results in this chapter can assist to understand the the process of dust growth in magnetised plasma. In addition to be as an instrumental detection in the solar system to the presence of elliptical dust grains especially in magnetized regions, which can be tool in aligning the dust grains giving rising to the light polarization. Collisions between ions and neutrals, if involved in this simulation, could reduce the velocity of the ions and so making them subject to the field near the grain surface. Therefore, the ellipsoidal growth may increased. For a much reliable simulation of dust growth, the growth processes could be in presence of many charged dust grains. The combined electrostatic field arising from all dust can influence the dynamics of ions loading on grains surfaces. In addition, simulation the motion of charged dust while ions deposition can be interesting field of research. Since magnetic field has a role in elliptical dust grains alignment and therefore gives rise to starlight polarization [Diver and Clarke (1996)], it could be useful to include interstellar dust grain growth in model that account for their optical properties [Perets and Biham (2006)]. This model can give more accurate interstellar polarized light fitting.

7.2 Dust plasma interaction

Microdischarge plasmas is a special case of electrical discharges which occurs in geometries where one dimension at least is in range of sub-millimetre length scales. However a more extreme situation than microdischarge plasma where small size charged dust grains may cause discharge for the neutral gas when dust gaps reach to submicro scales was investigated. The interactions of charged dust grains in plasma where molecules of Oxygen gas are present and the effect on the discharge of the ambient gas were investigated in presence of magnetic field. The particle in cell model was used to simulate electrons motion in addition to using Monte Carlo method to simulate the electrons collisions with neutrals. The importance of the magnetic field was explored by varying the parameter p which gives the relative size of the electric field to the magnetic field. The distribution of electrons kinetic energies was investigated in two cases when ($p = 10^3$) and ($p = 10^2$). In the first case the gained energy increased dramatically, however, the gained energy did not exceed further than the metastables threshold as a result of consuming electrons energy in metastable collisions. When magnetic field is increased ($p = 10^2$), gained energy is fluctuated as a result of contribution in gyromotion orbits and electrons only involved in metastable collisions. However, a number of metastable in this case is lower than ($p = 10^3$) case. The presence of the magnetic field can help electrons to persist for longer and this gives electrons higher chance to involve in extra collisions.

The presence of he charged dust grains in plasma can activate the neutral gas in a non-thermal way. The metastable population is an important key in determining the required breakdown voltage as well as they can be a source of photons. The metastables have longer lifetime than the excited state. In addition, the metastables can be ionised by electrons with a lower energy than the ground state neutral. Therefore, the required electric field for breakdown becomes lower.

For further improvement of this work, one can simulate many number of charged dust grains in different orientation. Then electrons can transport in distances between

dust rising the electric potential in the simulating space leading to very active interactions of the ambient gas. This can cause to a faster breakdown of the gas.

7.3 Collective dust grains interaction above thunderclouds

The electron beam can occur just after sprites. The presence of charged dust above thundercloud are thought to have a basic role in the electron beam formation in which the electrons avalanche in sprite event leaving an environment of negative charged dust and positive ions column. This environment was simulated in a model like hollow cathode with a column of positive ions inside. The particle in cell was used to simulate particles motion.The results for electrons' evolution in such an environment with and without the presence of positive ions have been presented. Electrons in an environment without positive ions evolve upwards, gaining lower final energy. The trajectories of the electrons show an oscillator motion, the period of which depends on its original position. In case when a positive column is presented, electrons evolve upwards in a long path and do not bias to sidewalls. Electrons gain higher energy in a shorter time compared to the case in which the ions column is not simulated.

The distribution of the gained energy in presence of the column of positive ions shows that the central electrons gain higher energy than the sideways moving ones as a results of high electric field in the central region. Although the self field of electrons are included in the calculation, the self field's effect is nearly negligible as the number of initial electrons is not huge. Simulating a large number of electrons may cause the central electrons to gain even more energy as the self field from other electrons helps to repeal the central electrons, causing the formation of a beam.

Results from this work can clarify some aspects of the physics of energetic process in the earth's atmosphere and their impact on the technological systems and the earth's climate.

To modify this work, applying a strong electric potential on the environment above thundercloud model, causes electrons to move in relativistic speed. This requires the model equations that control particles motion to be in relativistic mode. Furthermore, simulating large number of electrons lead to self field of the simulated electrons to make effect in the particles motion and beam formation.

References

NL Aleksandrov and EM Bazelyan. Streamer breakdown of long gas gaps. *Plasma Physics Reports*, 27(12):1057–1078, 2001.

JE Allen. Probe theory-the orbital motion approach. *Physica Scripta*, 45(5):497, 1992.

JE Allen, BM Annaratone, and U De Angelis. On the orbital motion limited theory for a small body at floating potential in a maxwellian plasma. *Journal of plasma physics*, 63(04):299–309, 2000.

LP Babich, EN Donskoy, IM Kutsyk, and RA Roussel-Dupre. Characteristics of a relativistic electron avalanche in air. In *Doklady Physics*, volume 49, pages 35–38. Springer, 2004.

DN Baker, SG Kanekal, RB Horne, NP Meredith, and SA Glauert. Low-altitude measurements of 2–6 mev electron trapping lifetimes at 1.5 l 2.5. *Geophysical Research Letters*, 34(20), 2007.

Christopher P. Barrington-Leigh, Umran S. Inan, and Mark Stanley. Identification of sprites and elves with intensified video and broadband array photometry. *Journal of Geophysical Research: Space Physics*, 106(A2):1741–1750, 2001. ISSN 2156-2202. doi: 10.1029/2000JA000073. URL `http://dx.doi.org/10.1029/2000JA000073`.

Paul Murray Bellan. *Fundamentals of plasma physics*. Cambridge University Press, 2006.

Euan David Bennet. *Cosmic magnetism: The plasma physics of the recombining universe*. PhD thesis, University of Glasgow, 2012.

C. K. Birdsall. Particle-in-Cell Charged Particle Simulations, plus Monte Carlo Collisions with Neutral Atoms, PIC-MCC. In S. Kuhn, K. Schöpf, and R. Schrittwieser, editors, *Current Research on Fusion, Laboratory and Astrophysical Plasmas*, page 33, 1993.

W. S. Boyle and P. Kisliuk. Departure from paschen's law of breakdown in gases. *Phys. Rev.*, 97:255–259, Jan 1955. doi: 10.1103/PhysRev.97.255. URL http://link.aps.org/doi/10.1103/PhysRev.97.255.

N St J Braithwaite. Introduction to gas discharges. *Plasma Sources Science and Technology*, 9(4):517, 2000. URL http://stacks.iop.org/0963-0252/9/i=4/a=307.

O Chanrion and Torsten Neubert. Production of runaway electrons by negative streamer discharges. *Journal of Geophysical Research: Space Physics (1978–2012)*, 115(A6), 2010.

Ching-Heng Chen, J Andrew Yeh, and Pei-Jen Wang. Electrical breakdown phenomena for devices with micron separations. *Journal of Micromechanics and Microengineering*, 16(7):1366, 2006. URL http://stacks.iop.org/0960-1317/16/i=7/a=034.

Francis F Chen. Langmuir probes in rf plasma: surprising validity of oml theory. *Plasma Sources Science and Technology*, 18(3):035012, 2009.

Morris B Cohen, US Inan, RK Said, MS Briggs, GJ Fishman, V Connaughton, and SA Cummer. A lightning discharge producing a beam of relativistic electrons into space. *Geophysical Research Letters*, 37(18), 2010.

DA Diver and D Clarke. The evolution of cosmic and laboratory plasma dust. *Journal of Physics D: Applied Physics*, 29(3):687, 1996.

B. J. P. Dowds, R. K. Barrett, and D. A. Diver. Streamer initiation in atmospheric pressure gas discharges by direct particle simulation. *Phys. Rev. E*, 68:026412, Aug 2003a. doi: 10.1103/PhysRevE.68.026412. URL http://link.aps.org/doi/10.1103/PhysRevE.68.026412.

B. J. P. Dowds, R. K. Barrett, and D. A. Diver. Streamer initiation in atmospheric pressure gas discharges by direct particle simulation. *Phys. Rev. E*, 68:026412, Aug 2003b. doi: 10.1103/PhysRevE.68.026412. URL http://link.aps.org/doi/10.1103/PhysRevE.68.026412.

H Dreicer. Electron and ion runaway in a fully ionized gas. ii. *Physical review*, 117 (2):329, 1960.

Joseph R. Dwyer. Diffusion of relativistic runaway electrons and implications for lightning initiation. *Journal of Geophysical Research: Space Physics*, 115 (A3):n/a–n/a, 2010. ISSN 2156-2202. doi: 10.1029/2009JA014504. URL

http://dx.doi.org/10.1029/2009JA014504.

Joseph R Dwyer, Brian W Grefenstette, and David M Smith. High-energy electron beams launched into space by thunderstorms. *Geophysical Research Letters*, 35(2), 2008.

Ute Ebert, Sander Nijdam, Chao Li, Alejandro Luque, Tanja Briels, and Eddie van Veldhuizen. Review of recent results on streamer discharges and discussion of their relevance for sprites and lightning. *Journal of Geophysical Research: Space Physics (1978–2012)*, 115(A7), 2010.

O Eichwald, M Yousfi, O Ducasse, N Merbahi, JP Sarrette, M Meziane, and M Benhenni. Electro-hydrodynamics of micro-discharges in gases at atmospheric pressure, 2011.

Jan C. T. Eijkel, Herbert Stoeri, and Andreas Manz. A dc microplasma on a chip employed as an optical emission detector for gas chromatography. *Analytical Chemistry*, 72(11):2547–2552, 2000. doi: 10.1021/ac991380d. URL http://pubs.acs.org/doi/abs/10.1021/ac991380d.

Jeffrey P Freidberg. *Plasma physics and fusion energy*. Cambridge university press, 2007.

M Füllekrug, C Hanuise, and M Parrot. Experimental simulation of satellite observations of 100 khz radio waves from relativistic electron beams above thunderclouds. *Atmospheric Chemistry and Physics*, 11(2):667–673, 2011a.

Martin Füllekrug, Robert Roussel-Dupre, EMD Symbalisty, JJ Colman, O Chanrion, Serge Soula, O Velde, A Odzimek, AJ Bennett, VP Pasko, et al. Relativistic electron beams above thunderclouds. *Atmospheric Chemistry and Physics*, 11(15):7747–7754, 2011b.

Martin Füllekrug, Declan Diver, Jean-Louis Pinçon, Alan DR Phelps, Anne Bourdon, Christiane Helling, Elisabeth Blanc, Farideh Honary, R Giles Harrison, Jean-André Sauvaud, et al. Energetic charged particles above thunderclouds. *Surveys in Geophysics*, 34(1):1–41, 2013a.

Martin Füllekrug, Ivana Kolmasova, Ondrej Santolik, Thomas Farges, József Bór, Alec Bennett, Michel Parrot, William Rison, Ferruccio Zanotti, Enrico Arnone, et al. Electron acceleration above thunderclouds. *Environmental Research Letters*, 8(3): 035027, 2013b.

Samiran Ghosh, R. Bharuthram, Manoranjan Khan, and M. R. Gupta. Instability of

dust acoustic wave due to nonthermal ions in a charge varying dusty plasma. *Physics of Plasmas (1994-present)*, 11(7), 2004.

David B Go and Daniel A Pohlman. A mathematical model of the modified paschens curve for breakdown in microscale gaps. *Journal of Applied Physics*, 107(10): 103303, 2010.

CK Goertz. Dusty plasmas in the solar system. *Reviews of Geophysics*, 27(2):271–292, 1989.

Robert J Goldston and Paul Harding Rutherford. *Introduction to plasma physics*, volume 1. CRC Press, 1995.

Jón Tómas Gudmundsson. A critical review of the reaction set for a low pressure oxygen processing discharge. Technical report, Technical Report RH-17-2004, Science Institute, University of Iceland, 2004.

Alexander V Gurevich and Kirill P Zybin. Runaway breakdown and the mysteries of lightning. *Phys. Today*, 58(5):37–43, 2005.

Christiane Helling, Moira Jardine, Declan Diver, and Sören Witte. Dust cloud lightning in extraterrestrial atmospheres. *Planetary and Space Science*, 77:152–157, 2013.

Noah Hershkowitz. Sheaths: More complicated than you thinka). *Physics of Plasmas (1994-present)*, 12(5):055502, 2005.

Yasutaka Hiraki and Hiroshi Fukunishi. Theoretical criterion of charge moment change by lightning for initiation of sprites. *Journal of Geophysical Research: Space Physics (1978–2012)*, 111(A11), 2006.

Felipe Iza, Gon Jun Kim, Seung Min Lee, Jae Koo Lee, James L Walsh, Yuantao T Zhang, and Michael G Kong. Microplasmas: Sources, particle kinetics, and biomedical applications. *Plasma Processes and Polymers*, 5(4):322–344, 2008.

Jin Jeon, Tanja M Rosentreter, Yangfang Li, Georg Isbary, Hubertus M Thomas, Julia L Zimmermann, Gregor E Morfill, and Tetsuji Shimizu. Bactericidal agents produced by surface micro-discharge (smd) plasma by controlling gas compositions. *Plasma Processes and Polymers*, 2014.

M Klas, Š Matejčik, B Radjenović, and M Radmilović-Radjenović. Experimental and theoretical studies of the direct-current breakdown voltage in argon at micrometer separations. *Physica Scripta*, 83(4):045503, 2011.

James G Laframboise. Theory of spherical and cylindrical langmuir probes in a collisionless, maxwellian plasma at rest. Technical report, DTIC Document, 1966.

Martin Lampe. Limits of validity for orbital-motion-limited theory for a small floating collector. *Journal of plasma physics*, 65(03):171–180, 2001a.

Martin Lampe. Limits of validity for orbital-motion-limited theory for a small floating collector. *Journal of plasma physics*, 65(03):171–180, 2001b.

Leon Lapidus and George F Pinder. *Numerical solution of partial differential equations in science and engineering*. John Wiley & Sons, 2011.

SA Lawton and AV Phelps. Excitation of the b $1\sigma+$ g state of o2 by low energy electrons. *The Journal of Chemical Physics*, 69(3):1055–1068, 2008.

LM Lidsky, SD Rothleder, DJ Rose, S Yoshikawa, C Michelson, and RJ Mackin Jr. Highly ionized hollow cathode discharge. *Journal of Applied Physics*, 33(8):2490–2497, 2004.

Michael A Lieberman and Alan J Lichtenberg. *Principles of plasma discharges and materials processing*. John Wiley & Sons, 2005.

Michael A Lieberman and Allan J Lichtenberg. Principles of plasma discharges and materials processing. *MRS Bulletin*, 30:899–901, 1994.

Leonard B Loeb. Streamer breakdown and sparking thresholds. *Physical Review*, 81: 287–287, 1951.

Craig S MacLachlan. *Numerical modelling of low temperature plasma*. PhD thesis, University of Glasgow, 2009.

Davide Mariotti and R Mohan Sankaran. Microplasmas for nanomaterials synthesis. *Journal of Physics D: Applied Physics*, 43(32):323001, 2010a.

Davide Mariotti and R Mohan Sankaran. Microplasmas for nanomaterials synthesis. *Journal of Physics D: Applied Physics*, 43(32):323001, 2010b. URL `http://stacks.iop.org/0022-3727/43/i=32/a=323001`.

Radu Mavrodineanu. Hollow cathode discharges. *J. Res. Nat. Bureau Standards*, 89 (2):143, 1984.

JM Meek. A theory of spark discharge. *Physical Review*, 57(8):722, 1940.

DA Mendis. Progress in the study of dusty plasmas. *Plasma Sources Science and Technology*, 11(3A):A219, 2002.

S Meshkani, M Lafouti, M Ghoranneviss, and A Salar Elahi. Stft analysis of the particle transport on the ir-t1 tokamak plasma sheath. *Journal of Fusion Energy*, 33 (2):108–118, 2014.

Maxime Mikikian, Marjorie Cavarroc, Lénaïc Couëdel, Yves Tessier, and Laïfa Boufendi. Dust particles in low-pressure plasmas: Formation and induced phenomena. *Pure & Applied Chemistry*, 82(6), 2010.

Harold M Mott-Smith and Irving Langmuir. The theory of collectors in gaseous discharges. *Physical review*, 28(4):727, 1926.

J. A. Nuth, III, F. J. M. Rietmeijer, and H. G. M. Hill. Condensation processes in astrophysical environments: The composition and structure of cometary grains. *Meteoritics and Planetary Science*, 37:1579–1590, November 2002. doi: 10.1111/j.1945-5100.2002.tb00812.x.

A. B. C. Patzer, T. M. Köhler, and E. Sedlmayr. Primary astrophysical dust formation: laboratory desiderata. *Planet. Space Sci.*, 43:1233–1239, February 1995. doi: 10.1016/0032-0633(95)00050-F.

Hagai B Perets and Ofer Biham. Molecular hydrogen formation on porous dust grains. *Monthly Notices of the Royal Astronomical Society*, 365(3):801–806, 2006.

K. Petcharaks. A contribution to the streamer breakdown criterion. In *High Voltage Engineering, 1999. Eleventh International Symposium on (Conf. Publ. No. 467)*, volume 3, pages 19–22 vol.3, 1999. doi: 10.1049/cp:19990689.

Z Lj Petrovi, N Åkoro, D Mari, C M O Mahony, P D Maguire, M Radmilovi-Raenovi, and G Malovi. A particle-in-cell simulation of the breakdown mechanism in microdischarges with an improved secondary emission model. *Contributions to Plasma Physics*, 47(3):165, 2007. URL `http://dx.doi.org/10.1002/ctpp.200710023`.

William H Press. *Numerical recipes in Fortran 77: the art of scientific computing*, volume 1. Cambridge university press, 1992.

M. Radmilovi-Radjenovi and B. Radjenovi. An analytical relation describing the dramatic reduction of the breakdown voltage for the microgap devices. *EPL (Europhysics Letters)*, 83(2):25001, 2008. URL `http://stacks.iop.org/0295-5075/83/i=2/a=25001`.

M Radmilović-Radjenović and B Radjenović. A particle-in-cell simulation of the breakdown mechanism in microdischarges with an improved secondary emission model. *Contributions to Plasma Physics*, 47(3):165–172, 2007.

M Radmilović-Radjenović, Jae Koo Lee, Felipe Iza, and GY Park. Particle-in-cell simulation of gas breakdown in microgaps. *Journal of physics D: applied physics*,

38(6):950, 2005.

Marija Radmilovic-Radjenovic and Branislav Radjenovic. A particle-in-cell simulation of the high-field effect in devices with micrometer gaps. *Plasma Science, IEEE Transactions on*, 35(5):1223–1228, 2007.

P Raizer Yu. Gas discharge physics, 1991.

Jean-Baptiste Renard, Gwenaël Berthet, Verónica Salazar, Valery Catoire, Michel Tagger, Bertrand Gaubicher, and Claude Robert. In situ detection of aerosol layers in the middle stratosphere. *Geophysical Research Letters*, 37(20), 2010.

C.P.R Saunders and J.S Rimmer. The electric field alignment of ice crystals in thunderstorms. *Atmospheric Research*, 51(34):337 – 343, 1999. ISSN 0169-8095. doi: http://dx.doi.org/10.1016/S0169-8095(99)00018-6. URL http://www.sciencedirect.com/science/article/pii/S0169809599000186.

Padma K Shukla and AA Mamun. *Introduction to dusty plasma physics*. CRC Press, 2010.

C. R. Stark, H. E. Potts, and D. A. Diver. Elliptical dust growth in astrophysical plasmas. *A&A*, 457:365–370, October 2006. doi: 10.1051/0004-6361:20064922.

Craig R Stark. *Plasma processes in pulsar environments*. PhD thesis, University of Glasgow, 2008.

Z. Sternovsky, Martin Lampe, and S. Robertson. Orbiting ions in the debye shielding cloud around dust particles in weakly collisional plasmas. *Plasma Science, IEEE Transactions on*, 32(2):632–636, April 2004. ISSN 0093-3813. doi: 10.1109/TPS.2004.826081.

Cyril Szopa, Guy Cernogora, Laifa Boufendi, Jean J Correia, and Patrice Coll. Pampre: A dusty plasma experiment for titan's tholins production and study. *Planetary and space Science*, 54(4):394–404, 2006.

P. A. Tchertchian, C. J. Wagner, T. J. Houlahan, B. Li, D. J. Sievers, and J. G. Eden. Control of the interface between electron-hole and electron-ion plasmas: Hybrid semiconductor-gas phase devices as a gateway for plasma science. *Contributions to Plasma Physics*, 51(10):889–905, 2011. ISSN 1521-3986. doi: 10.1002/ctpp.201100037. URL http://dx.doi.org/10.1002/ctpp.201100037.

Paul A Tipler and Gene Mosca. *Physics for scientists and engineers*. Macmillan, 2007.

Lewi Tonks and Irving Langmuir. Oscillations in ionized gases. *Physical Review*, 33

(2):195, 1929.

J-M Torres and R S Dhariwal. Electric field breakdown at microtre separations. *Nanotechnology*, 10(1):102, 1999. URL http://stacks.iop.org/0957-4484/10/i=1/a=020.

Z. Ulanowski, J. Bailey, P. W. Lucas, J. H. Hough, and E. Hirst. Alignment of atmospheric mineral dust due to electric field. *Atmospheric Chemistry and Physics*, 7(24):6161–6173, 2007. doi: 10.5194/acp-7-6161-2007. URL http://www.atmos-chem-phys.net/7/6161/2007/.

Oscar A. van der Velde, Joan Montany, Serge Soula, Nicolau Pineda, and Joan Bech. Spatial and temporal evolution of horizontally extensive lightning discharges associated with sprite-producing positive cloud-to-ground flashes in northeastern spain. *Journal of Geophysical Research: Space Physics*, 115(A9): n/a–n/a, 2010. ISSN 2156-2202. doi: 10.1029/2009JA014773. URL http://dx.doi.org/10.1029/2009JA014773.

C.G. Wilson and Y.B. Gianchandani. Silicon micromachining using in situ dc microplasmas. *Microelectromechanical Systems, Journal of*, 10(1):50–54, 2001. ISSN 1057-7157. doi: 10.1109/84.911091.

J Winter. Dust in fusion devicesa multi-faceted problem connecting high-and low-temperature plasma physics. *Plasma physics and controlled fusion*, 46(12B):B583, 2004.